Double spin resonance of electrons in snake states

Saraiva, Pedro

Award date:
2010

Awarding institution:
University of Bath

Double spin resonance of electrons in snake states

submitted by

Pedro Varela Saraiva

for the degree of Doctor of Philosophy

of the

University of Bath

Department of Physics

December 2010

Signature of Author .....

Pedro Varela Saraiva

Abstract

Two-dimensional electron gases (2DEG) located at GaAs/$Al_{0.33}Ga_{0.67}As$ heterojunctions are modulated by a periodic magnetic field generated by a magnetic grating fabricated at the surface of the heterostructure and are irradiated by microwaves. The devices were investigated for the detection of excitations of both paramagnetic and ferromagnetic spins in the magnetoresistance. Electron spin antiresonance was electrically detected, where spin flips are propelled by two transitions: one activated by snake orbit oscillations in the slanted magnetic field, the other by the microwaves. The double resonance forms a dark state which blocks spin flips, decreases Overhauser shift and freezes snake orbit drift, therefore changing the conduction in the 2DEG. The antiresonance is quantitatively described in the coherent population trapping framework. Collective and localised spin wave modes in dysprosium and cobalt gratings were detected as well in the 2DEG. Such effects were investigated as a function of microwave power, temperature, tilt angle of the applied magnetic field, and by varying the structural and material parameters to change the strength of dipolar interactions. The data reveal two types of spin waves. Dipolar magnetisation waves propagate across the grating through the magnetostatic interaction between stripes. An analytical expression of their dispersion curve was derived and a good fit of the ferromagnetic resonance broadening was obtained. The second type are dipolar edge spin waves which manifest through a series of sharp resonances at lower magnetic field. These waves are confined near the pole surfaces in spin wave "wells". The eigenfrequencies of the quantised modes were calculated and a qualitative explanation of the low field resonances was obtained. The experiments show that photovoltage measurements in hybrid semiconductor-ferromagnetic structures provide a sensitive and non-invasive tool for probing the spin waves of small magnets.

Acknowledgements

I would like to thank:

Dr Alain Nogaret, my supervisor, for giving me the opportunity to do research at this level, for letting me use the facilities of his group, for providing me with samples from where the results reported in this Thesis were obtained and for the skills I have learned by working with him and his collaborators;

Dr Bo Dai and Dr Vyascheslav Kachkanov for the skillful nanofabrication of the devices;

Prof. Jean-Claude Portal and Steffen Wiedmann at the LNCMI-CNRS in Grenoble, France for kindly integrating me in their group during my three visits to their laboratory, for the opportunity to use their world-class facilities and all the technical assistance;

Prof. Simon Bending for letting me use his "dirty" thermal evaporator for depositing dysprosium;

Bob Draper, Wendy Lambson and Dr Spartaco Landi for the technical assistance;

My parents for being my biggest supporters all this time, for being at my side in all the decisions I have made;

Andrea Gonçalves, my partner in life, for speaking "the same language" as me, for supporting me unconditionally, for being an inspiration as a person and a scientist;

Finally, my labmates Stephen Taylor, Dr Farzad Nasirpouri, Ashok Chauhan, André Müller, Miles Engbarth, Dr Sara Dale and Peter Lewis for their friend-

ship, moral support and for contributing for the fundamental balance between professional and social/personal life.

Contents

List of Figures

Chapter 1

Introduction

The aim of the work reported on this Thesis is about developing a sub-micron scale device which detects microwaves by outputting an electric signal dependent on its frequency by exploiting a novel class of physical effects that use two-dimensional electron systems under the influence of a perpendicular, space varying magnetic field. This capability refers to one half of the functionality of a transceiver device.

Broadband microwave nanotransceivers would replace metal interconnects which, with the constant demand for more speed and miniaturisation in the microelectronics industry, are reaching fundamental material limits. Wireless interconnects would operate at very high frequencies (1 GHz - 1 THz) with virtually no loss. Active components of an electronic device would be connected in a wireless local area network and would not need to be assembled in a planar circuit board due to the absence of physical interconnects, thus the integration density would be increased and the packaging would be easier.

The microwave frequency is detected in the device by inducing magnetic resonance of electrons located at the active region of the device and make the effect observable when measuring the resistance. The electrons are located at the interface of two layers of two semiconducting materials: GaAs and AlGaAs. When both materials are brought into contact, the electrons become confined in a plane, a medium usually called a two-dimensional electron gas (2DEG). Much like a thin-

film transistor, a rectangular region of the structure is etched, where the electron current drifts from source to drain. Instead of an electrostatic gate, the device is equipped with a magnetic gate in form of a stripe, deposited along the length of the 2DEG, whose utility will be explained later.

In order to become resonant, in an effect that will be called from now on as electron spin resonance (ESR), the electron must be subjected to a static magnetic field and a time-dependent magnetic field. The magnetic moment of the electron precesses at a frequency proportional to the magnitude of the static magnetic field, called Larmor frequency. Magnetic resonance is induced when the frequency of precession matches the frequency of the time-dependent magnetic field. Conventionally, the magnetic component of an electromagnetic wave is used as the time-dependent magnetic field. Electrical detection of microwave induced electron spin resonance in 2DEGs was demonstrated more than twenty years ago by Dobers *et al* [5, 6] in very specific conditions. In the case presented in this Thesis, a more reliable and versatile mechanism is described.

When a static magnetic field is applied in-plane with the 2DEG but across the magnetic stripe, the stripe becomes magnetised in a way so that it subjects the 2DEG to an almost linear gradient of perpendicular magnetic field. The 2DEG has therefore two regions subjected to magnetic fields of opposite sign, separated by a line where the magnetic field vanishes, called magnetic edge. According to its position, the electron is bent by the Lorentz force towards the magnetic edge. When the magnetic edge is crossed, the magnetic field changes sign and so does the direction of the Lorentz force, forcing it to a lateral spatial oscillation about the magnetic edge as it drifts from the source towards the drain. Such trajectories will be referred in the text as snake orbits. There is a continuous spectrum of snake orbit frequencies, within a finite range. Electrons doing such periodical trajectories inside the linear gradient of magnetic field will be effectively subjected to a time-dependent magnetic field [7, 8].

Like with the time-dependent magnetic field component of the microwaves, magnetic resonance can be excited in these electrons through this time-dependent magnetic field felt by electrons in snake orbits. ESR through this field is always occuring in the range of magnetic fields applied in the performed experiments.

By themselves, neither the magnetic resonance induced by the microwaves or the snake orbits changes the conductivity of the 2DEG, therefore no change in the magnetoresistance is observed.

Inducing ESR boosts the polarisation of the GaAs nuclei which can generate magnetic fields up to 5.7 T, when the nuclear polarisation is saturated [9]. Nuclear fields add to the static magnetic field and therefore shift the resonance position to lower field in magnetoresistance spectra. Nuclear fields with magnitudes similar to the predicted maximum value were observed, suggesting that the nuclear polarisation is saturated, which can be explained by the always occuring magnetic resonance.

When the microwave induced ESR condition is met, magnetic resonance is being driven by two different time-dependent magnetic fields with two different magnitudes, and therefore two different Rabi frequencies at the same time, since snake-induced ESR is always occuring. The situation can be illustrated by a three-level quantum system where electrons in two states at the ground level can be excited to a top level state when the respective transition is resonant. It is suggested that both transitions can interfere destructively. It is demonstrated mathematically that the three level quantum system evolves with time to a state where spin flips are blocked, the dark state [10].

It is suggested that if spin flips are blocked the electron is scattered off the snake orbit. If the electron is scattered off the orbit, source-drain conduction is affected. It is also suggested that the longitudinal conductivity is proportional to the probability of evolving to the dark state, which is equivalent to the fraction of electrons which get scattered of the orbit. The probability of formation of the dark state is derived and the change in resistivity is estimated, which agrees quantitatively with the experiment.

To complement the study of the physics involved in the operation of the device, other features in the magnetoresistance spectra were investigated. It is known that by applying the perpendicular magnetic field gradient to the 2DEG using the magnetic gate, thus inducing the formation of snake orbits, the magnetoresistance changes considerably [3]. Spins in the magnetic stripe can enter magnetic resonance also, an effect called ferromagnetic resonance (FMR). When FMR is

induced, the magnetisation vector oscillates at high frequency and the magnetic potential felt at the 2DEG vanishes momentarily. Therefore, it is suggested the 2DEG can be employed as a sensor to detect perturbations to the spin ensemble of very small magnetic samples.

Measuring the magnetoresistance of a sample with a single magnetic stripe on top corroborates the above, showing a change in the magnetoresistance spectra located at the value of magnetic field predicted by shape anisotropy [11]. While the line shape of FMR of a single stripe is sharp, magnetoresistance spectra of a one-dimensional array of stripes reveals a broad structure, spanning up to more than 1 T.

It is suggested that this broad resonance signal arises from the formation of magnetisation waves in the one-dimensional array of magnetic stripes. These waves propagate the dephasing of the magnetisation vector from one stripe to another through dipolar interaction, hence the designation dipolar magnetisation waves (DMW). The derived energy dispersion relation of the dipolar magnetisation waves generalises the resonance frequency condition given by the shape anisotropy, taking the dipolar interaction of neighbouring stripes into account. The frequency bandwidth of the dispersion relation corresponding to the whole range of modes limited by the in-phase and out-of-phase oscillation modes agrees quantitatively with the width of the broad resonant structure found in the magnetoresistance spectra.

In addition, a series of small resonant dips were observed at lower field. The internal magnetic field inside the magnetic stripe is inhomogenenous in the plane of the stripe, being stronger in the middle of the stripe and decreasing considerably as it approaches the lateral edges. When microwaves are applied to the sample, the phase of spins inside the magnetic magnetic material start to oscillate, giving rise to spin waves. The spin wave modes that propagate transversely inside the stripe become confined within the region of lower internal field [1].

That region acts as a quantum well, discretising the spin wave modes that can propagate in the region. This class of spin waves are called dipolar edge spin waves (DESW). It is suggested the observed small dips at low field correspond to the frequency of the allowed spin wave modes oscillating in the well. Experimental

results agree with the theory up to a certain point but not completely. Limitations to the theory are discussed.

The results of this Thesis are therefore separated in two parts. Evidence of electron spins scattered off snake orbits when in microwave induced magnetic resonance is described in Chapter 5, whereas results related to the observation of two types of dipolar spin waves in magnetic superlattices are in Chapter 4. In order to contextualise the results, some theoretical fundamentals are mentioned in the following Chapter 2. Preceding the results in their own chapter, more specific theory is reviewed, such as spin wave wells in transversely magnetised magnetic stripes in Chapter 4, ballistic electrons in a spatially periodic magnetic field and the formation of the dark state under CPT in Chapter 5. Finally, samples and experimental methods used in the production of the results are described in Chapter 3.

Chapter 2

Theoretical fundamentals

The present chapter is composed by a selection of subjects which aims to contextualise the results and interpretations found in the later chapters of the Thesis.

2.1 GaAs/AlGaAs-based 2DEGs in a perpendicular magnetic field

When two semiconductors with different bandgaps and Fermi energies come into contact, the chemical potential propagates throughout the heterostructure, bending the valence and conduction bands and setting the Fermi level for the whole structure. The electrons become confined at the interface due to a parabolic potential well created by the offset between the conduction bands of both semiconductors and the positively ionised donors, as it can be seen in Figure 2-1. Due to the confinement in the plane of the interface, two-dimensional subbands are created corresponding to the discrete states in the potential well, creating the two-dimensional electron gas (2DEG).

The electron transport in 2DEGs is usually characterised by three ideal modes of operation [12]. The first two, the diffusive and ballistic regimes, can be attained without an applied magnetic field, unlike the third type which will be introduced later. The property that distinguishes between the first two regimes is the relation

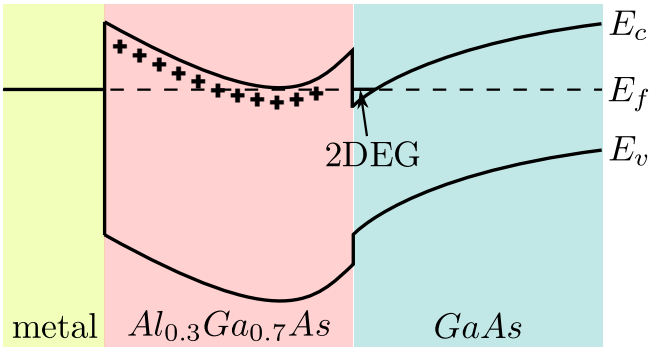

Figure 2-1: *Band diagram of an GaAs/AlGaAs heterostructure.*

between the sample dimensions and the mean free path λ. If the sample width is much greater than λ, there is a higher probability that the electron will be scattered by an impurity than by the boundary of the sample and it can be said that the electron transport is diffusive. In the ballistic regime, the sample length is smaller than λ. Therefore, scattering by the edge of the sample predominates. An intermediate regime of electron transport is often considered, designated quasi-ballistic. It occurs when λ is comparable to the sample's dimensions and there is approximately the same probability of electron scattering either by impurities or sample boundaries.

When an electric field E is applied in the plane of the 2DEG, an electron moves with drift velocity $\vec{v}$, given by the expression

$$\vec{v} = \frac{-e\vec{E}\Delta t}{m^*} \tag{2.1}$$

where Δt is the time elapsed since the last impurity collision and m^* is the effective electron mass, equal to $0.067m_e$ in GaAs. The average of Δt is the scattering time τ and the average drift velocity is given by the expression

$$\vec{v}_d = -\mu_e\vec{E} \tag{2.2}$$

where μ_e is the electron mobility, given by $\mu_e = e\tau/m$. The drift velocity and electrical field vector point to opposite directions, hence the minus sign. The drift current is defined as

$$\vec{J}_d = -en_s\vec{v}_d \tag{2.3}$$

where n_s is the electron density. According to the Ohm's law,

$$\vec{J}_d = \sigma\vec{E} \tag{2.4}$$

where one can derive the conductivity as $\sigma = n_s e\mu_e$.

The energy $E(k)$ of an electron in a subband of a 2DEG is given by

$$E(k) = \frac{\hbar^2 k^2}{2m^*} \tag{2.5}$$

The density of states $\rho(E)$ is the derivative of the number of electronic states n(E) with energy below E,

$$\rho(E) = \frac{dn(E)}{dE} \tag{2.6}$$

The number of states is given by

$$n(E) = \frac{g_s g_v A}{(2\pi)^2} \tag{2.7}$$

where g_s and g_v are the spin degeneracy and the valley degeneracy, respectively, and A is the area of the Fermi surface, which is a circle in k-space with radius equal to the Fermi wavevector k_F, where the states are contained, given by

$$A = \pi k_F^2 \tag{2.8}$$

Therefore, the density of states of a subband in a 2DEG is

$$\rho(E) = \frac{g_s g_v m^*}{2\pi\hbar^2} \tag{2.9}$$

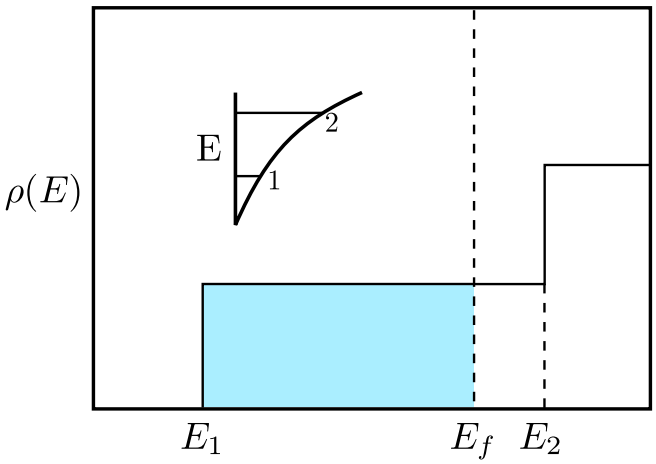

Figure 2-2: *Density of states as a function of energy in a 2DEG.*

which is constant for any energy value inside each subband. The density of electrons per unit area n_s depends on the number of states $n(E)$ and the Fermi-Dirac occupation function, which in its turn depends on the temperature. The Fermi wavevector k_F can be determined as $k_F = \sqrt{2\pi n_s}$

In Figure 2-2 it is shown the energy dependence of the density of states $\rho(E)$ in a 2DEG. The sequence of discrete levels in the potential well that confines the electron in the interface are the lowest energy value of each subband. If the temperatures are low enough, the electron density and therefore the Fermi level will also be low. Sometimes the Fermi level is low enough to have all the electrons contained in the first subband. As the temperature increases, further subband start to become populated.

A magnetic field applied normal to a 2DEG introduces the Landau quantisation of the energy levels, which characterises the third type of electron transport in 2DEGs: quantum Hall regime. The electrons feel a Lorentz force that bends their free trajectories into circular cyclotron orbits. The energy spectrum becomes discrete, thus the cyclotron radius is quantised, since it is proportional to the square root of the energy as in an harmonic oscillator. The energy levels are equivalent to a quantised harmonic oscillator, given as

$$E_n = \left(n + \frac{1}{2}\right)\hbar\omega_c \tag{2.10}$$

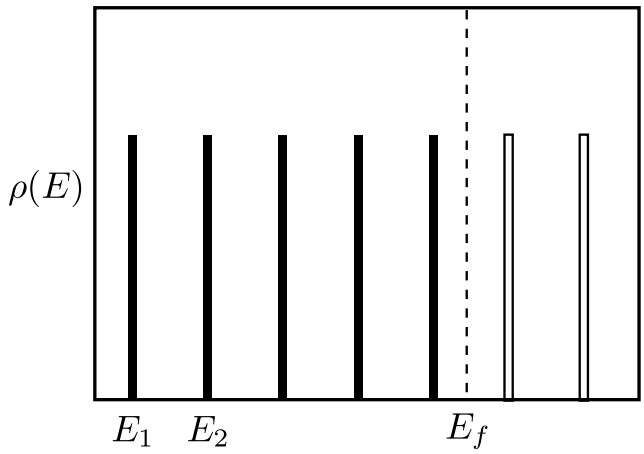

Figure 2-3: *Density of states as a function of energy in a 2DEG in the presence of perpendicular magnetic field. E_1 and E_2 are the energy values of the first two Landau levels.*

where ω_c is the cyclotron frequency given by $\omega_c = eB/m^*$ and n is an integer that labels the Landau levels. The number of states is the same to all Landau levels and equal to one state per flux quantum h/e through the sample. The density of states in this case is illustrated in Figure 2-3

Representing Landau levels as δ-functions corresponds to an ideal case of a collisionless system. According to Equation 2.10, when the magnetic field strength is increased, the spacing between Landau levels is increased as well. Considering the occupied Landau level have energies $E < E_F$, as the field is increased the number of occupied Landau level changes. In a real system, where $n(E)$ has a linewidth, Landau levels can be partially filled.

Consider a rectangular 2DEG with one potential probe in either end of the rectangle and several potential probes along the length of the rectangle, a geometry usually called Hall bar. In a plot of the longitudinal magnetoresistance R_{xx} as a function of the applied field, the resistivity will remain constant at low field but, as the field is increased, shows strong oscillations of B^{-1} periodicity. This is called the Shubnikov-de Haas effect [13]. The minima of the Shubnikov-de Haas oscillations corresponds to a situation where the occupied Landau levels are completely filled and the Fermi level lies between Landau levels. At the Fermi level, the density of states is zero and, therefore, the longitudinal conduction vanishes.

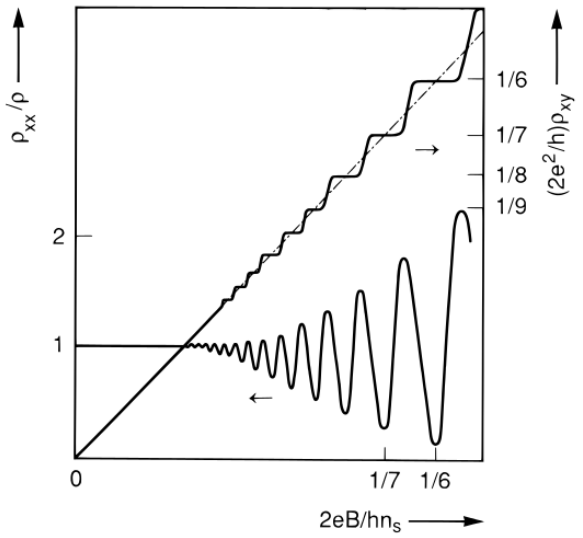

Figure 2-4: *Plot of the longitudinal resistivity ρ_{xx} (normalised to the zero field resistivity ρ) and of the Hall resistivity ρ_{xy} (normalised to the constant $h/2e^2$) as function of the applied magnetic field B (normalised to the constant $hn_s/2e$). It can be observed from the former and latter the Shubnikov-de Haas oscillations and the plateaus in the Hall resistivity, respectively. Figure adapted from Beenakker et al [12]*

If it is given an index i to each minima, the electron density can be determined by plotting the index as function of the periodicity B^{-1}, knowing the index i has the dependence $i = hn_s/eB$. The mobility can be found from the Drude conductivity, by measuring the longitudinal resistance of the 2DEG when no magnetic field is present. It can be converted to a conductivity by knowing the dimensions of the 2DEG.

The resistance measured transversely with respect to the Hall bar is called Hall resistance R_{xy}. It is also dependent of the magnetic field and at low fields $R_{xy} = B/en_s$ [13]. For the same values of magnetic field as the minima of the Shubnikov-de Haas effect, the Hall conductance $R_{xy}^{-1} = (e^2/h)i$ is quantised. Unexpectedly, the Hall resistance R_{xy} registers plateaus at the same position of the Shubnikov-de Haas oscillations. Classically, plotting h/e^2R_{xy} as a function of i would return a straight line of unit slope but R_{xy} is constant in the vicinity of integer i. The quantised Hall conductivity is an expression of the quantum Hall effect. The physical interpretation of the plateaus in the Hall resistance and quantum Hall effect can be found in the literature [12, 13].

2.2 Ferromagnetic order

The response of a given material to a magnetic field [14, 15, 16] is usually characterised by three types of behaviour. In materials which have no permanent magnetic moments due to the absence of unpaired electrons in the outer electronic shell, a magnetisation is induced antiparallel to the applied magnetic field, characteristic of a diamagnetic behaviour. This is a direct manifestation of the Lenz law: electrons in a magnetic field change its trajectory in order to induce a magnetic field which opposes the applied field. All materials have a diamagnetic contribution to their net response to a magnetic field but this contribution is much smaller than the contribution of permanent magnetic moments, if present. Those which have permanent magnetic moments can be organised in two groups: some present a long-range magnetic order below a critical temperature, whereas others do not. The latter refers to paramagnetic behaviour. In thermal equilibrium, if no magnetic field is applied, the magnetic moments are randomly oriented and have no net magnetisation. When a magnetic field is applied, a net magnetisation is induced parallel to the magnetic field, due to a partial alignment of the magnetic moments. This is due to the tendency of the system to dissipate energy through scattering events. If there was no dissipation the magnetic moments would precess indefinitely about the applied magnetic field but, as the energy decreases, the angle between the magnetic moments and the magnetic field decreases until there is parallel alignment.

Within the case of a material containing permanent magnetic moments with long-range order there are several subtypes. The focus will be on the case where the orientation of a magnetic moment is parallel with respect to its nearest neighbours, a behaviour called ferromagnetic. In this case, even when no field is being applied, the magnetic moments are spontaneously aligned parallel to each other inside small regions called domains. In paramagnetics and in thermal equilibrium, the magnetisation of each domain is oriented in a direction which minimises the magnetostatic energy. When a magnetic field is applied, the magnetisation of each domain is aligned parallel with the field, inducing a large net magnetisation. The interaction giving rise to the spontaneous alignment of the magnetic moments is called exchange interaction and will be explained in more detail later

in this section.

The response of a material to a magnetic field can be characterised by the magnetic susceptibility $\bar{\chi}$, which is defined by [15]

$$\vec{M} = \vec{M_0} + \bar{\chi} \cdot \vec{H} \tag{2.11}$$

where $\vec{M}$ is the induced magnetisation and $\vec{M_0}$ is the spontaneous magnetisation when no field $\vec{H}$ is being applied. In general, the susceptibility $\bar{\chi}$ is a tensor but for isotropic materials, the induced magnetisation is parallel or antiparallel to the applied field, therefore the susceptibility is reduced to a scalar. As it was seen above, the diamagnetic behaviour is characterised by an induced magnetisation aligned antiparallel to the applied field. Thus, in isotropic diamagnets the magnetic susceptibility is negative. On the other hand, if there are permanent magnetic moments, the response of the material to an applied field is an induced magnetisation aligned parallel to the applied field, therefore isotropic paramagnets and ferromagnets have positive magnetic susceptibility.

The magnetic moments are aligned inside the domains due to a property of materials with permanent magnetic moments called exchange interaction. The exchange interaction is nonclassical in nature and is based in two fundamental concepts: Coulomb interaction and Pauli exclusion principle. The Pauli exclusion principle states that two electrons cannot be in the same quantum state at the same time. If the orbits of two unpaired electrons from adjacent atoms overlap and if the relative orientation of the spins is parallel, electrons tend to stay far apart, minimising electrostatic energy and making the system more stable. The exchange interaction is felt as an effective field, which will be referred to in this text as exchange field B_E. The exchange field [16] is proportional to the induced magnetisation

$$\vec{B}_E = \lambda \vec{M} \tag{2.12}$$

where λ is a constant. There is a dipolar interaction between magnetic moments but it is overshadowed by the exchange field which can be of the order of 1000

T. The exchange interaction competes with thermal agitation which destroys the magnetic order at high enough temperatures.

Going back to the definition of magnetic susceptibility (Equation 2.11) in the paramagnetic phase and adding the exchange field which is created when the magnetisation is induced

$$M = \chi_p(B_a + B_E) \tag{2.13}$$

where B_a is the applied magnetic field. The Curie law defines the paramagnetic susceptibility [16] as

$$\chi_p = \frac{C}{T} \tag{2.14}$$

where C is the Curie constant and T is the temperature of the sample. By combining Eqs. 2.12, 2.13 and 2.14, it is obtained

$$M = \frac{CB_a}{T - C\lambda} \tag{2.15}$$

Considering the response to the applied magnetic field, using Equation 2.15, the susceptibility in this case becomes

$$\chi = \frac{M}{B_a} = \frac{C}{T - C\lambda} \tag{2.16}$$

It is easily concluded that the susceptibility is infinite at $T = C\lambda$. The physical meaning of this result is that there will be a magnetisation even if the applied field is zero, *i.e.*, a spontaneous magnetisation. The temperature $T_c = C\lambda$ is the critical temperature that distinguishes between the paramagnetic and ferromagnetic phases and is called Curie point. Although the Curie-Weiss model (Equation 2.16) does not predict it mathematically, spontaneous magnetisation also occurs below the Curie point, but as it was pointed before, the treatment presented above is only valid for the paramagnetic phase.

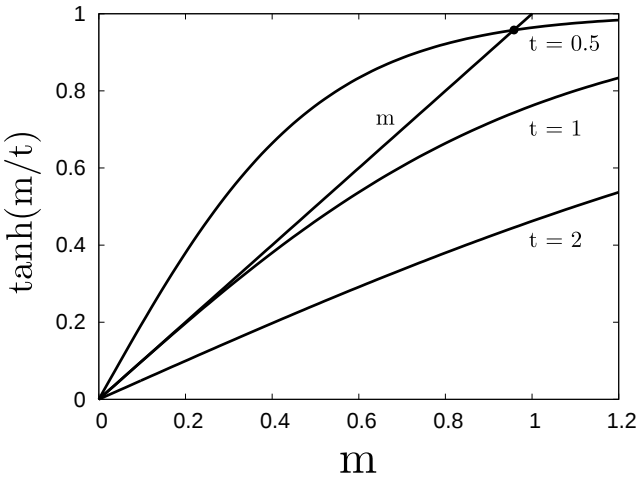

Figure 2-5: *Graphical solution of Equation 2.18 for the reduced magnetisation m as a functions of the reduced temperature t.*

To find the spontaneous magnetisation as a function of the temperature below the Curie point, an expression derived from the Brillouin function will be used instead. For the case of total spin $J = 1/2$ and setting the applied field B_a to zero [16],

$$M_0 = N\mu \tanh\left(\frac{\mu\lambda M}{k_B T}\right) \tag{2.17}$$

where N is the total number of atoms and μ is the projection of the magnetic moment parallel to the exchange field. Being transcendental, the solutions of the Equation 2.17 must be found graphically [16]. By reducing Equation 2.17 to

$$m = \tanh(m/t) \tag{2.18}$$

where $m = M/N\mu$ and $t = k_B T/N\mu^2\lambda$.

In Figure 2-5 it is plotted m and $\tanh(m/t)$ for $t = 0.5, 1, 2$ as a function of m. For $t = 2$, the curve only intersects the m line at $m = 0$, meaning there is no spontaneous magnetisation at this value of temperature, consistent with the paramagnetic phase. The curve with $t = 1$ is tangent to the m line, which means it corresponds to the temperature at the onset of the ferromagnetic phase, and

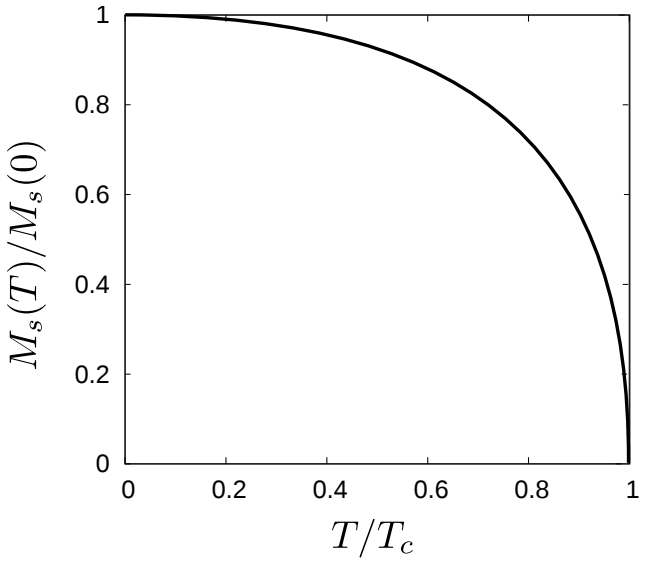

Figure 2-6: *Saturation magnetisation as a function of the temperature.*

finally the curve $t = 0.5$ which intersects at approximately $M = 0.98N\mu$, which is the spontaneous magnetisation. The reduced temperature is $t = T/T_c$ and the Curie point is therefore given by $T_c = N\mu^2\lambda/k_B$. If enough points are extracted by this method, the plot shown in Figure 2-6 with $M_s(T)/M_s(0)$ as a function of T/T_c can be made. It can be observed at $T/T_c \to 0$ the magnetisation saturating at the maximum value and the magnetisation gradually decreasing until it reaches the Curie point and becomes zero.

The tabulated values for the saturation magnetisation of dysprosium and cobalt are 3.667 and 1.81 T, respectively.

2.3 Magnon dispersion relation

An analysis from an energetic point of view of a one dimensional array of N magnetic moments is going to be presented [16, 15]. The energy of the system is the sum of the exchange interaction between nearest neighbours and is given by the Hamiltonian

$$U = -2\mathcal{J}\sum_{p=1}^{N}\vec{S}_p \cdot \vec{S}_{p+1} \tag{2.19}$$

where $\mathcal{J}$ is the exchange integral and $\hbar\vec{S}_p$ is the angular momentum of the magnetic moment p. The angular momentum $\hbar\vec{S}_{p+1}$ refers to the nearest neighbour of magnetic moment p. The Hamiltonian is based on the Heisenberg model, which describes the energy of interaction between two magnetic moments. Considering that the system is in the ground state when all the magnetic moments are parallel; in such state, $\vec{S}_p \cdot \vec{S}_{p+1} = S^2$ and the exchange energy is $U_0 = -2N\mathcal{J}S^2$. On the other hand, considering that one magnetic moment is reversed in the array, it can be seen from Equation 2.19 that the energy for this state would be higher by $8\mathcal{J}S^2$ than the energy of the ground state. It would be more efficient energetically if all magnetic moments participated in the excitation. In fact, the orientation of the magnetic moments oscillate collectively as an oscillatory system coupled by the exchange interaction. Such systems are called spin waves. The ends of the magnetic moment vectors precess in circles, being dephased by a constant angle in relation to their nearest neighbours.

The dispersion relation for spin waves in one dimensional arrays with nearest neighbour interaction is derived, for example, by Kittel [16]. The result is

$$\hbar\omega = 4\mathcal{J}S(1 - \cos ka) \tag{2.20}$$

where a is the period of the array and k is the wavevector of the spin wave mode.

The dispersion relation is plotted in Figure 2-7 within the range $0 \leq k \leq \pi/a$. The limits of the range correspond to the state where all magnetic moments are oscillating in phase and out of phase, respectively.

2.4 Magnetocrystalline anisotropy

The energy spent magnetising a sample depends on the orientation of the magnetisation vector [14]. The most energetically favourable direction is called easy

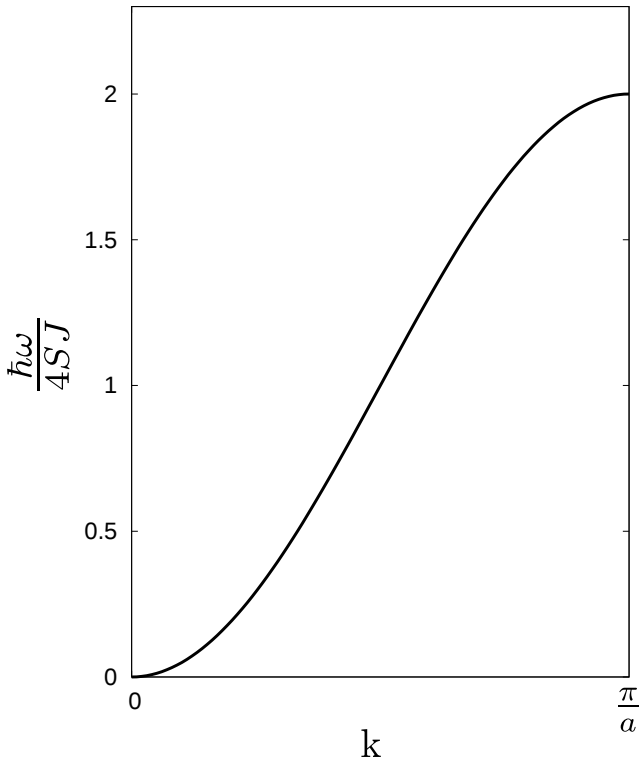

Figure 2-7: *Dispersion curve for magnons in a ferromagnet in one dimension.*

axis, whereas the less favourable direction is called hard axis. When no field is being applied, the spontaneous magnetisation points towards the easy axis. On the other hand, if the magnetisation vector is required to be oriented in another direction, an external field must be applied. Accordingly, the applied field needed to saturate the magnetisation along the easy axis is smaller in comparison to other orientations, whereas it is larger along the hard axis. This property is dependent on the crystallographic symmetry of the ferromagnetic material.

The physical origin behind this phenomena is related to electron orbitals around the ions at the crystalline lattice sites are not spherically symmetric. Thus, the interaction between the spin and orbital angular moment varies according to the orientation and affects the energy in the magnetisation process.

Both materials used in the experimental part have a crystal lattice with hexagonal symmetry. The easy direction of magnetisation is the axis perpendicular to the basal plane, usually referred in the literature as the hexagonal axis. Any direction belonging to the basal plane is an hard axis. Since materials with hexagonal

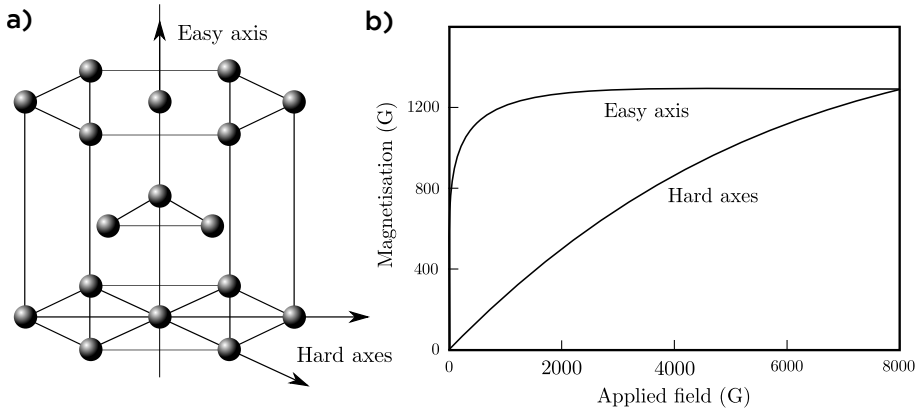

Figure 2-8: *a) HCP lattice structure of cobalt showing the easy and hard magnetisation axes; b) Magnetisation curves of cobalt when magnetised along the easy and the hard axes. Based on Figure 6.1 from O'Handley [14].*

symmetry only have one easy direction they are called uniaxial.

In the Figure 2-8 a) the easy and hard axes are shown in the case of uniaxial anisotropy. The applied field dependence of the magnetisation is plotted in b), comparing both cases of magnetisation along the easy and hard direction and it can be verified the quick saturation when magnetisating in the easy axis.

The uniaxial anisotropy energy density needed to saturate the magnetisation in any given direction is defined as the energy needed to saturate the magnetisation in the basal plane minus the energy needed to saturate the magnetisation along the easy axis. The energy density can be estimated as the area between the magnetisation curves referring to both directions, roughly half the area of the rectangle limited by the saturation magnetisation and the anisotropy field H_a. There are approximated energy functions determined for each material, usually in the form of series expansions. The uniaxial anisotropy energy density [14] is given by a power series of the form

$$u_a = \sum_n K_n \sin^{2n} \theta \tag{2.21}$$

where K_n is the contribution to the uniaxial energy density of nth order and θ is the angle the magnetisation vector does with the easy axis. It is usually enough to consider only the first three terms. The leading term is isotropic since it does

not depend on the angle, therefore it becomes $u_a = K_1 \sin^2\theta + K_2 \sin^4\theta$.

Magnetocrystalline anisotropy can be quantified by the anisotropy field H_a. The anisotropy field is defined as the field needed to saturate the magnetisation along the hard axis. After being saturated, a finite magnetisation remains when the applied field is switched off. That magnetisation is called remanence. Remanence is larger if the magnetisation lies along the easy axis and is smaller or zero along the hard axis.

2.5 Spin 1/2 particle in a magnetic field

To study how spins evolve with time when they are in magnetic resonance, being either electron spins organised with paramagnetic or ferromagnetic order or nuclear magnetic moments, one must revisit the fundamental picture of a spin 1/2 particle in a uniform magnetic field. A classical description follows. Consider a spin carrying magnetic moment $\vec{\mu}$ and angular momentum $\vec{S}$. If both vectors are parallel, they are related by $\vec{\mu} = \gamma\vec{S}$. The constant γ is called gyromagnetic ratio and is given by[1] $\gamma = -g\mu_B/\hbar$, where g is the Landé g-factor.

If such spin is under a static magnetic field (Figure 2-9), it will sense a torque given by $\vec{\tau} = \vec{\mu} \times \vec{B}_{dc}$. From classical mechanics, a torque is equal to the first time-derivative of the angular momentum. Additionally, by multiplying both sides of the equation with γ, it is obtained

$$\frac{d\vec{\mu}}{dt} = \gamma\vec{\mu} \times \vec{B}_{dc} \tag{2.22}$$

which is the equation that describes the precession of a magnetic moment $\vec{\mu}$ about the static magnetic field $\vec{B}_{dc}$. If the tail of the vector of the magnetic moment is "fastened" to the origin of a Cartesian coordinate system and the static magnetic field is given by $\vec{B}_{dc} = B_0\hat{z}$, the tip of the magnetic moment will describe circles around $\vec{B}_{dc}$ in a plane parallel to $x0y$ plane.

[1]The Bohr magneton μ_B is used for the case of electrons. For nuclear magnetic moments, the nuclear magneton μ_N is used instead.

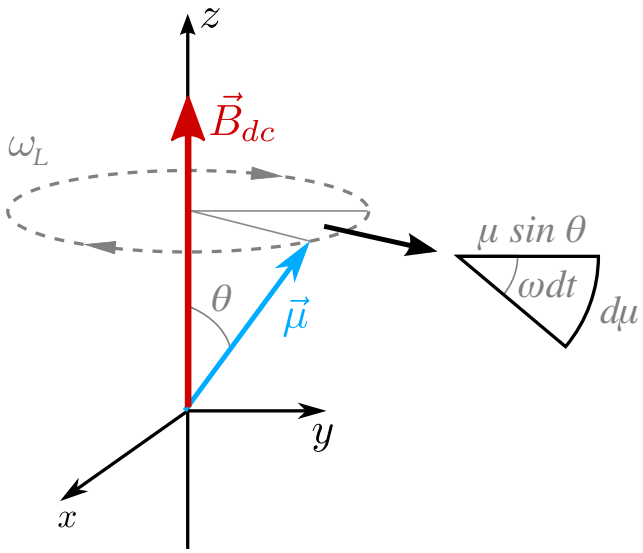

Figure 2-9: *Magnetic moment $\vec{\mu}$ in Larmor precession when subjected to a static magnetic field*

If the magnetic moment vector describes a small arc of circumference $d\vec{\mu}$, like in Figure 2-9, the corresponding phase angle of the rotation is given by ωdt. The radius of the circumference done by the tip of the magnetci moment vector is $\mu \sin\theta$, where θ is the angle of the cone done by the magnetic moment vector. Therefore, $d\vec{\mu} = \mu \sin\theta \omega dt$. From Equation 2.22,

$$\gamma \vec{\mu} \times \vec{B}_{dc} = \mu \sin\theta \omega \tag{2.23}$$

Since the angle between vectors $\vec{\mu}$ and $\vec{B}_{dc}$ is θ, the vector product can be simplified and thus

$$\gamma \mu B_{dc} \sin\theta = \mu \sin\theta \omega \tag{2.24}$$

The frequency of precession is therefore given by the condition $\omega_L = \gamma B_{dc}$. The frequency ω_L and the static magnetic field $\vec{B}_{dc}$ are called the Larmor precession frequency and Larmor field, respectively.

Lets now consider the influence of a time-dependent magnetic field $\vec{B}_{ac}$ applied perpendicular to the Larmor field $\vec{B}_{dc}$, thus rotating in the $x0y$ plane, and whose

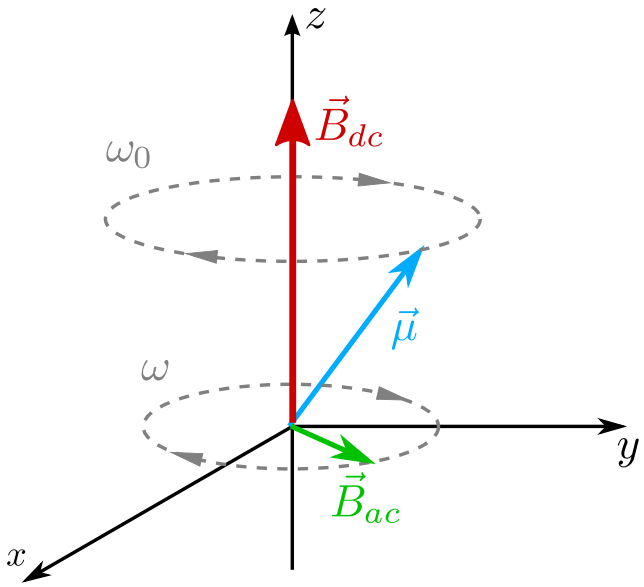

Figure 2-10: *Magnetic moment $\vec{\mu}$ in Larmor precession when subjected to crossed dc and ac magnetic fields.*

magnitude is much smaller than the magnitude of $\vec{B}_{dc}$. A field with the specifications provided above is appropriate to model a circularly polarised electromagnetic wave irradiating a sample. The *ac* field induces an *ac* response from the magnetic moment. It is convenient to write the total field and total magnetic moment as a sum of *dc* and *ac* components [17], therefore where there was before $\vec{B}_{dc}$ and $\vec{\mu}$ in Equation 2.22, both vectors are replaced by the sums $\vec{B}_{dc}+\vec{B}_{ac}$ and $\vec{\mu}_{dc}+\vec{\mu}_{ac}$, respectively. Neglecting vector products between *ac* components and knowing $\vec{\mu}_{dc}\times\vec{B}_{dc}=0$, because the two vectors are aligned parallel to the z axis, Equation 2.22 becomes

$$\frac{d\vec{\mu}_{ac}}{dt}+\gamma\vec{\mu}_{ac}\times\vec{B}_{dc}=-\gamma\vec{\mu}_{dc}\times\vec{B}_{ac} \tag{2.25}$$

Using the same kind of dependence for $\vec{\mu}_{ac}$ as the one used in Equation 2.22, projecting onto the axes of the Cartesian system

$$\begin{cases} i\omega\mu_{ac,x}+\gamma B_{dc}\mu_{ac,y}=\gamma\mu_{dc}B_{ac,y} \\ -\gamma_{dc}\mu_{ac,x}+i\omega\mu_y=-\gamma\mu_{dc}B_{ac,x} \\ i\omega\mu_{ac,z}=0 \end{cases} \tag{2.26}$$

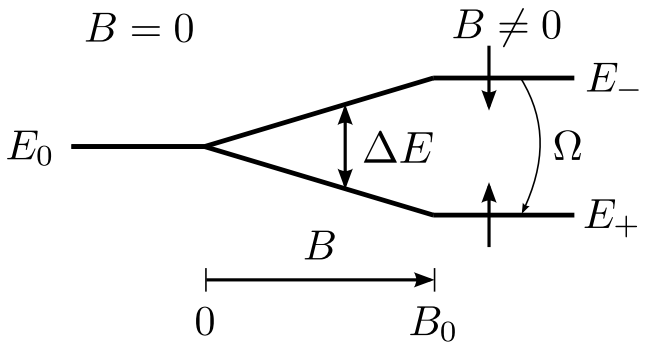

Figure 2-11: *Energy diagram of Zeeman splitting of spins the presence of a magnetic field.*

The solution of the system is given by

$$\begin{cases} \mu_{ac,x} = \chi B_{ac,x} + i\chi_a B_{ac,y} \\ \mu_{ac,y} = -i\chi_a B_{ac,x} + \chi B_{ac,y} \\ \mu_{ac,z} = 0 \end{cases} \tag{2.27}$$

where χ and χ_a are components of the high-frequency magnetic susceptibility tensor and are given by

$$\chi = \frac{\gamma \mu_{dc} \omega_L}{\omega_L^2 - \omega^2} \,, \qquad \chi_a = \frac{\gamma \mu_{dc} \omega}{\omega_L^2 - \omega^2} \tag{2.28}$$

where ω_L is the Larmor precession frequency. Eqs. 2.28 have a singularity at $\omega = \omega_L$, which makes χ and χ_a grow to infinity. When both the Larmor frequency and the frequency of the *ac* magnetic field are matched, there is resonant absorption of electromagnetic energy by the system.

In the picture of Zeeman interaction (Figure 2-11), when no magnetic field is present, there is no distinction between particles of different spin orientation, therefore these are all degenerate states at the same level. When the magnetic field is applied, it interacts with the magnetic moment of the particle, lifting the spin degeneracy and splitting the original level into two different states: one for particles with $S = +1/2$ (spin "up", parallel) and another for $S = -1/2$ (spin "down", antiparallel). These two states are equally displaced from the original energy value and their gap is the energy correspondent to the frequency where

resonant absorption occurs in the example shown above, $\Delta E = \hbar\omega_L$. Therefore the states have an energy given by

$$E_{\pm} = E_0 \pm \frac{1}{2} g\mu_B B_0 \tag{2.29}$$

where E_0 is the energy at $B_0 = 0$. The Bohr magneton is used here assuming the S = 1/2 particles are electrons. The sign of the g-factor is important because it determines which are the lower and higher energy states. In the case of GaAs, the g-factor is $g = -0.44$ and thus the spin "up" has lowest energy.

When the system is in magnetic resonance, the spin flips to the higher energy state and, if the resonance conditon is kept, instantaneously decays to the lower state with stimulated emission. The system will oscillate with transitions between these two states with a rate dependent of the magnitude of the *ac* magnetic field. This is called Rabi frequency and it is given by $\Omega = \gamma B_{ac}$. Vectorially, the magnetic moment $\vec{\mu}$ will also oscillate along the z axis and if the z component of $\vec{\mu}$ is plotted as a function of time, it will result in a sinusoidal function with frequency equal to the Rabi frequency Ω.

2.6 Shape anisotropy

The last section described the dynamics of a single spin in an isotropic medium in conditions of magnetic resonance. As it was seen before, in a medium ordered ferromagnetically, the spins align spontaneously and the macroscopic picture of magnetisation can be used, which is the sum of all magnetic moments per unit volume. The mathematical treatment of the previous section would return the same results if the magnetic moments μ are substituted by magnetisations and the angular momentum by an angular momentum density, in an isotropic ferromagnet.

Experimentally, the resonance condition $\omega = \omega_L$ is valid only in a special case: a sample with spherical shape. The present section will show that the shape of the sample plays an important role [16, 17].

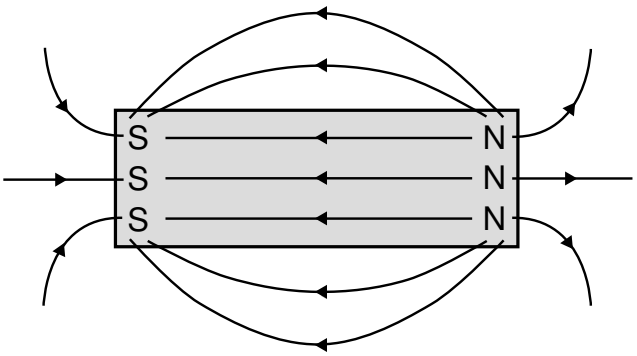

Figure 2-12: *Bar magnetised from left to right will have magnetic poles created at each each of the bar. The two poles induce a new field with opposite direction with respect to the magnetisation and magnitude proportional to the magnetisation.*

If a magnetic field is applied from left to right to a ferromagnetic bar, a magnetisation forms in the same direction inside the bar. Magnetic poles are created at each end of the bar and therefore a magnetic field will be induced from north to south pole. This magnetic field has a magnitude proportional to the magnetisation vector and is called demagnetising field because it opposes the applied magnetic field and reduces the magnetic field inside the sample. Its proportionality constant in relation to the magnetisation vector is given by the demagnetising tensor $\vec{N}$. The demagnetisation tensor $\vec{N}$ is given for this case by

$$\vec{N} = \begin{bmatrix} N_x & 0 & 0 \\ 0 & N_y & 0 \\ 0 & 0 & N_z \end{bmatrix}$$

The internal magnetic field felt by the spins inside the sample is therefore the sum of the applied field with the demagnetising field $\vec{H}^i = \vec{H}^e + \vec{H}^{dem}$, where $\vec{H}^{dem} = -\vec{N}\vec{M}$.

Demagnetising fields have great significance in ferromagnets because the magnetisation is strong, usually close to saturation, therefore inducing strong demagnetising fields also. The definition of demagnetising field and the derivation of a new resonance condition will be made assuming the sample shape is an ellipsoid. Samples with ellipsoidal geometry have a useful property: if the applied field is homogeneous, the magnetisation and the internal field are homogeneous as well.

The elements of the diagonal N_x, N_y and N_z are called demagnetising factors and are the proportionality constants relating the demagnetising field and magnetisation along the respective directions. The demagnetisation factors are only dependent of the sample geometry - formulas are provided in *Craik* [33] - and its sum is $N_x + N_y + N_z = 1$.

Before writing the equation of motion and deriving the resonance condition, the *ac* and *dc* components of the total magnetic field acting on the spin must be rewritten to take the demagnetising field into account. The *dc* component of the total magnetic field acting on the spin is given by

$$\vec{H}_{dc} = \vec{H}^e_{dc} - \vec{N}\vec{M}_{dc} \tag{2.30}$$

where $\vec{H}^e_{dc}$ is the *dc* component of the applied magnetic field. The *ac* component of the internal field is going to be disregarded since there is no interest in determining the magnetic response to an *ac* magnetisation. In order to find the resonance condition one only needs to determine the frequency of free oscillations. Appropriate adjustments must be done to Equation 2.25 in previous section to incorporate the internal field given by Equation 2.30. Vector products between *ac* vectors are neglected again. The vector product between the *dc* magnetisation and the *dc* internal field are parallel along the z axis, $\vec{M}_{dc} \times (\vec{H}^e_{dc} - \vec{N}\vec{M}_{dc}) = 0$, thus it is obtained

$$\begin{aligned} &i\omega M_{ac,x} + \gamma\mu_0(H^e_{dc} - N_z M_{dc} + N_y M_{dc})M_{ac,y} = 0 \\ &-\gamma\mu_0(H^e_{dc} - N_z M_{dc} + N_x M_{dc})M_{ac,x} + i\omega M_{ac,y} = 0 \end{aligned} \tag{2.31}$$

Solving the system 2.31, the frequency of the free oscillations of the magnetisation vector is given by the following condition

$$\omega = \gamma\mu_0\sqrt{[H^e_{dc} - (N_x - N_z)M_{dc}][H^e_{dc} - (N_y - N_z)M_{dc}]} \tag{2.32}$$

If the *ac* magnetic field frequency is matched to the frequency of free oscillations in Equation 2.32, ferromagnetic resonance will occur.

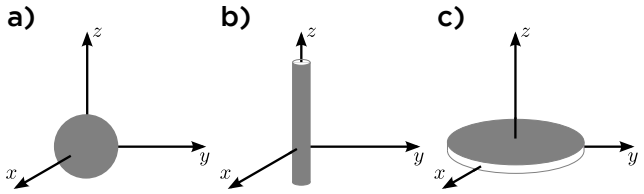

Figure 2-13: *Limiting cases of an ellipsoidal specimen: a) sphere; b) rod of infinite length and very small radius (prolate) and c) disk of inifinite radius and very small thickness (oblate).*

As it was mentioned above, the frequency of resonance of a sample with spherical geometry is given by $\omega = \gamma\mu_0 H^e_{dc}$ because the demagnetising factors are all equal $N_x = N_y = N_z = 1/3$. This is one of the three limiting cases (Figure 2-13). Ellipsoids are characterised as prolate or oblate according to the ratio between the axes of the ellipsoid. In a prolate ellipsoid the axis of revolution is the longest, whereas in a oblate ellipsoid it is the shortest. The limiting case of a prolate ellipsoid is an infinitely long rod pointed along the z axis, whose demagnetising factors are $N_x = N_y = 1/2, N_z = 0$ and frequency of resonance is $\omega = \gamma\mu_0(H^e_{dc} + M_{dc}/2)$. The limiting case of oblate ellipsoid is the infinite plane $x0y$, whose demagnetising factors are $N_x = N_y = 0, N_z = 1$ and frequency of resonance is $\omega = \gamma\mu_0(H^e_{dc} - M_{dc})$.

All magnets in the samples measured in the experiments described in this Thesis do not have ellipsoidal geometry, being rectangular prisms instead. Ellipsoidal specimens have, an uniform internal field all over the whole sample, therefore there is only need to determine one set of demagnetising factors for the whole sample. On the other hand, unlike ellipsoids, non-ellipsoidal specimens have an inhomogeneous internal field. If the demagnetising field depends on the position inside the sample, the demagnetising factors will have the same dependence. In terms of frequency of resonance, the condition is the same (Equation 2.32), but the demagnetising factors must be calculated differently. The formulas are provided in Appendix A to calculate demagnetising factors of rectangular prisms.

2.7 Dynamic nuclear polarisation in GaAs crystal lattices

As with the electron spins, nuclear spins of the ions located in a lattice have a tendency to align with an external magnetic field [18, 19]. However, the nuclear magnetic moment is approximately 2000 times smaller than the magnetic moment of the electron spin ($\sim$ one Bohr magneton), therefore even with an external magnetic field with a magnitude of 100 T at a temperature of 1 K, it would be achieved a nuclear polarisation of the order of 1%. Higher levels of nuclear polarisation can be achieved via hyperfine interaction with electron spins in non-equilibrium. The description of such processes belongs to a section of nuclear magnetism called dynamic nuclear polarisation. Dynamic nuclear polarisation is essentially the transfer of angular momentum from the electron spin to the nuclear spin. The total angular momentum (electrons + nuclei) is conserved by the hyperfine interaction. Hyperfine interaction, the coupling between the electronic and nuclear spins is characterised by an Hamiltonian H_{hf} given by

$$H_{hf} = \sum_n a_n(\vec{s} \cdot \vec{I}_n) \tag{2.33}$$

where $a_n = v_0 A_n |\Psi(\vec{r}_n)|^2$, v_0 is the volume of the unit cell, $\Psi(\vec{r}_n)$ is the electron density at the nth nucleus position $\vec{r}_n$, $\vec{I}_n$ is the nuclear spin of the nth nucleus and A_n is the hyperfine constant. The hyperfine constant A_n is of the order of 100 μeV in GaAs-based semiconductors.

If there is a finite average polarisation of the nuclei, the hyperfine interaction is expressed by an effective field created at the nuclei which influences the electrons. This nuclear field is given by

$$B_N = \frac{v_0 \sum_\eta A_\eta \langle \vec{I}_\eta \rangle}{\mu_B g_e} \tag{2.34}$$

Since the field B_N is a sum all over the nuclear species composing the lattice, η labels the species, $\langle \vec{I}_\eta \rangle$ is the average spin of the nuclei of species η and g_e is the

electron g-factor. In GaAs, $B_N = 5.3$ T [9].

Many processes can lead to dynamic nuclear polarisation but the most relevant in the context of this Thesis is usually referred as "solid effect" in the literature authored by Abragam [19]. It consists of a process involving nuclear spins being polarised when microwaves are applied with frequency equal to the Larmor frequency of the electrons, where the nuclear polarisation can become comparable to the magnitude of the polarisation of the electrons. The solid effect can be explained qualitatively, under many assumptions, as follows. Consider a number of nuclear spins $I = 1/2$ with Larmor frequency ω_I in the crystal lattice of a diamagnetic solid which has paramagnetic impurities with electron spins $S = 1/2$ of Larmor frequency ω_S, coupled with the nuclear spins through hyperfine interaction. Setting the magnetic field H and temperature T such that all electron spins "S" are polarised, for example, all pointing "up" and the nuclear spins I all unpolarised, with same population of "up" spins as "down" spins. The hyperfine interaction allows simultaneous reversals of S and I in opposite directions, which will be called flip-flops [19], and reversals in the same direction, which can be called flip-flips [19], for example. The relaxation rate of nuclear spins is small at low temperatures, $1/T_n \sim 10^{-3}$ Hz, whereas the relaxation rate of one electron spin is much faster, $1/T_e \sim 10^3$ Hz. Irradiating the sample with microwaves, can induce flip-flops at a frequency of $\Omega = \omega_S - \omega_I$ or flip-flips at $\Omega = \omega_S + \omega_I$. Assume the linewidth $\Delta\omega_S \ll \omega_I$ so that when exciting flip-flops, it is ensured flip-flips are forbidden because they are off-resonance with Ω, and vice versa. Finally, assume that when flip-flops are induced, the amplitude of the magnetic field component of the microwaves is such that the Rabi frequency of the flip-flop cycling is much greater than the nuclear relaxation rate but smaller than the electron relaxation rate.

Consider now that one of the nuclear spins I is "up" and all the electron spins S are "up". The frequency is set to induce flip-flops but this spin can only be reversed by following all spins S downwards, a flip-flip, which is forbidden. Therefore, only a spin I which is "down" is allowed to reverse via flip-flop transition, ending in an "up" position while spins S are all "down". The population of nuclear spins I pointing "up" is now equal to the population of spins I "down" plus two. This same spin I which is now "up" could come back down to the

original position, balancing the populations of spins I "up" and "down", through a flip-flop with spins S all "down". As it was seen above, the relaxation rate of the electrons is quicker than the Rabi frequency of subsequent flip-flops. Therefore, before the flip-flop transition that would send the spins to the original state, the spins S relaxate back to the "up" position and the next transition will bring another spin I "down" upwards, increasing the polarisation $\langle \vec{I}_n \rangle$. Eventually all spins I would be brought "up".

If flip-flips were being induced with $\Omega = \omega_S + \omega_I$, it is easy to see that all spins I would go "down" with a polarisation opposite to that of the spins S. If the electrons were not completely polarised, $\langle S_n \rangle < 1$, it is also easy to see following the same logic that the nuclear polarisation would end up being $\langle I_n \rangle = \pm \langle S_n \rangle$.

Chapter 3

Experimental setup

This chapter is divided into two sections. First, it will be presented the main specifications of the samples and it will be described how the fabrication start from a wafer of the heterostructure to a device packaged in a chip carrier ready to be measured. In the other half, the entire measurement procedure will be described, i.e. subjecting the sample to the desired conditions, data acquisition and further details.

3.1 Samples

Hybrid devices were fabricated from a GaAs/$Al_{0.33}Ga_{0.67}As$ single heterojunction, grown by molecular beam epitaxy by Semiconductor Physics group at the University of Cambridge. The mobility and density of the 2DEG were determined from quantum transport measurements as $\mu = 1.5 \times 10^6 cm^2 V^{-1} s^{-1}$ and $n_s = 1.6 \times 10^{11} cm^{-2}$. Hall bars with nominal dimensions of $8 \times 32 \mu$m were patterned by optical lithography. The Hall bar (Figure 3-2) is a type of structure which have a convenient geometry to study quantum transport. It is comprised of a rectangular active region and several arms located at each end of the structure and along the longest edge of the rectangle at each side, which can be used as voltage probes or as terminals used to supply current to the device. The voltage probes were separated by distances ranging from 2 μm to 16 μm. Ferromagnetic

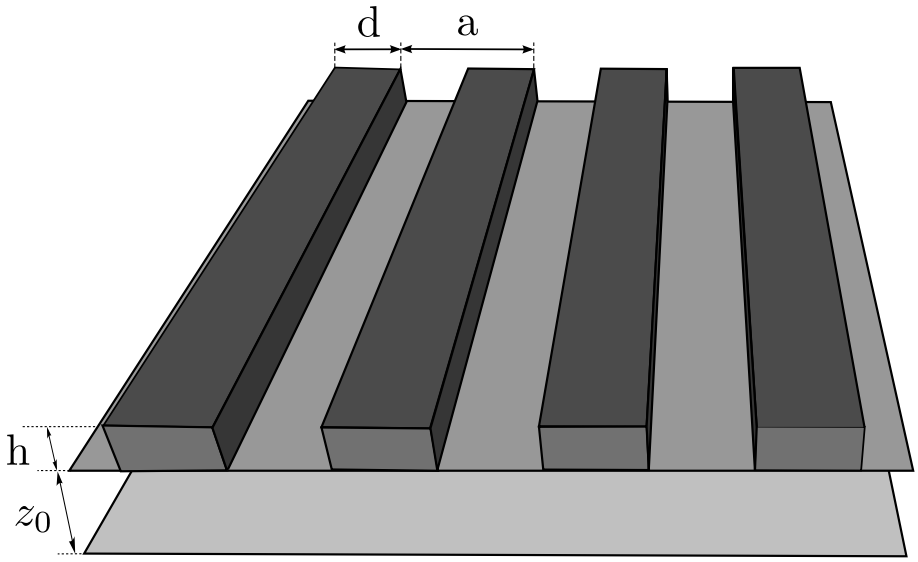

Figure 3-1: *Schematic of an heterostructure with a grating deposited on top. Labels of the dimensions of the grating are represented.*

Sample	*A*	*B*	*C*	*D*
Magnet	Dy,Co stripe	Dy grating	Dy grating	Co grating
a	N/A	400	300	400
d	200	200	210	200
h	150	160	80	150
z_0	90	90	90	90

Table 3.1: *Device parameters. Dimensions are in nm. As it can be seen from Figure 3-1, a, d, h and z_0 correspond to the magnetic superlattice period, stripe width, stripe thickness and distance between the 2DEG plane and the heterostructure surface.*

gratings and individual stripes were then fabricated at the centre of Hall bars to modulate the 2DEG located at 80nm below the surface (Figure 3-6).

Measurements were made in four different types of device, listed in Table 3.1. Samples of type A had a single dysprosium (or cobalt) stripe shown in Figure 3-3. Samples B-D were 1D arrays made with two different materials and two different lattice periods, such as the one shown in Figure 3-4. The use of gratings of different pitch allows varying dipolar coupling and studying its effect on the high frequency dynamics. Dysprosium was used because it has the highest magnetic moment per atom which maximises the coupling between stripes. The tabulated

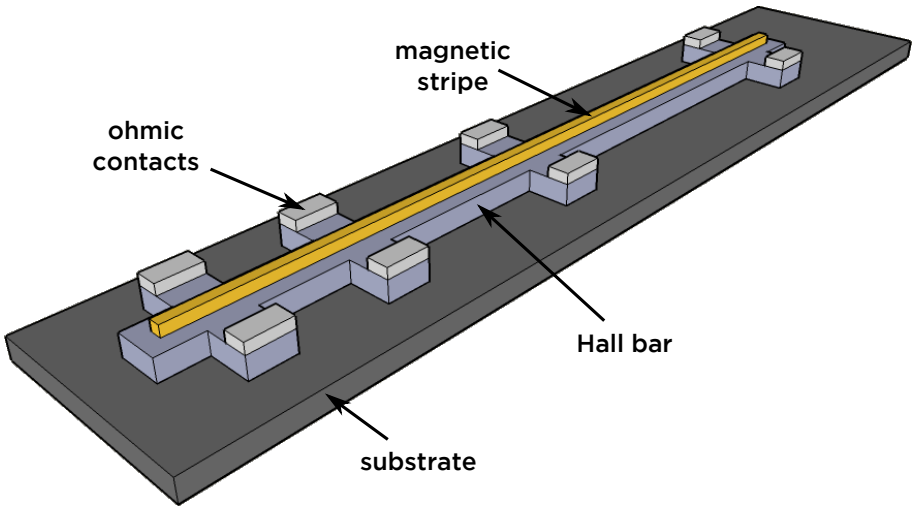

Figure 3-2: *Schematic of a single magnetic stripe device.*

values of the saturation magnetisation at 4 K are $\mu_0 M_s = 3.67$ T (Dy) and $\mu_0 M_s = 1.84$ T (Co). In all devices, the stripes exceeded the length of the Hall bar by 10μm at each end, and effectively behaved as stripes of infinite length. Similarly, the gratings overlapped the active area of the Hall bar plus 10μm on each side. The lack of edge effects allowed to consider the grating as being infinite.

The devices were processed in the David Bullett Nanofabrication Facility at the University of Bath, in a class-1000 clean room. Photolithography techniques were used to pattern arrays of Hall bars in the substrate wafer. The substrate was then immersed in the etchant to etch the exposed regions deeper than the interface where the 2DEG is located, well into the GaAs layer, to shape the 2DEG as desired. To add ohmic contacts to the devices, another sequence of photolithographic steps were used to define the area where the contacts were to be deposited on top of the substrate. A few layers of gold and germanium were then deposited all over the substrate by thermal evaporation. Next, the lift-off of the remaining photoresist was performed in order to remove the thin-film in unwanted areas. After the evaporation, the contacts were annealed in an oxygen-free atmosphere to make contact with the 2DEG. Finally, to apply inhomogeneous magnetic fields to the 2DEG, micromagnets were deposited above the channel of the Hall bar. Since a much higher resolution was needed for the feature size of the stripes (of the order of 100 nm), electron beam lithography was employed instead. The magnetic materials were then deposited by thermal evaporation,

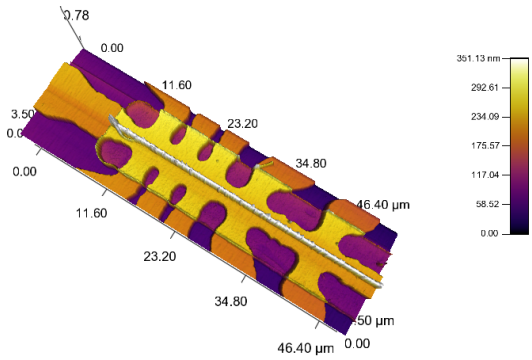

Figure 3-3: *AFM micrograph of a single stripe sample.*

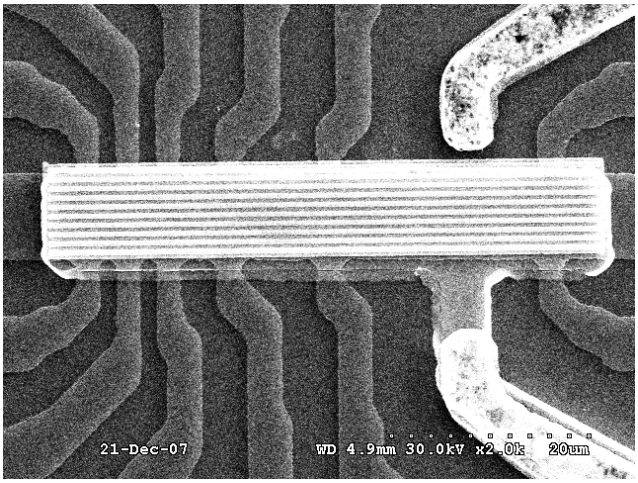

Figure 3-4: *SEM micrograph of a magnetic superlattice sample.*

followed by a lift-off process. The wafer was then cleaved into chips with a single device.

Before being ready for measurement, the samples must be mounted on a chip carrier. The samples are small, fragile and hard to handle at a macroscopic scale. The chip carriers are 1 cm^2 ceramic tiles with several gold pads where wires can be soldered to. The sample is fixed to the chip carrier using GE varnish - a material that keeps its adhesive properties at very low temperatures. To make connections between ohmic contacts in the sample and the contacts in the chip carrier, an ultrasonic bonding machine was used. This bonding machine does a more precise soldering using 12.5 μm wires. A wedge shaped needle applies ultrasonic pulses to bond the wires to the contacts by thermocompression.

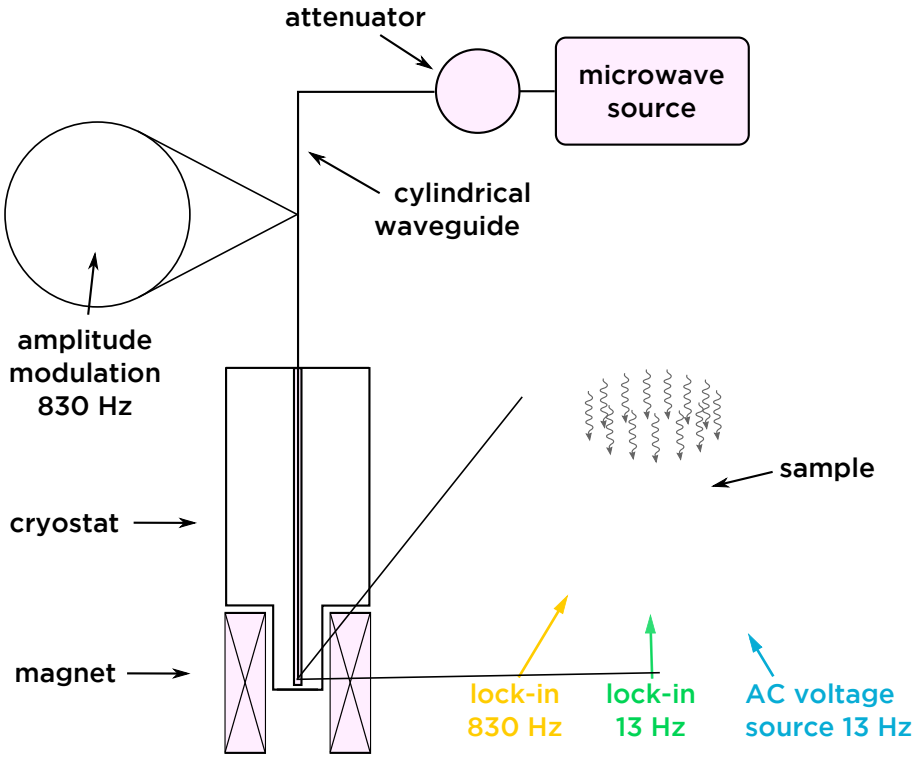

Figure 3-5: *Schematic of the experimental setup used in the measurement of magnetoresistance while being irradiated by microwaves.*

3.2 Experiments

The experiments involved measuring the magnetoresistance between two voltage probes of the Hall bar. The experimental setup is depicted in Figure (3-5) Magnetoresistance is the property of a material to change its resistivity when an external magnetic field is applied to it. Therefore, in order to study this property the sample must be subjected to a variable, static magnetic field. A superconducting solenoid capable of producing an output of 15 T was used for that purpose. The regimes of electron transport that were going to be induced - quantised transport for 2DEG characterisation and ballistic transport for the remainder of the results - are only accessible at very low temperatures. Additionally, for the magnetic materials to be of any use, these need to be operating in the ferromagnetic phase, which occurs at a temperature lower than the Curie point, as it was seen in the previous section. For the above reasons, it was needed a way to cool down the sample to temperatures near 1.3 K and a way of controlling

the temperature, since there was also interest in studying temperature dependences. The samples were therefore inserted in a cryostat with liquid Helium, which brought the temperatures down to approximately 4 K. Lower temperatures down to 1.2 K were achieved by pumping the liquid Helium with a Roots pump, taking it to the superfluidic phase. The sample was located at the bottom of the cryostat with the help of a long probe which had a sample holder at the tip and several feedthroughs connecting the sample to BNC sockets outside of the cryostat. The bottom of the cryostat was in its turn located at the center of the superconductive solenoid. It was possible to mount the sample such that the applied magnetic field would be aligned with any of the axes of the coordinate system of Figure 3-6.

However, aligning the sample in plane with the magnetic field was not easy and could only be done in a coarse way. After the sample being in place in the cryostat, the alignment was finely adjusted by displacing the sample from the center of the superconductive solenoid by carefully pulling the probe millimeters from the cryostat, while the Hall resistance R_{xy} was being monitored. Once the minimum of R_{xy} was found, the sample was considered as well aligned as possible. It will be understood later in this Thesis that even misalignments of angles of approximately half a degree can subject the sample to a tilted magnetic field such that its perpendicular component is large enough to supress the periodical magnetic field with zero average, whose presence is crucial to observe some of the results. In one experiment, it was estimated a perpendicular component of $\vec{B_a}$ of approximately 40 mT when $B_a = 3$ T but similar values were observed in other experiments. Microwaves were generated by a range of backward wave oscillators covering the 35-110 GHz band. A cylindrical waveguide carried the microwaves down to the sample space through the probe. The sample was irradiated perpendicularly regardless of the alignment of the sample with the magnetic field.

The normal procedure is to irradiate the sample with microwaves of fixed frequency and sweep the static magnetic field at a rate of 1 T/min. Under a static magnetic field, magnetic moments sense a torque that causes a precession around the magnetic field vector with a Larmor frequency dependent on the magnitude of the field. Ramping the field, the frequency of this precessing motion matches

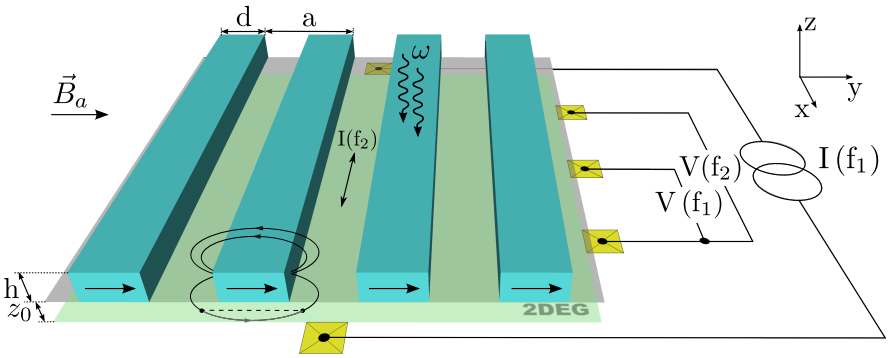

Figure 3-6: *Lateral superlattice consisting of an array of ferromagnetic stripes (Dy or Co) located 90 nm above a 2DEG. The grating is irradiated by microwaves at frequency ω while being magnetised in the plane by magnetic field B_a. At resonance, oscillations of the stray magnetic field induce a microwave current, $I(f2)$, in the 2DEG. The frequency f_2 is the frequency of the amplitude modulation of the microwaves. The photovoltage, $V(f_2)$ is measured at the frequency used to modulate the microwave power, $f_2 = 870$ Hz. The photoresistance is measured at frequency $f_1 = 13$ Hz*

eventually the frequency of the time dependent magnetic field, magnetic resonance occurs and a peak develops at the corresponding value of static magnetic field in the longitudinal magnetoresistance measured in the 2DEG.

The device operated with a current supply no higher than 1 μA. Rather sensitive equipment was required to detect the weak magnetoresistance signals, thus the voltage drop $V(f_1)$ was measured with a lock-in amplifier. The oscillator of the lock-in amplifier was connected in series with a resistor in a circuit to supply an *ac* current to the device. The phase-sensitive detector of the lock-in amplifier was set at the same frequency $f_1 = 13Hz$ as the oscillator. An alternative method was used to acquire a signal more dependent of the microwaves. The method consists of setting an amplitude modulation on the microwave output with frequency $f_2 = 870$ Hz which induces eddy currents $I(f_2)$ in the 2DEG - see Figure 3-6. An additional lock-in amplifier is used to lock on this frequency f_2 and measure the photovoltage $V(f_2)$. It was observed that the signal of microwave induced effects had bigger amplitude by using this method.

It is traditional to apply the current and measure the voltage drops in differ-

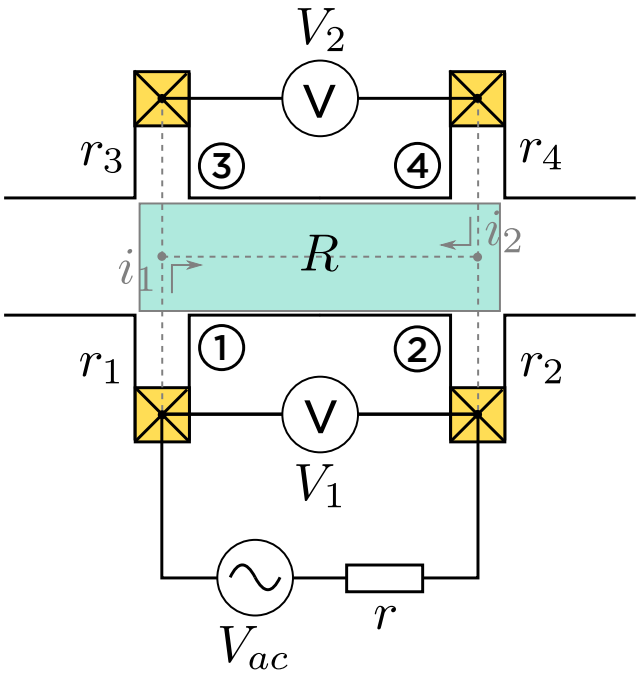

Figure 3-7: *Circuit of a 4-terminal measurement.*

ent voltage probes, a method called 4-terminal measurement. This method is preferred to its counterpart 2-terminal measurement because it determines the resistance more accurately by neglecting the internal resistance of the wiring and ohmic contacts of the current source. In Figure 3-7, the oscillator V_{ac} and the resistance r are equivalent to a current source. It is intended to determine the resistance R of the device, thus the circuit is closed by connecting the device to the current source using terminals 1 and 2. However, the output current i_1 of the current source is large enough so that the internal resistance of the wiring and ohmic contacts must be considered. If the voltage is measured using the same two terminals as the current source, the voltage drop V_1 would not be only across the active region of the device but instead across the active region plus the internal resistance of the wiring and ohmic contacts, $V_1 = (R + r_1 + r_2)$. Since r_1 and r_2 are unknown, neglecting these would lead to a inaccurate value of R for what is supposed to be a precise measurement. Instead, if the voltage drop is detected in other 2 terminals, another circuit loop will be created but the current i_2 of this sensing circuit will be very low, therefore the internal resistances r_3 and r_4 are negligible in comparison with R. Since $i_1 \gg i_2$, it is assumed the current flowing in R is $\approx i_1$. This new voltage drop is given by $V_2 = Ri_1$.

Chapter 4

Electrical detection of dipolar spin waves in lateral magnetic superlattices

In this chapter, the results of collective excitations of spins in the magnetic grating resistively detected in a 2DEG, which acts as a sensor, are reported. Two types of excitations were studied: localised spin wave modes - designated dipolar edge spin waves (DESW) - which become confined in spin wave wells near the lateral edges of the stripe, and dipolar magnetisation waves (DMW) which propagate across the 1D array through the magnetostatic interaction between the stripes. The localised modes of spin waves confined in spin wave wells will be also briefly characterised.

4.1 Spin wave wells in transversely magnetised magnetic stripes

While Kittel's model of shape anisotropy (Section 2.6) is a good enough approximation at strong magnetic fields to describe simple ferromagnetic resonance by assuming the internal field is uniform all over an ellipsoidal sample, a more ac-

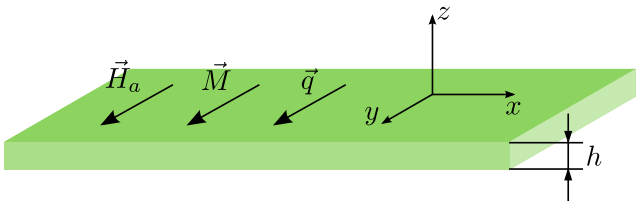

Figure 4-1: *Orientation of the applied magnetic field and magnetisation vectors and the direction of propagation of the microwaves with respect to the sample geometry. The origin of the coordinate system is considered to be located at the middle of the infinite stripe.*

curate description of the involved processes is needed in order to generalise the theory for the application in magnetic stripes subject to dipolar interaction from neighbouring stripes.

Spin wave propagation is going to be characterised in a sample shaped as an infinitely long rectangular prism [1] — which is an approximation of the samples studied in this Thesis — with a width of 2 μm which is magnetised with a magnetic field where the vector is oriented in the stripe plane and along the width. Furthermore, the sample is subjected to a radiofrequency magnetic field with a wavevector parallel to the magnetic field. The system is illustrated in Figure 4-1.

The field inside the sample is strongly inhomogeneous, especially near the edges where the poles are formed, due to the strong demagnetisation. Spin wave propagation is affected by the internal field H_i in such way that, in regions where the field gradient is steeper, spin waves propagating along the width become confined.

Figure 4-2 shows the internal field profile as a function of y. It has a broad maximum at the centre of the sample and decreases to zero as y approaches $\pm 1\mu$m, where the edges are located. At the centre, where the internal field is maximum, the magnetisation is aligned with the field and is saturated. Close to the edges where the internal field is almost zero, the magnetisation is no longer saturated and thus magnetic domains are formed. The strong inhomogeneity affects the propagation of spin waves considerably by creating a "well" which confines spin waves [20, 2, 21]. Depending on the region of the inhomogeneous field being sensed, the spin wave modes acquire different properties. One can characterise the different types through an experiment of Brillouin light scattering

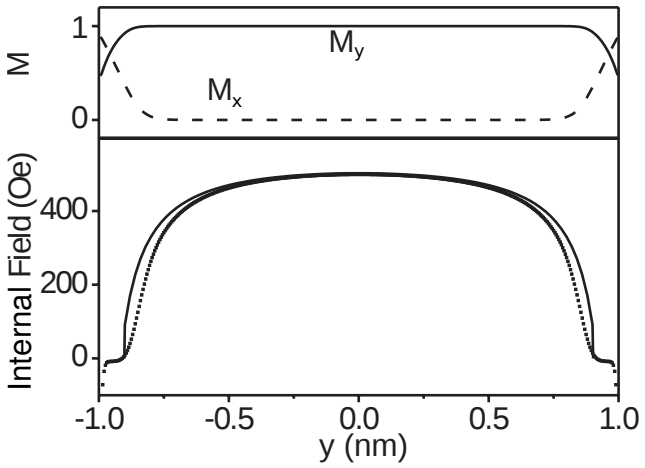

Figure 4-2: *(top) Magnetisation components M_x and M_y along the width of the stripe. (bottom) Internal field along the width of the stripe. Figure from Bayer et al [1].*

(BLS) [22].

The BLS spectrum (Figure 4-3) of a system with the configuration mentioned above is dominated by three features. At higher frequency, there is a structure with two peaks corresponding to two perpendicular surface spin wave (PSSW) [23] modes. One is located in the central region of the sample where the magnetisation and the internal field is close to maximum, and another is approximately at $y = \pm 0.5\mu$m. Decreasing in frequency, one can observe a broad structure at approximately 6 GHz corresponding to a band of resonances of nonlocalised spin wave modes. Finally at the lower frequency, there is a peak corresponding to the resonance of a localised mode, confined in the spin-wave well. In Figure 4-3, the major difference between an applied field of 500 and 800 Oe is the existance of a second localised spin wave mode at a higher frequency than the first mode but still lower than the band of nonlocalised modes.

Figure 4-4 shows the applied field dependence of the frequency of the several types of spin wave modes. As the applied field is increased, the number of localised modes is increased as well. These modes are shifted to higher frequency. Below a threshold value H^* of applied field, where the field is not sufficient to saturate the magnetisation at the centre of the sample, there is only one PSSW mode in the region $H_i = H_i(y)$. At H^*, the PSSW peak splits with the creation of the mode located where the magnetisation is saturated at higher frequency. The peak at

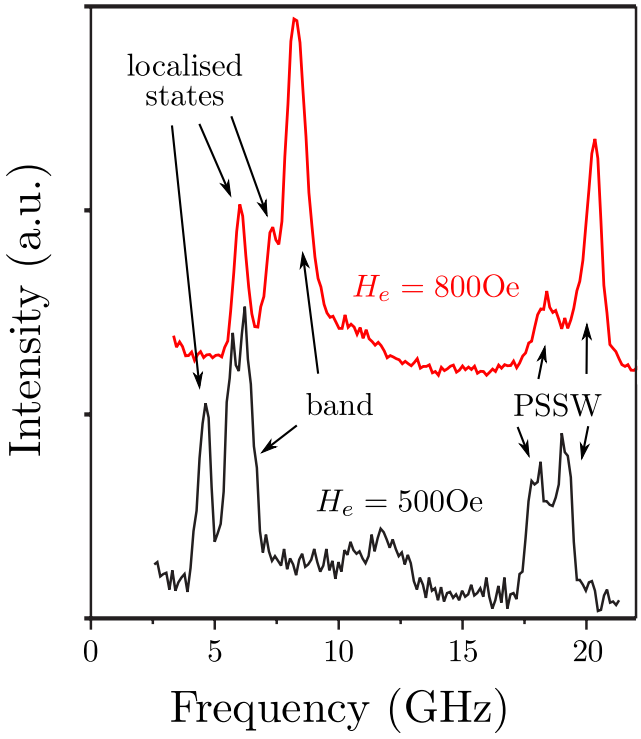

Figure 4-3: *BLS spectra of a magnetic stripe magnetised transversely, showing the localised spin wave modes, the band of spin wave modes propagating freely along the width of the stripe and the PSSW modes for two values of applied field, 500 and 800 Oe (black and red). Data from Bayer et al [1].*

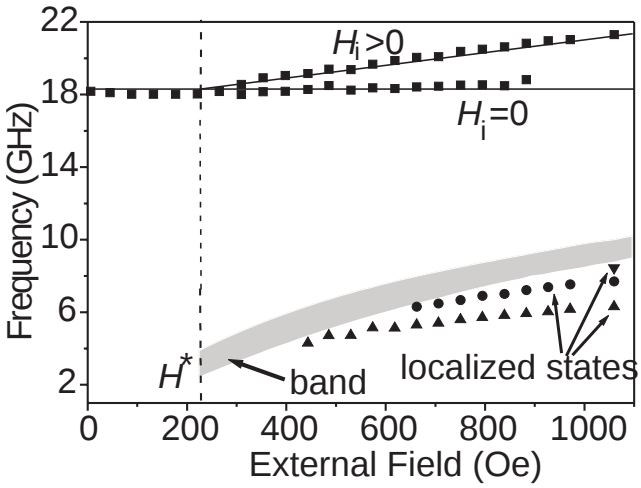

Figure 4-4: *Applied magnetic field dependence of the frequency of the spin wave modes. Figure from Bayer et al [2].*

lower field retains its frequency whereas the frequency of the other PSSW mode increases with increasing applied field.

Consider a spin wave travelling from the edge to the centre of the sample with frequency ω_0 and traversing the region where $H_i = H_i(y)$. Since the dispersion relation depends of the wavevector and the internal field, $\omega[q(z), H_i(y)]$, the variation of H_i must be compensated by varying the wavevector q accordingly to maintain the frequency ω_0 constant. However, if the conditions are met, the field H_i can be so large that no real solution of q satisfies the dispersion relation. The spin wave becomes evanescent when the dispersion relation can be only fulfilled with a imaginary wavevector. Spin waves are reflected at the point $y = y_l$, called the left turning point, where the wavevector q becomes imaginary. This explains the localisation of certain spin wave modes and the formation of a spin wave well. For large enough frequencies, there might be a real solution of q for any given y which means the spin wave propagates throughout the whole sample width without any confinement.

In order to determine the frequencies of the localised spin-wave modes, one must start by calculating the internal field. The internal field is defined by $\vec{H}_i = \vec{H}_a + \vec{H}_h + \vec{H}_d$, where $\vec{H}_a$ is the applied field, $\vec{H}_h$ is the uniaxial anisotropy field (Section 2.4) and $\vec{H}_d$ is the demagnetising field. The demagnetising field H_d can be determined from Maxwell's equations using the same method as in [24]. The magnetisation was considered uniform along the z axis, thus calculating H_d at $z = 0$.

The dispersion relation for spin waves propagating in the medium described above corresponds to the dispersion of the dipolar-exchange spin waves characterised by Kalinikos *et al* [25], and is given by

$$\left(\frac{\omega}{\omega_M}\right) = \left[\frac{\omega_H}{\omega_M} + \alpha q^2\right]\left[\frac{\omega_H}{\omega_M} + \alpha q^2 + \frac{1 - \exp(-qh)}{qh}\right] \tag{4.1}$$

where $\omega_M = \gamma\mu_0 M$, $\omega_H = \gamma\mu_0 H_i$ and $\alpha = 2\pi A/\mu_0 M_s^2$ is the exchange constant expressed as a function of A, the exchange stiffness constant. The wavevector $\vec{q} = q_x\hat{x} + q_y\hat{y} + q_z\hat{z}$ is quantised in two directions. The component $q_z = p\pi/h, p = 1, 2, 3...$ is quantised by the finite thickness of the specimen. The component q_y

is quantised by the spin-wave well and the deeper the spin wave well is, more discrete modes exist. The Equation 4.1 admits real solutions of q if the Larmor frequency of the internal field is smaller than the microwave frequency, $\omega_H < \omega$, demonstrating that the localised spin-wave modes become trapped in the regions of lower internal field, close to the edges of the sample. The discrete values of q_y are determined by the following expression 4.2, using Wentzel-Kramers-Brillouin quantisation [20]

$$\int_{y_l}^{y_r} q_y[H_d(y), \omega]dy = m\pi \tag{4.2}$$

where m is the mode index and y_r is the right turning point which is the location where the Larmor frequency becomes zero, $\omega_H(y_r) = 0$.

4.2 Results

Using the double modulation technique described in Chapter 3, photovoltage and photoresistance were measured in the 2DEG of samples A-D to study the high frequency dynamics of spins in dysprosium and cobalt gratings. This was possible because of the coupling between the excitations in the magnets and the 2DEG through their dipolar field. Two types of spin waves could be resolved in the measurements: dipolar magnetisation waves which propagate across the grating and, inside the stripes, localised modes of spin waves, which will be designated by dipolar edge spin waves, become confined in a well created in the inhomogeneous internal field. The usefulness of the 2DEG as a sensor to detect excitations in small magnets will be confirmed by probing for the uniform modes of oscillation (conventional ferromagnetic resonance) in a single stripe sample.

4.2.1 Ferromagnetic resonance of individual wires

Under microwave irradiation, the magnetoresistance in sample A exhibits a single sharp resonance that moves to higher magnetic field with increasing microwave frequency - see Figure 4-5. The position of the resonant dip depends linearly on

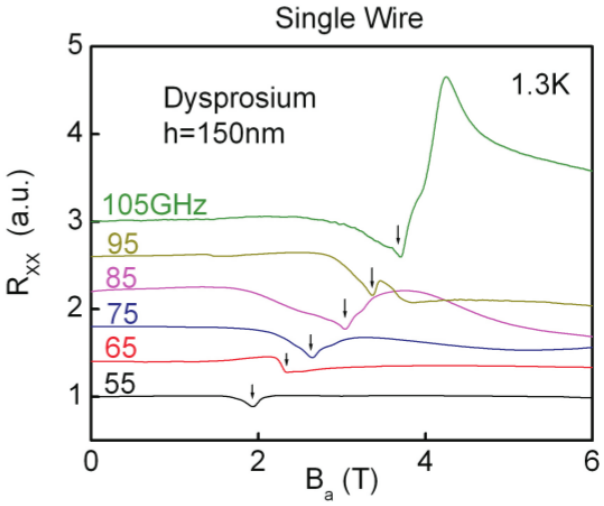

Figure 4-5: *Ferromagnetic resonance of sample A detected through a change in the resistance of the 2DEG ($B_a||y$) as a function of the applied magnetic field. Curves are vertically offset for clarity. Arrows indicate resonance field for each frequency.*

the microwave frequency - see Figure 4-6. Shape anisotropy is covered in Section 2.6. The resonance condition is dependent on the sample geometry and is given by the Kittel [11] formula:

$$\omega = \gamma\mu_0 \{[H_a^* + (N_x - N_y)M_s]\times \times[H_a^* + (N_z - N_y)M_s]\}^{\frac{1}{2}} \tag{4.3}$$

where γ is the gyromagnetic ratio. $N_x = 0$, $N_y = 0.45$, $N_z = 0.55$ are the demagnetisation factors of the stripe derived in Appendix A. It is found that Equation 4.3 must include the crystal field anisotropy of Dy to fit the data, which would return lower resonance fields than the experimental results otherwise. Magnetocrystalline anisotropy behaves as an internal magnetic field $\bar{H}_h$ that adds to H_a [11]. It is therefore defined the effective applied magnetic field as $H_a^* = H_a + \bar{H}_h$. The best fit is obtained for $\mu_0\bar{H}_h = 0.6$ T - see Figure 4-6 (full line). One obtains the Landé g-factors $|g| = 1.81$ (Co) and $|g| = 1.95$ (Dy), which are similar to the tabulated values -1.83 [26] and ~ 2, respectively. Broad peaks are known to characterise the ferromagnetic resonance of dysprosium crystals [27, 28].

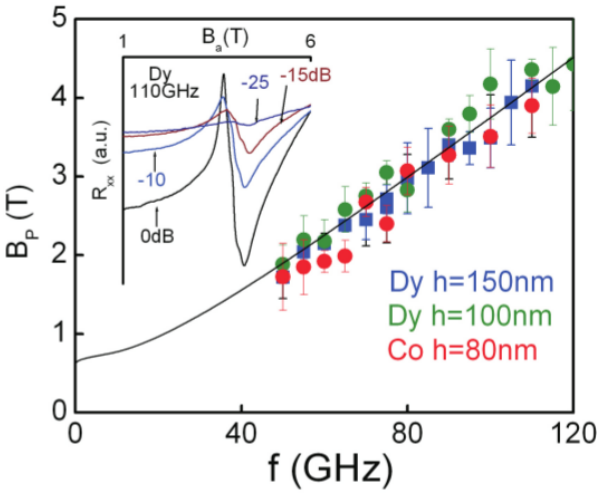

Figure 4-6: *Frequency dependence of the resonant field (symbols) fitted with Equation 4.3 (full line). Inset: Microwave power dependence of the magnetoresistance in the vicinity of the resonant field.*

To demonstrate that the resonance is microwave induced its power dependence is studied, as it can be seen in the inset to Figure 4-6. It is demonstrated that the resonance occurs in the ferromagnet - rather than in the 2DEG - by studying its temperature dependence in Figure 4-7. The peak amplitude decreases from 20K to 75K and completely vanishes at 100K. Since dysprosium is ferromagnetic up to 85K, this explains the photoresistance resonance in this temperature range. Above 85K, the magnetic moments adopt a spiral structure which produces zero net magnetisation [29]. Ferromagnetic resonance then becomes impossible which is why the resonant structure vanishes from the 100K photoresistance curve. It was therefore demonstrated that the 2DEG is sensitive to the dynamics of small magnetic elements at its surface. In the case of individual stripes, the FMR occurs at a single frequency.

4.2.2 Dipolar magnetisation waves and dipolar surface spin waves in 1D arrays of magnetic wires

Magnetic gratings exhibit more complex magnetic excitations than single stripes. This can be seen in Figure 4-8 which studies the photovoltage of sample B at

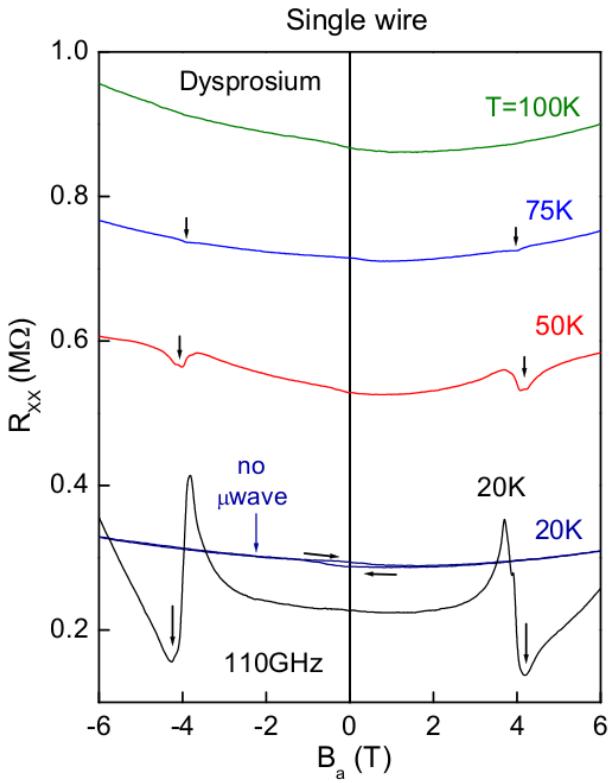

Figure 4-7: *Temperature dependence of the photoresistance of sample A. The FMR vanishes above the Curie point of dysprosium (85 K). The magnetic hysteresis of dysprosium is visible in the curves measured without microwaves. Other curves are measured by sweeping the magnetic field up.*

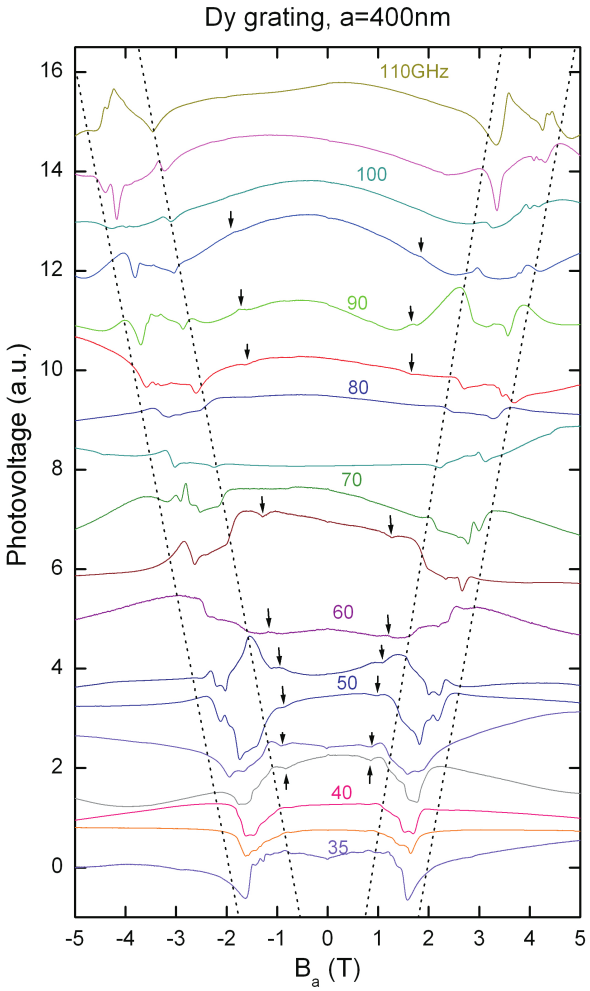

Figure 4-8: *Photovoltage spectroscopy of magnetic excitations in sample B ($B_a||y$), taken at a temperature of 1.5K. The dotted lines are a guide to the eye for the magnetic field dependence of the onset and the cutoff of the FMR range. At lower magnetic field, the arrows indicate a series of smaller dips induced by microwaves. Curves are vertically offset for clarity.*

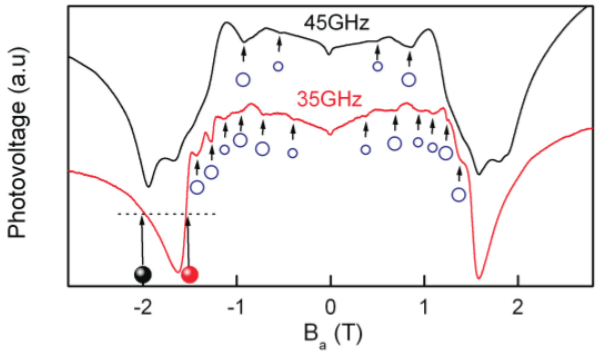

Figure 4-9: *Details of the fine resonant structure at 35 GHz and 45 GHz. The diameter of the blue circles is proportional to the amplitude of the dips. The onset (red dot) and the end (black dot) of the FMR range are defined at the mid-height of the main resonance.*

microwave frequencies varying between 35GHz and 110GHz. A series of complex resonances loosely delimited by the dashed lines replaces the single resonance of individual stripes. To allow for a more precise comparison with theory, it is plotted the onset and the end of the FMR range as the red and black circles in Figure 4-10. The onset and the end of the magnetic field range are taken at the half height of the FMR range - see in Figure 4-9.

The FMR bandwidth increases with microwave frequency. It starts from 0.4 T at 35 GHz and increases to 1.8 T at 110 GHz, as it can be seen in Figure 4-10. Below 60 GHz, the onset oscillates from the trend line to a higher magnetic field value before eventually settling for the higher magnetic field boundary at 42 GHz. In comparison, the oscillations of the cut-off are weaker and remain centered on the trend line. It is believed that below 60 GHz, the magnetic field at the onset minus the demagnetising field becomes smaller than the field needed to saturate the magnetisation ~ 1 T. Therefore it is suggested that below 42 GHz, the FMR only survives at the higher end of the resonance range where the magnetisation is more likely to be saturated.

Microwaves also induce a series of discrete resonances at lower magnetic field. These are indicated by the arrows in Figure 4-8 and by the open circles in Figure 4-10. The resonances shift linearly with frequency but at a weaker rate than the FMR. The narrowness of the dips and their occurrence below the FMR is

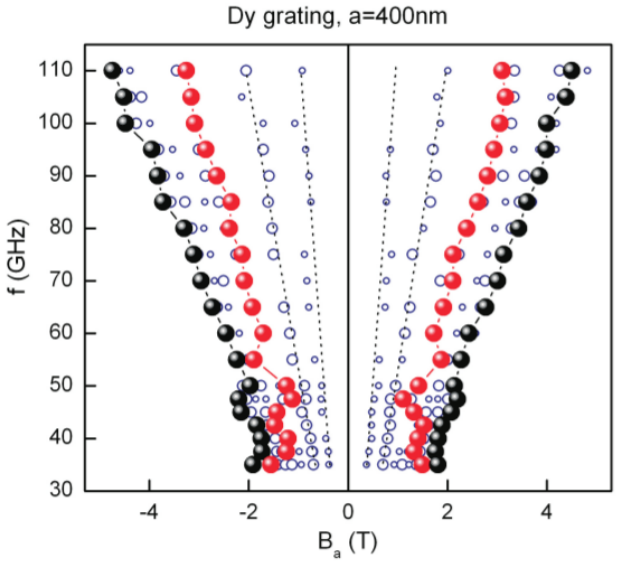

Figure 4-10: *Frequency dependence of the microwave resonances in the photovoltage of sample B, taken at a temperature of 1.5 K. The fan diagram shows the FMR onset (red dots), the FMR cutoff (black dots) and the dependence of the small photovoltage dips at low field (blue circles).*

suggestive of localised spin waves. There are two localised modes in sample *B*.

Regarding to sample *C*, the photovoltage curves of Figure 4-11 show a broadening of the FMR band, as in sample *B*. The FMR band hosts a complex series of subsidiary resonances. The frequency dependence of the onset and the end of the FMR is plotted in Figure 4-12. The width of the FMR increases from 0.9 T at 35 GHz to 1.4T at 80 GHz thus qualitatively reproducing the trend of sample *B*. Unlike sample *B* however, the width of the FMR is more stable, less dependent on microwave frequency, below 60 GHz. This is one indication that dipolar interactions are more effective in stabilising the magnetisation in the direction perpendicular to the stripes. This observation is corroborated by the fact that sample *C* has smaller demagnetising field in comparison to sample *B* due to having half the thickness. Consequently, the internal field is stronger and thus magnetisation saturation is achieved at a lower applied magnetic field. This allows FMR to be observed at lower microwave frequencies than in sample *B*.

Sample *C* exhibits a series of microwave induced dips below the FMR. The dips are indicated by the arrows in Figure 4-11 and by the open circles in Figure 4-

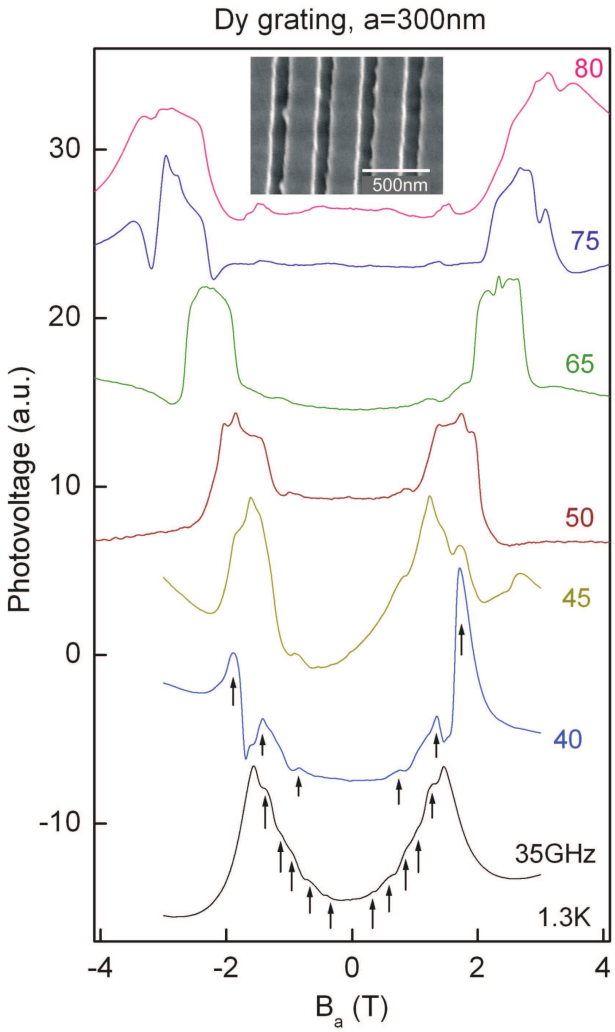

Figure 4-11: *Photovoltage spectroscopy of magnetic excitations in sample C ($B_a||y$). The broad FMR peak corresponds to the excitation of DMWs across the grating. The series of dips highlighted by the arrows indicates resonances with quantised DESW modes in individual stripes. Curves are vertically offset for clarity. Inset: dysprosium grating of sample C (detail).*

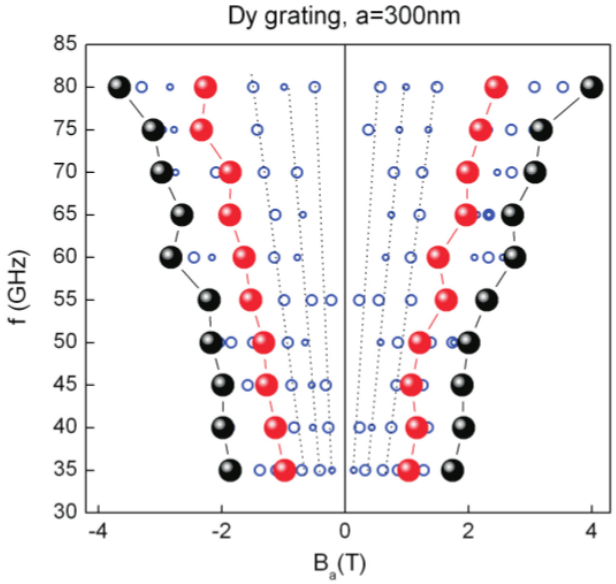

Figure 4-12: *Frequency dependence of the microwave resonances in the photovoltage of sample C, taken at a temperature of 1.5 K. The fan diagram shows the FMR onset (red dots), the FMR cutoff (black dots) and the frequency dependence of the small photovoltage dips at low field (blue circles).*

12. Their frequency dependence is similar to that of the low field resonances in sample B. However, there are 3 resonances in C compared to 2 in B. The first resonance occurs earlier, at $B_a = 0.23$ T (C) compared to $B_a = 0.39$ T (B) at 35 GHz. The observation that DESW modes have larger gaps in sample B than in C shows that spin waves are more tightly confined — *i.e.* are confined in a narrower quantum well — in sample B than in C. Lateral confinement by the physical edges can be ruled out as an explanation, firstly because h is twice as large in sample B. The quantisation of wavevector $q_z = p\pi/h$ gives the largest gaps in sample C - the opposite of what is observed. Secondly, the nearly identical values of d in B and C also rules out the quantisation of q_y . The resonant dips must therefore arise from (magnetic) confinement in the y direction. The tighter spin wave confinement in B is consistent with earlier reports of a stronger dipolar magnetic field in B.

Figure 4-13 maps the FMR signal of sample D. The FMR band is 0.75 T wide at 80 GHz - see Figure 4-14. This is smaller than in samples B (1.0 T) or C (1.4 T) at the same frequency. In Appendix C, it is calculated the dipolar magnetic

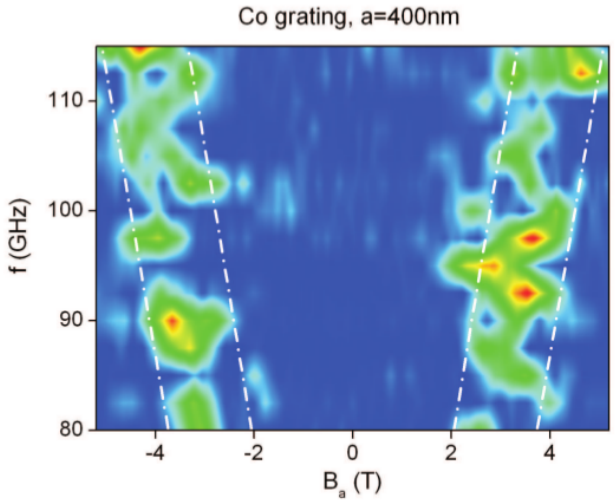

Figure 4-13: *Photoresistance of sample D mapped as a function of microwave frequency and magnetic field ($B_a||y$). The bandwidth of the resonance with DMWs is delimited by the dash-dotted lines.*

field in the grating and it is shown that it is proportional to the magnetisation. Since the magnetisation of Co is half that of Dy, the data demonstrates that the width of the FMR increases with the strength of the dipolar magnetic field.

It was found that the photoresistance is highly anisotropic when the magnetic field is rotated in the plane - see Figure 4-15. When the stripes are magnetised along their long axis, the 2DEG effectively decouples from the grating. The magnetoresistance remains featureless even at the highest microwave power and

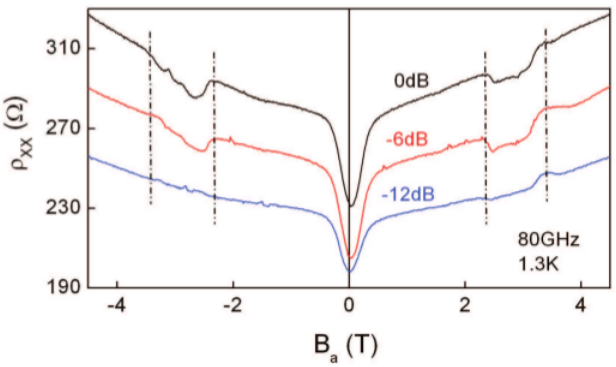

Figure 4-14: *Microwave power dependence of sample D. The bandwidth of the resonance with DMWs is delimited by the dash-dotted lines.*

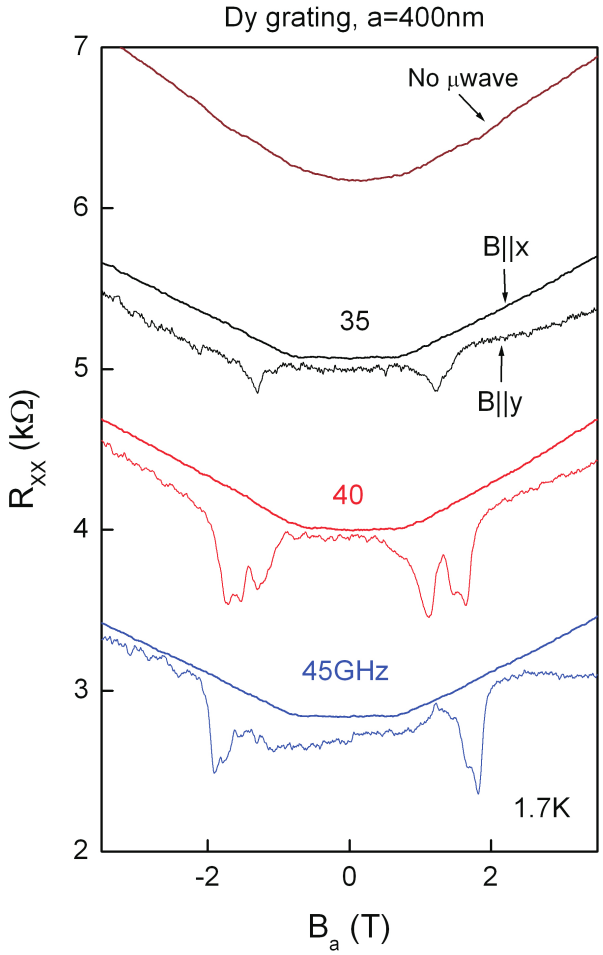

Figure 4-15: *Comparison of the photoresistance obtained in a transverse magnetic field ($B_a||y$) and a longitudinal magnetic field ($B_a||x$) for sample B. When $B_a||x$, the dipolar magnetic field is zero. Resonant absorption is recovered by aligning $B_a||y$.*

almost no change is observed when microwaves are switched off. An examination of the more sensitive photovoltage curves reveals a residual FMR signal and no resonant dips at lower field.

Magnetising the stripes along x eliminates the magnetic poles. This has three consequences: the stripes decouple from each other, the grating decouples from the 2DEG and the confinement of surface spin waves vanishes. The latter explains the absence of resonant dips in the photovoltage curves. Under resonant conditions with $B_a \| x$, the oscillations of magnetisation components M_y and M_z induce stray magnetic fields at the site of the 2DEG. The small amplitude of the

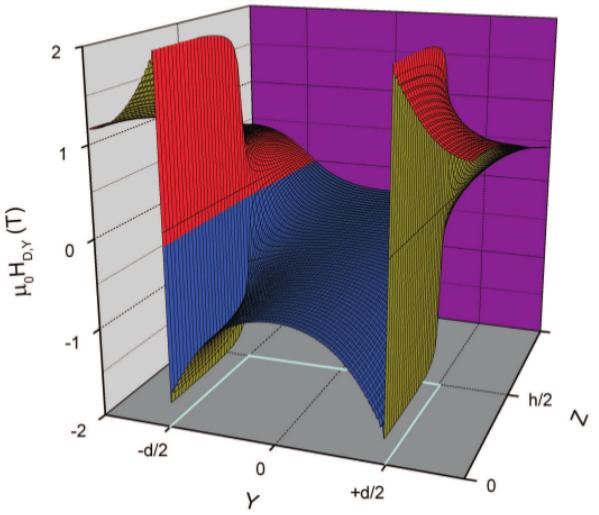

Figure 4-16: *Spatial variation of the in-plane dipolar magnetic field in one stripe of sample C. The superlattice is assumed to be magnetised to saturation along y. The edges of the stripe are indicated by the full lines in the y0z plane.*

photovoltage peaks and the absence of any effect in the photoresistance suggests that the ferromagnetic resonance cone is very narrow, M_y, $M_z \ll M_s$.

A theory that incorporates the above ideas is now developed and used to fit the experiments. It is started by calculating the magnetic field emanating from an infinite array of rectangular stripes whose stripes are assumed to be uniformly magnetised along y. Maxwell's equations are then solved using Fourier analysis done in Appendix C. The $H_{d,y}$ and $H_{d,z}$ vector components are obtained in the analytical form of Equations C.4 and C.6. Their spatial variation is computed in the case of superlattice C and plotted in Figures 4-16 and 4-17. Between $-d/2$ and $+d/2$, $H_{d,y}$ is the demagnetising magnetic field of the stripe. This field is strongly inhomogeneous decreasing from -0.4T at the centre to -1.4T near the poles. By contrast, $H_{d,y}$ varies smoothly in the z direction away from the $z = 0$ plane. Note that the magnetic well at $\pm d/2$ extends vertically right up to the physical edge of the stripe at $z = h/2$, making magnetic confinement undistinguishable from physical confinement in this direction. In Figure 4-17, $H_{d,z}$ diverges at the corners of the stripe. This is where the magnetic flux flips by 180 degrees. $H_{d,z}$ decays exponentially away from the stripes, giving a sinusoidal modulation of amplitude 0.24T as it passes through the plane of the 2DEG.

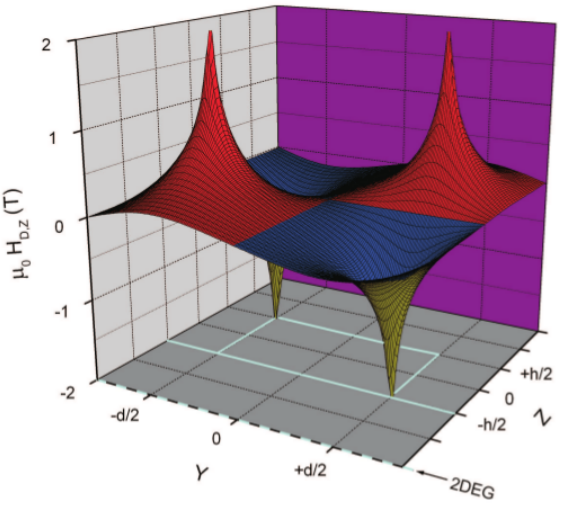

Figure 4-17: *Spatial variation of the perpendicular dipolar magnetic field in one stripe of sample C. The magnetic field that couples the grating to the 2DEG is the sine wave at the plane* $Z = -h/2 - z_0$.

Prior to modelling dipolar spin waves in confined geometries, it is necessary to recall the properties of bulk spin waves in ferromagnetic dysprosium. When H_a is along the magnetic easy axis - a-axis - the energy dispersion relation is given by [30]:

$$\begin{aligned} \hbar\omega(\vec{q}) \;=\; & \big\{[2S[J(0) - J(\vec{q})] + 3K_2S^{-1} + \hbar\gamma\mu_0 H_a] \\ & [2S[J(0) - J(\vec{q})] + 36K_6^6 S^{-1} + \hbar\gamma\mu_0 H_a]\big\}^{\frac{1}{2}}, \end{aligned} \tag{4.4}$$

where S=15/2 is the angular momentum on each Dy ion, $J(\vec{q})$ is the Fourier transform of the exchange interaction. The exchange energy of dysprosium is $\Delta E_{Ex} = 7meV$ [29]. $K_2 = 87 \times 10^6 \mathrm{J.m^{-3}}$ and $K_6^6 = -1.1 \times 10^6 \mathrm{J.m^{-3}}$ are the axial and hexagonal energies of magnetocrystalline anisotropy [31] which measure the energy cost of aligning the magnetisation along the c- and b- hard magnetic axes. The anisotropy terms in Equation 4.4 behave as two effective magnetic fields: $\mu_0 H_c = 3K_2/(SM_s)$ (12T) and $\mu_0 H_h = 36K_6^6/(SM_s)$ (1.8T) which add to H_a [11]. Given the large value of the H_c field, magnetocrystalline anisotropy reduces to the effects of H_h: the FMR lines are shifted to lower magnetic field by

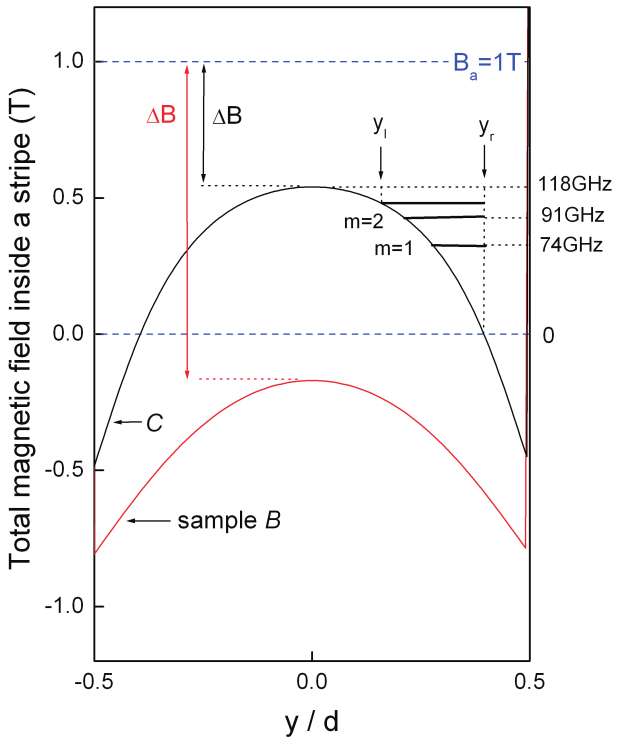

Figure 4-18: *Internal magnetic field across one stripe at height $z = 0$. The magnetic bias is $B_a + \bar{B}_h = 1$ T. ΔB is the bias threshold where the internal magnetic field becomes positive at the centre of the stripes and starts squeezing spin waves against the edges. The quantised dipolar edge spin wave modes $m = 1, 2$ and 3 ($p = 1$) are shown together with their frequencies. y_l and y_r are the left and right turning points of the $m = 3$ dipolar edge spin wave mode.*

$-H_h$ and there is a finite resonance frequency at zero magnetic field. Since the Dy stripes are polycrystalline [32], the magnetic field assumes random orientations with respect to the a-axis. The effective anisotropy of the polycrystal is estimated by averaging the $\sin^2\theta$ dependence of the magnetocrystalline energy over a solid angle of 4π steradians. It is obtained as $\bar{H}_h$ =$\mathrm{H}_h/3$, which matches the offset magnetic field (0.6 T) observed in our dysprosium devices.

Dipolar edge spin waves

The frequencies of spin waves quantised by magnetic wells at $\pm d/2$ in Figure 4-16 are now calculated. The calculation follows the method of Bayer et al. [1],

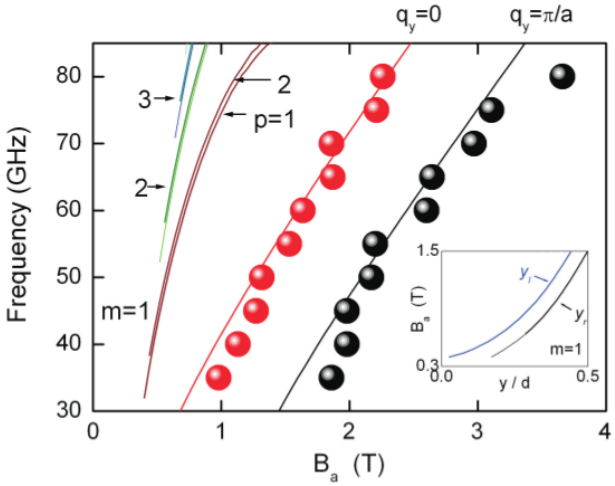

Figure 4-19: *Theoretical frequency dependence of the DESW modes ($m = 1, 2, 3...$ $p = 1, 2$) in sample C labelled $m = 1, 2$. Red and black spheres indicate the experimental values of the onset and the cutoff, respectively, of the DMW resonant range, whereas the red and black lines are the calculated values returned by Equation 4.9.*

mentioned in Section 4.1.

The calculation proceeds by finding the wavevector q_m where the dispersion curve, Equation 4.1, goes through its minimum. Wavevector q_m depends only on the microwave frequency. By inserting q_m into Equation 4.1 it was found the internal magnetic field at the left turning point. The spatial variation of the dipolar magnetic field being known, it is obtained y_l by solving Equation C.4 numerically. The right turning point is obtained in a similar way by solving $\omega_H(y_r) = 0$. Once y_l and y_r are known, the frequencies of the quantised DESWs $m = 1, 2, 3...$ are calculated using Equation 4.2. These modes are shown in Figure 4-18. Their magnetic field dependence is plotted in Figures 4-20 and 4-19.

The theoretical magnetic field dependence of the DESW frequencies in Figure 4-20 and 4-19 is now commented. The theory agrees with the experiment on the following points. Firstly, the DESW fan structure starts from a higher magnetic field in sample B than in sample C. This is because the demagnetising field is stronger inside stripe B - see Figure 4-18. As a result, the magnetic field ΔB needed to create a spin wave well is larger in B than in C. Secondly, the theory obtains the correct number of trapped modes using $A = 1.5 \times 10^{-12}$J.m^{-1} as the spin exchange stiffness constant of dysprosium [29]. The exchange constant

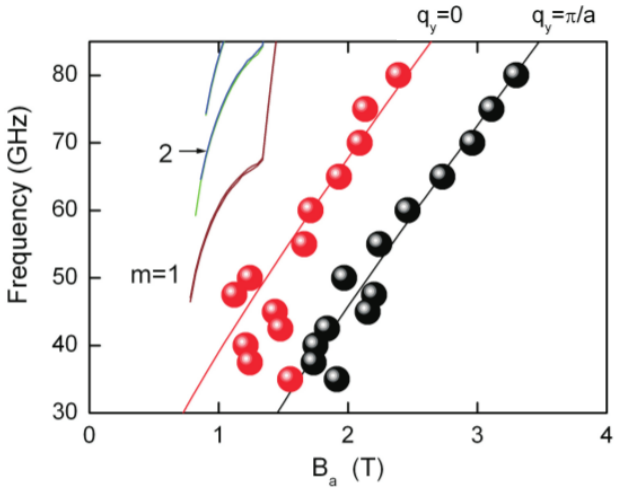

Figure 4-20: *Theoretical frequency dependence of the DESW modes ($m = 1, 2, 3...$ $p = 1, 2$) in sample B. The theoretical frequency dependence of the onset and cutoff magnetic fields of the DMW band is plotted as the red and black curves, whereas the experimental frequency dependence of the onset and cutoff of the DMW resonant range are represented by red and black spheres. Inset: left and right turning points of the m=1 DESW mode. The spin wave drifts towards the edge of the stripe as the magnetic field increases.*

calculated from $\alpha = 2\pi A/\mu_0 M_s^2$ gave $\alpha = 0.5\text{nm}^2$. Thirdly, the theory predicts one more branch in the theoretical fan of C than in the fan of B.

This is consistent with the observation of an additional branch in the experimental frequency dependence of the resonant range of sample C. This difference is explained by the deeper spin wave well of sample C - see Figure 4-18. Fourth, the theory correctly locates the DESW resonances below the FMR. Fifth, the frequency splitting of the $p = 1$ and $p = 2$ subbands induced by the vertical confinement is negligible compared to magnetic confinement along y. The nonlinearity of the theoretical branches however prevents making a quantitative fit. The bend in the $m = 1$ curve of Figure 4-20 occurs when the right turning point of the first DESW mode collides with the pole surface. At this point, the tighter confinement results in an upward shift of the $m = 1$ mode. The drift of DESW modes towards the pole surface is shown in the inset to Figure 4-19. Possible modifications that might enhance this picture are discussed later.

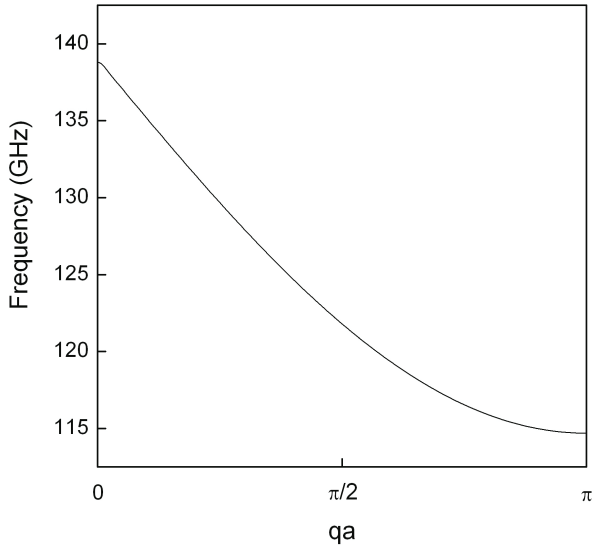

Figure 4-21: *Frequency dispersion curve of dipolar magnetisation waves in sample C at* $B_a = 5\ T$.

Dipolar magnetisation waves

An infinite array of rectangular magnetic stripes is now considered and the frequency dispersion curve of DMWs, $\omega(q_y)$, is calculated. The dephasing of the magnetisation from one stripe to the next makes the coupling between stripes dependent on wavevector q_y. As a result, the grating becomes a dispersive medium for the plane magnetisation waves that propagate through it. The DMW modes enter resonance over a finite range of frequencies which explains the FMR bandwidth. Since the FMR occurs in magnetic fields over 1 T, the magnetisation of Dy stripes will be considered to be saturated.

Consider one stripe labelled $n = 0$. Its magnetisation $M^{(0)}$ experiences a torque from B_a as well as from the spatially varying magnetic field emanating from all stripes. With the assumption of a homogeneous magnetisation, the overall torque applied to stripe $n = 0$ is the torque exerted by the stray magnetic field averaged over the stripe ($\bar{B}$). Under constant microwave irradiation, the magnetisation obeys a gyroscopic equation (Section 2.6) of the form:

$$\frac{d\vec{M}^{(0)}}{dt} = \gamma \vec{M}^{(0)} \times \vec{\vec{B}}(t), \tag{4.5}$$

where

$$\vec{B}(y,t) = \mu_0 \begin{cases} 0 \\ H_a + H_{d,y}(y,t) \\ H_{d,z}(y,t) \end{cases},$$

The dipolar magnetic field $\vec{H}_d$ is obtained from elementary magnetostatics [33, 24] as the sum of the dipolar field from each stripe. The magnetisation of stripe n $\vec{M}^{(n)}(t)$ generates a dipolar magnetic field $H^{(n)}_{d,y}(y,t) = -N^{(n)}_y(y)M^{(n)}_y(t)$ and $H^{(n)}_{d,z}(y,t) = -N^{(n)}_z(y)M^{(n)}_z(t)$ at the location of stripe $n = 0$. The coefficients $N^{(n)}$ are calculated at $z = 0$ by neglecting the variation of the internal magnetic field in the z-direction - see Figure 4-17 [1]. One obtains:

$$N^{(n)}_y(y) = \frac{1}{\pi}\left\{\arctan\frac{1}{\zeta^+_n} - \arctan\frac{1}{\zeta^-_n}\right\}, \tag{4.6}$$

$$N^{(n)}_z(y) = \frac{1}{\pi}\left\{\arctan\zeta^+_n - \arctan\zeta^-_n\right\}, \tag{4.7}$$

where $\zeta^{\pm}_n = (2y - 2na \pm d)/h$ and $N^{(n)}_x(y) = 0$. Equations 4.6 and 4.7 are inspired in Equation 33 of Ref. [1], which was, in its turn, derived from Joseph *et al* [24], and were generalised to return the demagnetisation factor of any stripe in the array. The coupling coefficients must be averaged to give the torque on stripe $n = 0$:

$$\bar{N}^{(n)}_\alpha = \frac{1}{d}\int_{-d/2}^{+d/2} dy N^{(n)}_\alpha(y) \qquad \alpha \equiv (y,z) \tag{4.8}$$

If $n = 0$, Equation 4.8 gives the demagnetisation coefficients of the semi-infinite prism. These satisfy the well-known sum rule $N_x + N_y + N_z = 1$. If $n > 0$, the N_α may be loosely viewed as generalised demagnetisation coefficients arising from the

coupling to other stripes. However, N_y is negative whereas N_z is positive because these coefficients obey a new sum rule: $N_x + N_y + N_z = 0$ $(n > 0)$, which is a consequence of summing Equations 4.6 and 4.7. One calculates H_d by summing the contribution from all stripes. The result is inserted into Equations 4.5 and 5.24. Equation 4.5 is solved by seeking solutions of the form $M^{(n)}(t) = M^{(0)} e^{i(q_y n a - \omega t)}$. Using the symmetry property $\bar{N}_\alpha^{(n)} = \bar{N}_\alpha^{-n}$, one finds the dispersion curve of DMWs:

$$\omega^2 = (\gamma\mu_0)^2 \quad \{H_a + \sum_{n=0}^{\infty} c_n [\bar{N}_z^{(n)} - \bar{N}_y^{(n)}] \cos(q_y n a) M_s\} \times \{H_a - \sum_{n=0}^{\infty} c_n \bar{N}_y^{(n)} \cos(q_y n a) M_s\}, \tag{4.9}$$

where $c_0 = 1$ and $c_n = 2$ for $n > 0$. Equation 4.9 generalises the Kittel formula of Equation 4.3 [11]. It makes clear that dispersive terms arise from the demagnetisation coefficients of higher order $n > 0$. The effects of long range dipolar coupling are particularly noticeable at long wavelengths where the frequency depends linearly on the wavevector - see Figure 4-21. The group velocity of DMWs is negative because the $N_y^{(n)}$ are negative. At long wavelengths, the in-plane dipolar field reinforces the applied magnetic field. As a result the Larmor frequency is maximum at $q_y = 0$.

Returning to the experimental data, the DMWs of wavevector $q_y = 0$ are the first to enter resonance since they require the lowest magnetic field to oscillate at frequency ω. The DMW modes at $q_y = 0$ $(q_y = \pi/a)$ are excited at the onset (cut-off) of the FMR range. The theoretical dependence of the FMR onset (red line) and the FMR cutoff (black line) is plotted in Figures 4-20 and 4-19. The use of the nominal parameters of samples B and C gives a FMR linewidth and position in very good agreement with the experiment (dots). This demonstrates the formation of DMWs in superlattices.

4.2.3 Discussion

The results demonstrate the coexistence of two types of spin waves in magnetic superlattices. Dipolar magnetisation waves are plane waves that travel across the superlattice. Dipolar edge spin waves, by contrast, are two dimensional waves quantised by spin wave quantum wells near pole surfaces. There is no experimental evidence suggesting the hybridisation of DESWs across the superlattice. Judging the strength of the dipolar interaction by the height of the resonances, the coupling between DESWs in different stripes must be at least 10 times smaller than the magnetostatic coupling between stripes. The experiment does not permit to ascertain whether DESWs trapped at opposite edges of the same stripe hybridise or not. Intra-stripe coupling is predicted to be negligible at the high magnetic fields that were used [1]. This seems to be confirmed by the absence of dedoubling of the dips at higher m-values. The frequency dependence of these dips with the magnetic field is stronger than the theory predicts [2]. This discrepancy comes from the assumption of a uniform magnetisation which was made to calculate $\vec{H}_d$. This assumption has the effect of giving a strong demagnetisation field between y_r and $+d/2$ which tends to create a magnetic domain. As a result, the magnetisation and dipolar field must be computed self-consistently with the result that both the magnetisation and the dipolar field decay smoothly to zero at $+d/2$. This correction to the model would make $y_r \approx d/2$ and eliminate the bend in the $m = 1$ branch of Figure 4-19.

The dispersion curve of DMWs given by Equation 4.9 is similar in shape to the dispersion curve computed by Kostylev et al. [34] however the group velocities have opposite signs. This difference underlines the exchange dominated character of dipolar exchange spin waves at low magnetic field in contrast to the dipole dominated character at high field. The exchange force controls the part of the spin wave inside the stripes and is zero at $q_y = 0$. This gives a dispersion curve with positive group velocity. Dipolar interactions control the part of the spin waves between the stripes and are the only interactions left when the stripes are magnetised to saturation, which is a condition verified in the experiments when in the resonance range. The coupling strength of the dipolar interactions is maximum at $q_y = 0$ which is why DMWs have negative group velocity. For the sake of completeness, it is verified the assumption of the constancy of the internal

field along z which is made when calculating the demagnetisation coefficients $\bar{N}_\alpha^{(n)}$. Considering one stripe of sample B, the demagnetisation factors calculated from Equation 4.8 are $\bar{N}_y^{(0)} = 0.49$ and $\bar{N}_z^{(0)} = 0.51$. The exact demagnetisation factors calculated from Equations A.1 and A.2 in Appendix A are $N_y = 0.45$ and $N_z = 0.55$. The small differences in these numbers shows that Equation 4.9 remains a good approximation of the dispersion curve even for relatively thick stripes.

Chapter 5

Double spin resonance under coherent population trapping

This chapter reports on the results of the detection of electron spin antiresonance in the 2DEG of a GaAs/AlGaAs heterostructure modulated by a inhomogeneous magnetic field and irradiated by microwaves.

Inhomogeneous magnetic fields are a vast field of research and covering a bit of everything is out of the scope of the Section 5.1. It is relevant to understand the conditions that lead to the formation of snake states, its characterisation with respect to the dynamics and how the conduction in the 2DEG is affected in the framework of the semiclassical drift-diffusion model.

Electromagnetic susceptibility with anomalies due to the formation of a dark state in lambda-type atoms is presented within the scope of the coherent population trapping framework in Section 5.2. In the results section it will be suggested that the same mechanism is achieved with fields in the microwave range with conduction electrons in a 2DEG.

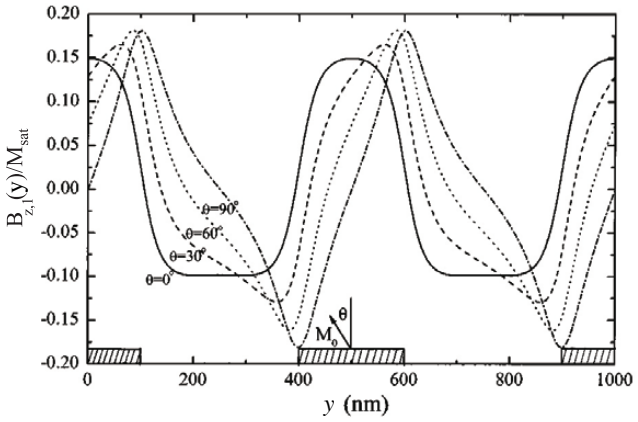

Figure 5-1: *Magnetisation angle dependence of the magnetic field profile emanating from a magnetic grating. If the z-axis is perpendicular to the plane of the grating, the x-axis is parallel to the length of the stripes and the y-axis is parallel to the width of the stripes, M_0 is the projection of the magnetisation vector in the plane $y0z$ and θ is the angle M_0 with respect to the z-axis. Thus, $\theta = 0°$ and $90°$ corresponds to $\vec{M}_0 \parallel z$ and $\vec{M}_0 \parallel y$. Figure from Nogaret [3]*

5.1 Ballistic electrons in a spatially periodic magnetic field

It is now considered the case where a 2DEG in the ballistic regime is subjected to an inhomogeneous magnetic field, more specifically the situation where a field perpendicular to the 2DEG varies periodically along the y axis, is constant in the x direction and its mean amplitude is zero [35, 36].

Such case can be achieved by depositing a one dimensional array of ferromagnetic wires at the surface of the heterostructure, aligned in parallel with the longer edge of the 2DEG. If the array is magnetised to saturation with a field in-plane with the 2DEG and across the wires, it generates a stray field which at the location of the 2DEG (90nm below) has a perpendicular component $B_{1,z}$ that meets the specifications mentioned above and a component parallel to the y axis, $B_{1,y}$, approximately constant. Under the magnetic field, ballistic electrons are deflected according to the local Lorentz force. Since the mean amplitude is zero, the 2DEG must be divided in regions of magnetic field of opposite sign, as it can be seen in Figure 5-2. At the boundary between such regions, the magnetic field is zero. The boundary will from now on be referred in the section as magnetic

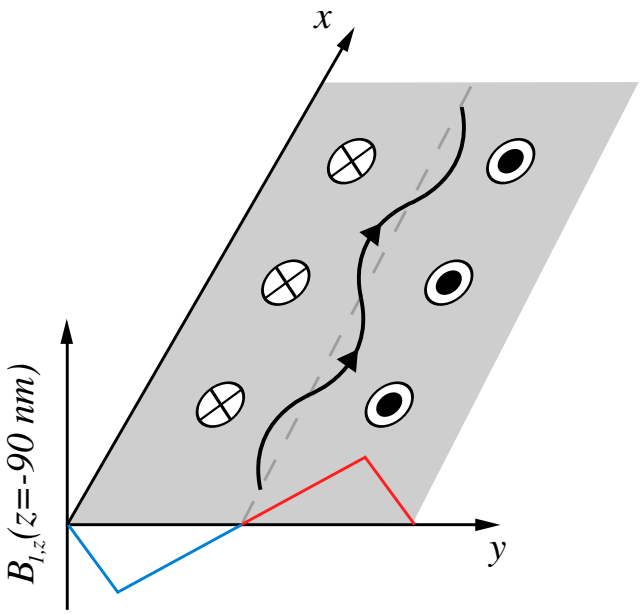

Figure 5-2: *Diagram illustrating two regions of the 2DEG subjected to a perpendicular magnetic field of opposite sign, the case corresponding to when the grating is magnetised along the y-axis. The profile of the magnetic modulation is similar to the profile of* $\theta = 90°$ *of Figure 5-1.*

edge.

The stray field generated by a periodic 1D array can be calculated accurately by the formula in the Appendix B. In Figure 5-1 is depicted the magnetisation angle dependence of the magnetic profile for a given array of stripes. It can be seen that when $\vec{M}\|z$, the magnetic profile is somewhat rectangular whereas it has a triangular shape when $\vec{M}\|y$. If the magnetisation vector is made to point to the x axis direction, the magnetic modulation is switched off. Figure 5-3 shows MFM images of an array of Cobalt wires. When the array is magnetised along the y axis, magnetic poles are formed in the facets parallel to the plane defined by the x and z axis, shown as black lines in the image. When in the $\vec{M}\|x$ case, no magnetic poles are formed and it can be said the magnetic modulation is switched off.

The 2DEG sees a magnetic potential when inhomogeneous magnetic fields of the aforementioned configuration are applied to it [35, 36]. Quantum phenomena affecting the behaviour of the electrons when drifting in such magnetic potentials are going to be quickly introduced. The magnetic field $B_{1,z}$ has a correspondent

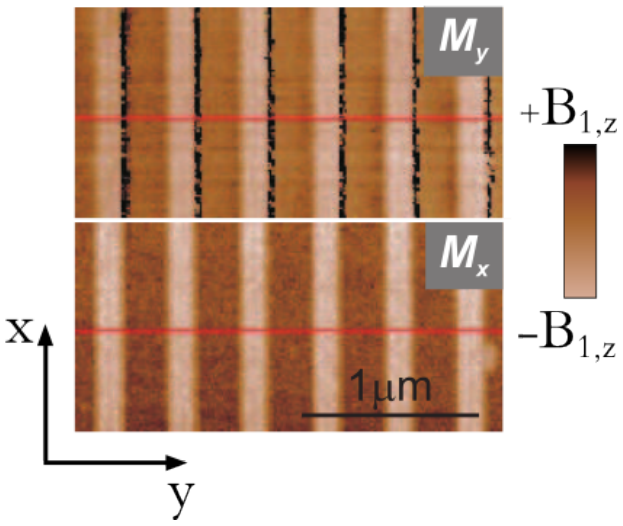

Figure 5-3: *MFM images of the Co grating magnetised along y (top) and along x (bottom). Magnetic pole formation is observed in the first case, but not in the second.*

vector potential defined by $\vec{B} = \nabla \times \vec{A}$. In the Landau gauge, the vector potential is given by $\vec{A} = (0, A_y(x), 0)$. The system can be described by the Hamiltonian given by

$$H = \frac{(\vec{p} - e\vec{A})^2}{2m^*} \tag{5.1}$$

where $\vec{p}$ is the free-electron momentum operator, e is the elementary charge and m^* the effective mass. The system is translationally invariant along the x direction, therefore the wavefunction can be written as a product of the form

$$\Psi(x, y) = e^{\imath k_x x}\psi(y) \tag{5.2}$$

where $\hbar k_x$ is the expectancy of p_x. The wavefunction $\psi(y)$ satisfies the following Schrodinger equation

$$-\frac{\hbar^2}{2m^*}\frac{\partial^2\psi(y)}{\partial y^2} + V(y, k_x)\psi(y) = E\psi(y) - \frac{\hbar^2 k_x^2}{2m^*}\psi(y) \tag{5.3}$$

where the effective potential $V(y, k_x)$ is given by

$$V(y,k_x) = \frac{\hbar^2}{2m^*}\left[k_x + \frac{e}{\hbar}A_x(y)\right]^2 \tag{5.4}$$

and the energy dispersion curves $E_n(k_x)$ of magnetic edge states are given by

$$E_n(k_x) = E_n - \frac{\hbar^2 k_x^2}{2m^*} \tag{5.5}$$

It was seen in Figure 5-1 that the magnetic field profile in the samples used in the experiments have shapes that vary from something resembling a rectangular wave to something more triangular shaped. For a matter of simplicity, a rectangular step [36, 37] will be used as the magnetic field profile for this theoretical introduction, which corresponds to one period of the magnetic superlattice. The effects are essentially the same and some unneeded complexity to explain the concept is avoided. The perpendicular component of the magnetic field is then

$$B_{1,z}(y) = B_m\left[H(y) - H(-y)\right] \tag{5.6}$$

where B_m is the modulation amplitude, i.e. the amplitude of the magnetic step, and $H(y)$ is the Heaviside function. The vector potential becomes $A_x(y) = B_m|y|$ and therefore the effective potential is now given by

$$V(y,k_x) = \frac{m^*\omega_c^2}{2}\left(\frac{\hbar k_x}{eB_m} + |y|\right)^2 \tag{5.7}$$

where ω_c is the cyclotron frequency. If the electron is propagating in the positive direction of x, $k_x > 0$ the shape of the effective potential is a double parabolic quantum well with minima at $y_0 = \pm\frac{\hbar k_x}{eB_m}$, whereas for $k_x < 0$ its a simple parabolic quantum well with the vertex at $y = 0$.

The dispersion curves $E_n(k_x)$ [3] of the first three Landau levels are represented in Figure 5-5. Assuming the magnetic edge is located at $y = 0$, for each value of momentum k_x corresponds two oscillator centres located at the vertices of the parabolic double quantum well. Depending on the Landau level, the oscillators have different cyclotron radius, given by $R_n = \sqrt{2n+1}r_m$, for a given level n,

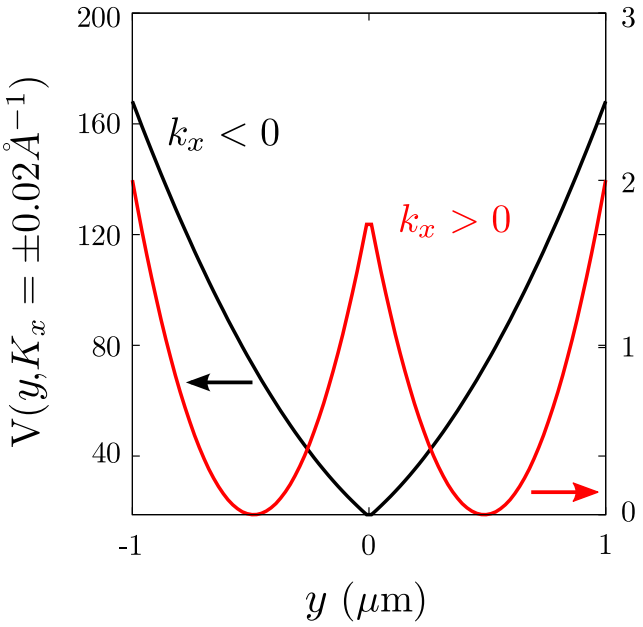

Figure 5-4: *Effective magnetic potential arising from the a stepwise magnetic field, for electron orbiting with $k_x > 0$ and $k_x < 0$.*

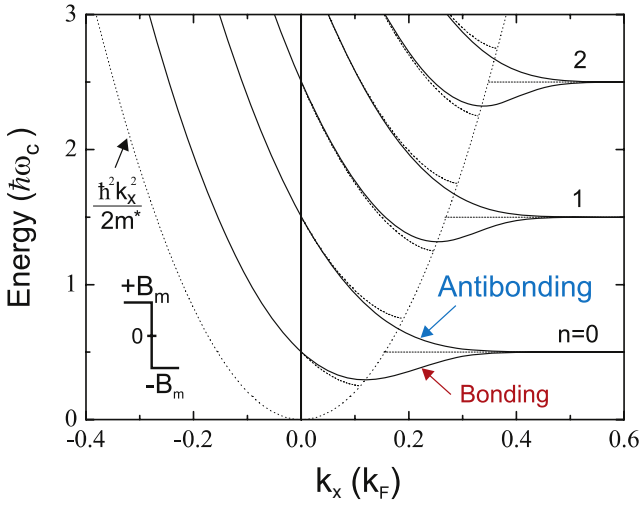

Figure 5-5: *Dispersion curves of electrons subjected to an inhomogeneous magnetic field. Figure from Nogaret [3]*

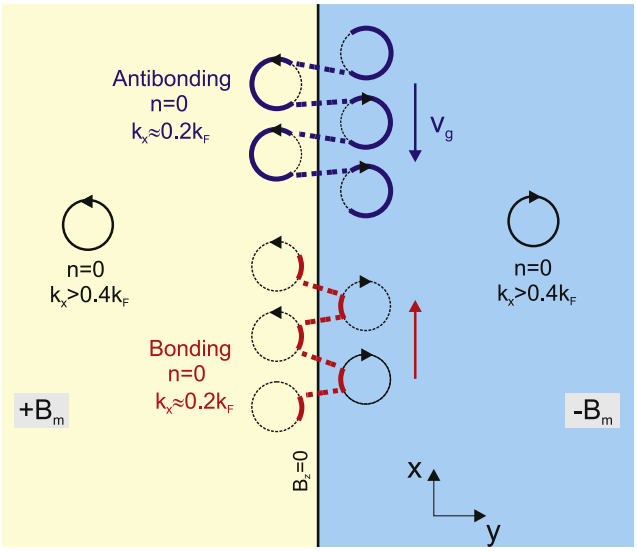

Figure 5-6: *Electron trajectories in the stepwise magnetic field. the bonding and antibonding edge states are in red and blue. Figure from Nogaret [3]*

where $r_m = \sqrt{\frac{\hbar}{eB_m}}$.

If $y_0 \gg R_n$, the oscillators are far from the magnetic edge and do not interact with each other. The Landau levels are doubly degenerate, corresponding to two states orbiting with opposite angular momentum in regions seeing a magnetic field of opposite sign, as it can be seen in Figure 5-6. If $y_0 \approx R_n$, the oscillator centres start coupling by tunnelling through the central barrier of the magnetic double quantum well. The coupling lifts the opposite angular momentum degeneracy and the system splits into the bonding and antibonding subbands. The opposite sign of the group velocity distinguishes between both subbands, being positive for the bonding states and negative for the antibonding states. At $y_0 = R_n$, the potential of the central barrier is now lower than the energy of Landau level n, the oscillators start interacting classically and the group velocity of the bonding states reverses sign. The oscillators start to drift in the negative direction of the y axis in snake orbits.

By measuring the magnetoresistance of a 2DEG subjected to a periodical magnetic potential of the kind being characterised in this section, it can be observed a V-shaped feature at low field. It is more convenient to consider a sinusoidal magnetic field profile for this case. Such feature is typical of a regime where the

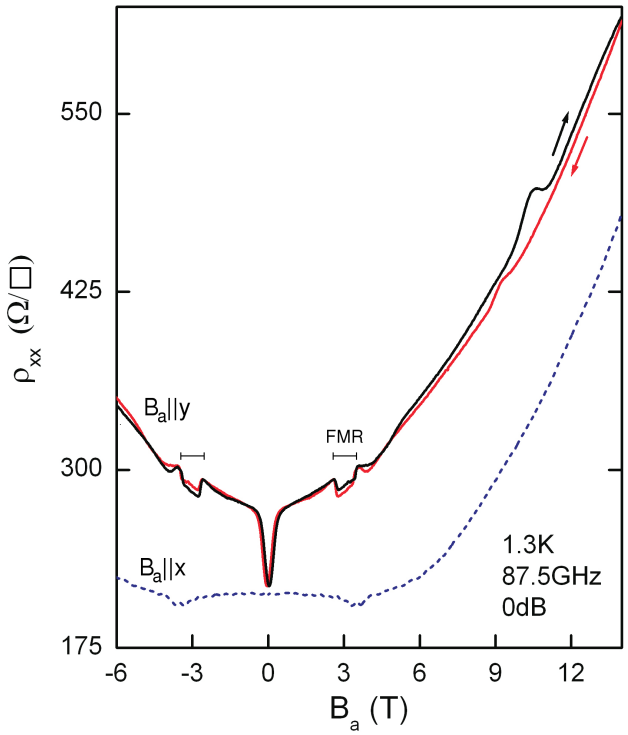

Figure 5-7: *V-shaped structure at low field observed in a magnetoresistance spectrum when the grating is magnetised in plane.*

amplitude of the inhomogeneous magnetic field is larger than the z component of the applied magnetic field, $B_m > B_{0,z}$, with $B_{0,z} = B_0 \cos\theta$, where θ is the angle between the z axis and $\vec{B}_0$. If the magnetoresistance is measured when the applied magnetic field is tilted from an orientation perpendicular to the 2DEG, $\theta = 0$, until it is in plane with the 2DEG, $\theta = \pi/2$, the amplitude of the V-shaped magnetoresistance can be observed increasing as θ approaches $\pi/2$.

When $B_m < B_{0,z}$, commensurability oscillations can be observed in the magnetoresistance. Commensurability effects are not going to be discussed because the results presented in this Thesis were obtained from measurements always made with the applied magnetic field in plane with the 2DEG, $\theta = \pi/2$, and, thus, the perpendicular component $B_{0,z} is zero, theoretically$.

The transition between both regimes is made at a value of the z component of the applied field, in which $B_{0,z} = B_m$. This allows for a direct measure of the modulation amplitude. In the regime $B_m > B_{0,z}$, the 2DEG has a sequence of

alternated regions of positive and negative magnetic field. Between two adjacent regions of opposite sign, the Lorentz force sign is toggled, deflecting electrons accordingly towards the magnetic edge. These are the conditions for the formation of snake orbits, which is what induces the V-shaped magnetoresistance.

In the semiclassical drift diffusion model [3], let it be assumed the electrons drift with Fermi velocity v_F when no snake orbits are formed. When electrons wiggle about the magnetic edges, their drift velocity v_d is a fraction of the Fermi velocity, $v_d = v_F \sin\phi/\phi$ [3]. The orbit crosses the magnetic edge with an angle ϕ. There is a critical angle, ϕ_{max}, such that if $\phi > \phi_{max}$, the electron escapes the confinement felt in a snake state and becomes cycloid-like. The angle ϕ_{max} can be obtained by knowing

$$\cos[(\pi - \phi_{max})/2] = Ql_b \tag{5.8}$$

where $Q = 2\pi/a$, $l_b = \sqrt{\hbar k_F/eb}$ and $b = QB_m$ is an approximation of the field gradient at the magnetic edge.

When in a cycloid orbit, the electron describes loops at the Fermi velocity v_F. The drift velocity of cycloid orbits corresponds to the velocity of the guiding center of the loops, therefore the drift velocity of cycloid orbits is much slower than the Fermi velocity, being considered stationary in comparison with snake orbits. The longitudinal component of the diffusion tensor D_{yy} is therefore corrected by averaging the drift velocity over the whole bundle of snake orbits as

$$\delta D_{yy} = \langle v_d^2 \rangle \frac{\tau}{2} \tag{5.9}$$

From the Einstein equation, the resistivity tensor is inversely proportional to the diffusion tensor

$$\vec{\rho} = \frac{1}{Ne^2\vec{D}} \tag{5.10}$$

where $N = 4\pi m^*/h^2$, whereas the diffusion tensor is proportional to the average

of the drift velocities. Therefore, if the diffusion tensor is decreased, the resistivity tensor increases, explaining the rise of the magnetoresistance as the snake orbits are formed. Quantitatively, the increment in magnetoresistance when the magnetic potential is present is

$$\frac{\Delta\rho_{xx}}{R_0} = 2(\mu B_z)^2 \frac{\langle v_d^2 \rangle}{v_F^2} \tag{5.11}$$

where μ is the mobility of the 2DEG. In approximation [38], $\langle v_d^2 \rangle \approx v_F^2(\phi_{max}/\pi)$, therefore Equation 5.11 becomes

$$\frac{\Delta\rho_{xx}}{R_0} = \frac{2\phi_{max}}{\pi}(\mu B_z)^2 \tag{5.12}$$

Reijniers *et al* [39] presented an alternative explanation based instead on the Landauer-Buttiker formula. The rise in magnetoresistance is explained succintly: increasing the magnetic field increases the separation between magnetic subbands, which decreases the number of conducting channels, leading to an increase of the longitudinal component of the resistivity tensor.

In the case where the inhomogeneous magnetic field has zero average, $B_{0,z} = 0$, therefore there is no transition between regimes. The cutoff of the V-shaped magnetoresistance can still be observed. The amplitude of the inhomogeneous magnetic field depends on the magnetisation, which in its turn depends on the applied field B_0. When the magnetoresistance is increasing, the magnetisation is still being increased as well. The cutoff of the V-shaped feature corresponds to the minimum applied magnetic field that saturates the magnetisation. When the magnetisation is saturated, the amplitude of the inhomogeneous magnetic field is maximum.

This section will be finalised with the characterisation of the classical trajectories of the snake orbits. The frequency with which the electrons oscillate about the zero field edge is derived from the semiclassical equation of motion of electrons on the Fermi surface [40].

Let $\tilde{y}$ be the amplitude of the oscillations of the snake orbits. The amplitude $\tilde{y}$ is

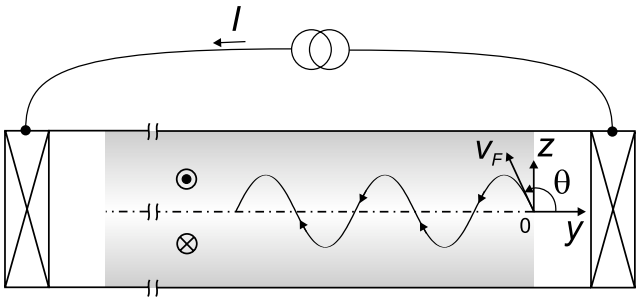

Figure 5-8: *Two adjacent regions of a 2DEG subjected to perpendicular magnetic fields of opposite sign. At the boundary, where the magnetic field is zero, spins oscillate with frequency and amplitude given by Eqs. 5.13 and* $Y = \pm\cos(\pi/2)$. *Figure from Nogaret et al [4].*

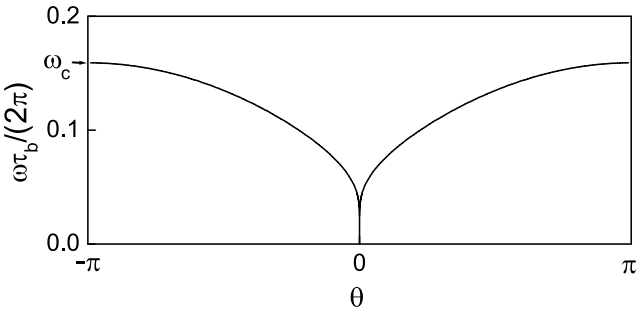

Figure 5-9: *Continuous spectrum of snake orbit frequencies as a function of the initial angle* θ. *Figure from Nogaret et al [4].*

related to the angle θ, which is the angle between the Fermi velocity vector of an oscillator and the magnetic edge, by the relation $\tilde{y} = (2/Q)\arcsin[\cos(\theta/2)/\gamma]$, where Q is the wavevector and $\gamma = Ql$. The length scale of oscillations l is given by $l = \sqrt{\hbar k_F/(eb)}$, where b is the effective magnetic gradient given by $b = Q\tilde{B}_1$ and $\tilde{B}_1$ is the amplitude of magnetic modulation. The angular frequency of the oscillator $\omega_1(\theta)$ is

$$\omega_1(\theta) = \frac{\tilde{\omega_1}}{4F(\pi/2, \theta)} \tag{5.13}$$

where

$$F(\pi/2, \theta) = \int_0^{\pi/2} \frac{d\alpha}{\sqrt{1 - \cos^2\frac{\theta}{2}\left(1 + \gamma^2 \sin^2\frac{\theta}{2}\right)\sin^2\alpha}} \tag{5.14}$$

The frequency cutoff $\tilde{\omega_1}$ is given by $\tilde{\omega_1} = \sqrt{\hbar k_F e b}/m^*$

The dispersion curve of the snake orbit modes of oscillation is depicted in Figure 5-9. It can be concluded there is at all times a bundle of snake orbits with a continuous spectrum of frequencies, within a certain range.

Electrons doing this periodical transversal motion in magnetic field gradients are therefore subjected to an effective *ac* magnetic field whose frequency is the same as the frequency of the periodical motion ω_1 and whose amplitude is equivalent to the modulation field B_m.

5.2 Dark state in the coherent population trapping framework

Between states in an atom, the interference between alternative excitation pathways leads to modified optical response [10]. The response of an atom to resonant absorption of electromagnetic radiation is described by the first order susceptibility $\chi^{(1)}$. The real part of the susceptibility, $Re[\chi^{(1)}]$ corresponds to the refractive

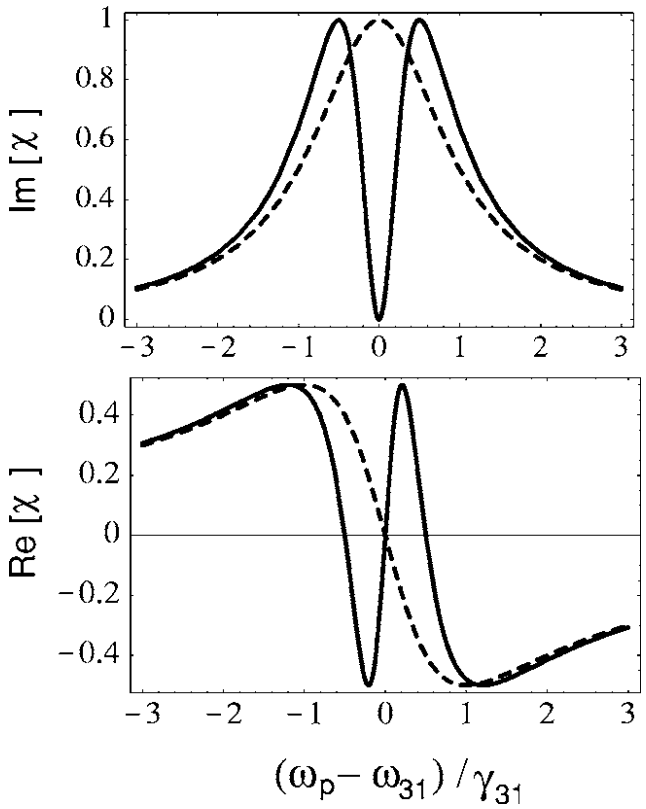

Figure 5-10: *(top) First order susceptibility as a function of the frequency ω_p of the applied field, detuned from the atomic resonance frequency ω_{31} with a relaxation rate γ_{31} (dashed line) and an EIT system with resonant coupling field (solid line). (top) absorption; (bottom) Reffractive index.*

index, which is a measure of how quick does an electromagnetic wave travel in a medium, whereas the imaginary part of the susceptibility $Im[\chi^{(1)}]$ corresponds to the absorption of energy. The frequency dependence of the absorption $Im[\chi^{(1)}]$ has the shape of a Lorentzian, whose width is dependent on the damping.

If the frequency corresponding to the interaction energy is larger than the characteristic linewidth, the evolution of such system must be described in terms of density matrix equations. Thus, the atom-states must evolve coherently, i.e., the phase information must be retained. Coherent evolution of a two-level system is characterised by oscillatory population transfer, Rabi flopping. Generalising this picture to a three-level system leads to the observation of anomalies in the susceptibility as shown in Figure 5-10.

Figure 5-10 shows the real and imaginary parts of the first-order susceptibility

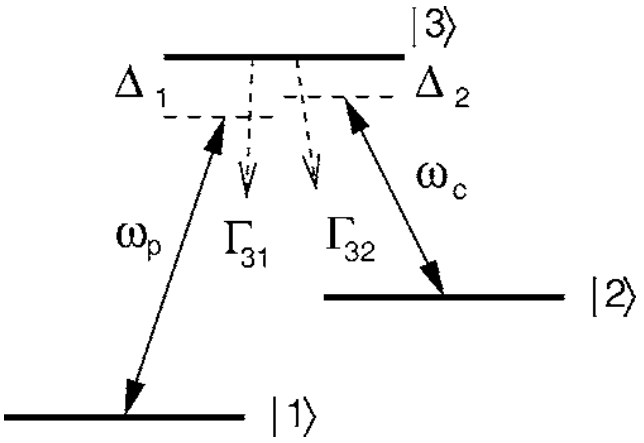

Figure 5-11: *Lambda system with a probe field of frequency ω_p and a coupling field of frequency ω_c. $\Delta_1 = \omega_{31} - \omega_p$ and $\Delta_2 = \omega_{32} - \omega_p$ are the detunings from resonance of both transitions.*

$\chi^{(1)}$ of a resonant coupling field in a three-level system as function of the probe field detuning from the resonance frequency. It can be concluded already that the interference is destructive, by the dip in absorption in the vicinity of the resonant frequency. It means the medium becomes transparent to probe field. There are several types of three-level systems but the focus will be on the one in Figure 5-11, called Λ-type.

The cancellation of the absorption is explained by the formation of a dark state where the population becomes trapped and no transition is possible. The derivation of the response of an Λ-type atom where a dark state is formed follows, drawing heavily from Fleischhauer *et al* [10]. The derivation of the susceptibility in this reference was made for Λ-type atoms slightly different than the Λ-type system used in our experiments, while being irradiated with laser fields. It will serve as a reference at a later stage in the Thesis, where it will be proved that the response of our system, derived from the magnetic susceptibility, is identical to the susceptibility of systems used in the electromagnetic induced transparency framework.

Consider a Λ-type system (Figure 5-11) with two near-resonant fields being irradiated at it. The Hamiltonian of the system becomes $H = H_0 + H_{int}$, where H_0 is the Hamiltonian of the bare atom and H_{int} is the Hamiltonian of the interaction. In the dipole approximation, the interaction Hamiltonian is expressed in terms

of the Rabi frequency Ω, such that $H_{int} = \vec{\mu} \cdot \vec{E}$ and $\Omega = \vec{\mu} \cdot \vec{E}_0/\hbar$, where E_0 is the amplitude of the electric field $\vec{E}$ and $\vec{\mu}$ the electronic dipole moment of the transition. The interaction Hamiltonian is then given by

$$H_{int} = -\frac{\hbar}{2} \begin{bmatrix} 0 & 0 & 0 \\ 0 & -2(\Delta_1 - \Delta_2) & \Omega_c \\ \Delta_p & \Delta_c & -2\Delta_1 \end{bmatrix} \tag{5.15}$$

where Ω_c and Ω_p are Rabi frequencies of the coupling and probe transition, $\Delta_1 = \omega_{31} - \omega_p$ and $\Delta_2 = \omega_{32} - \omega_c$ are the detunings of the probe and coupling field frequencies ω_p and ω_c from resonance. The eigenstates of Equation 5.15 are going to be expressed in terms of the "mixing angles" θ and ϕ and the single-photon ($\Delta_1 = \Delta$) and two-photon ($\delta = \Delta_1 - \Delta_2$) detunings. In the case of a two-photon resonance ($\delta = 0$) the mixing angles are defined as

$$\tan\theta = \frac{\Omega_p}{\Omega_c} \tag{5.16}$$

$$\tan 2\phi = \frac{\sqrt{\Omega_p^2 + \Omega_c^2}}{\Delta} \tag{5.17}$$

Finally, the eigenstates are given by

$$|a^+\rangle = \sin\theta \sin\phi|1\rangle + \cos\phi|3\rangle + \cos\theta \sin\phi|2\rangle \tag{5.18}$$

$$|a^0\rangle \cos\theta|1\rangle \sin\theta|2\rangle \tag{5.19}$$

$$|a^-\rangle = \sin\theta \cos\phi|1\rangle + \sin\phi|3\rangle + \cos\theta \cos\phi|2\rangle \tag{5.20}$$

What matters to observe here is $|a^0\rangle$ is the only state which has no component in $|3\rangle$, therefore it is the dark state. If the system ends up in state $|a^0\rangle$ there is no possibility of transferring population to $|3\rangle$ therefore arresting further Rabi

flopping.

It will now be proceeded towards the derivation of the susceptibility of such system. The atomic polarisation is given by

$$P(t) = \varrho[\mu_{13}\rho_{31}e^{-i\omega_{31}t} + \mu_{23}\rho_{32}e^{-i\omega_{32}t}] \tag{5.21}$$

where $\varrho = N_{atom}/V$ and ρ_{31} and ρ_{32} are off-diagonal elements of the density matrix $\hat{\rho}$. These elements are determined through the master equation, which relates the density matrix $\hat{\rho}$ with the interaction Hamiltonian H_{int}. The master equation is given as Equation 9 in Ref. [10]. The off-diagonal elements of the density matrix that matter are

$$\begin{aligned}
\rho_{32} &= \frac{i\Omega_c e^{i\Delta_1 t}}{\gamma_{32} + i2\Delta_2}\rho_{12} \\
\rho_{12} &= -\frac{i\Omega_c e^{i\Delta_2 t}}{\gamma_{21} + i2(\Delta_2 - \Delta_1)}\rho_{13} \\
\rho_{31} &= \left(\frac{i\Omega_p e^{i\Delta_1 t}}{\gamma_{31} + i2\Delta_1} + \frac{i\Omega_c e^{i\Delta_2 t}}{\gamma_{31} + i2\Delta_1}\right)\rho_{21}
\end{aligned} \tag{5.22}$$

The susceptibility is derived through the relation $P = \chi\epsilon_0 E_p$, where $E_p = \hbar\Omega_p/\mu_{13}$:

$$\begin{aligned}
\chi^{(1)}(-\omega_p, \omega_p) = \frac{|\mu_{13}|^2\varrho}{\epsilon_0\hbar}\Bigg[&\frac{4\delta(|\omega_c|^2 - 4\delta\Delta) - 4\Delta\gamma_{21}^2}{||\omega_c|^2 + (\gamma_{31} + i2\Delta)(\gamma_{21} + i2\delta)|^2} \\
&+ i\frac{8\delta^2\gamma_{31} + 2\gamma_{21}(|\Omega_c|^2 + \gamma_{21}\gamma_{31})}{||\omega_c|^2 + (\gamma_{31} + i2\Delta)(\gamma_{21} + i2\delta)|^2}\Bigg]
\end{aligned} \tag{5.23}$$

5.3 Results

Measurements were performed in Sample D, which is a device equipped with a Cobalt grating with 400 nm of period. The sample was irradiated with microwaves within the 35-110 GHz range and was cooled down to approximately

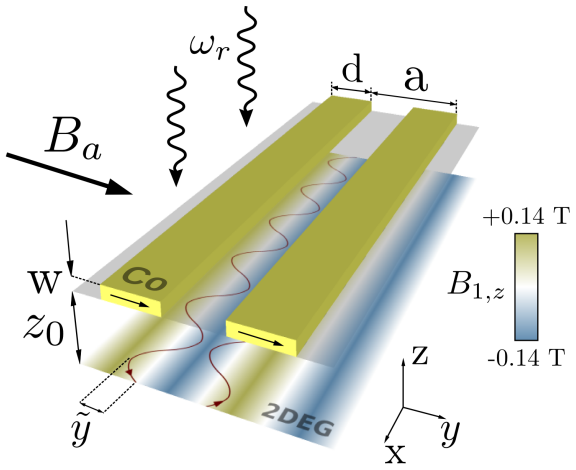

Figure 5-12: *Schematic of the active region of a Hall bar etched from a GaAs/AlGaAs heterojunction with a Cobalt grating deposited at the surface.*

1.4 K, except when performing the temperature dependence. An *ac* current of 500nA was applied longitudinally to the 2DEG and the magnetoresistance was measured by low frequency (13 Hz) lock-in detection. The Cobalt micromagnets were magnetised with an external magnetic field B_a in-plane with respect to the sample. By orienting the field B_a across (along) the Co wires, it was possible to toggle the magnetic modulation detected in the 2DEG on (off). When the wires are magnetised transversely, magnetic poles are formed in the facets perpendicular to the field B_a. The magnetic poles of each wire generate a stray magnetic field whose component perpendicular to the sample subjects the 2DEG to a spatially varying magnetic field, which is periodic in the y axis direction with average magnitude equal to zero (Section 5.1). The inhomogeneous magnetic field oscillates with the same period a of the magnetic array and is defined approximately by

$$B_1(y) = \begin{cases} 0 \\ \tilde{B}_1 \cos(Qy) \\ -\tilde{B}_1 \sin(Qy) \end{cases}$$

where $Q = 2\pi/a$. Higher harmonics exist (Appendix B) but were considered negligible due to the large separation between the 2DEG and the magnetic array. As

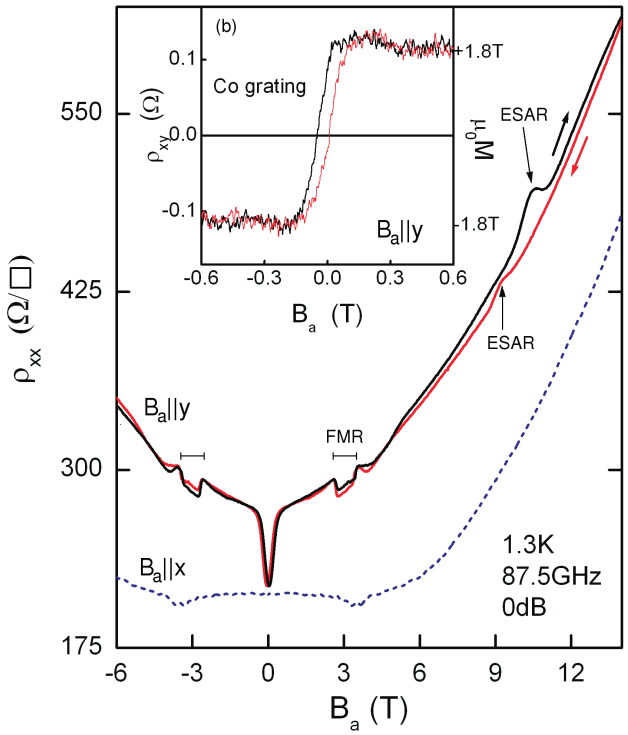

Figure 5-13: *Magnetoresistance of the cobalt superlattice when $B_a||y$ (full lines) and $B_a||x$ (dotted lines).*

mentioned in Section 5.1, part of the ballistic electrons drifting under the influence of the effective potential of such magnetic profile do snake-like trajectories along the line where the inhomogeneous field gradient cancels.

The field B_a also lifts the electron spin degeneracy and enables the spin precession around the vector B_a with Larmor frequency given by $\omega_0 = g_{\|}\mu_B B_a/\hbar$ (Section 2.5). In order to avoid any residual perpendicular component of the field which could change the inhomogeneous field profile considerably, which would destroy the snake orbits, the sample was carefully aligned with the field B_a by minimising the Hall resistance of the 2DEG (Section 3.2).

In Figure 5-13 is depicted the dependence of the resistivity ρ_{xx} with the external magnetic field B_a. The curves with solid lines correspond to the $B_a\|y$ case whereas the dashed line corresponds the field is oriented as $B_a\|x$. Three features easily stand out and will be characterised next. First, when $B_a\|y$, a V-shaped structure develops at low field within the $B_a = \pm 0.3$T range. It does not appear

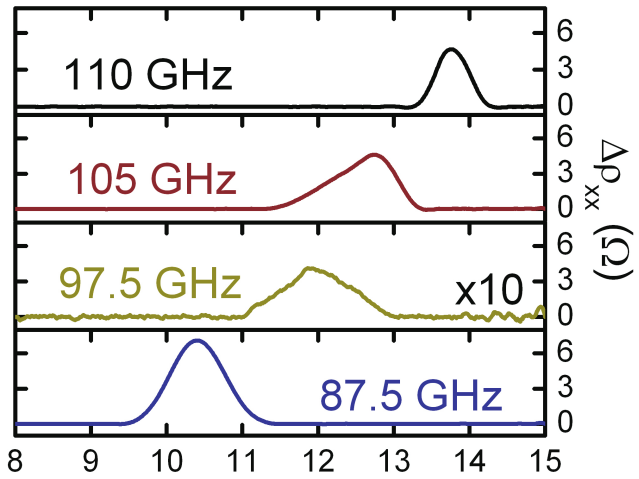

Figure 5-14: *Frequency dependence of the ESAR peak.*

when $B_a \| x$ thus it should be an effect originated by the magnetic modulation. As it was seen in Section 5.1, the applied field cutoff of the V-shaped structure is good estimate of the amplitude of the magnetic modulation imposed by the grating.

The cutoff corresponds approximately to a magnetic modulation of $\tilde{B}_1 = 0.150T$ Calculating the stray field coming from the grating [41, 36] as

$$\tilde{B}_1 = \mu_0 M_y/(2\pi)\sin(Qd/2)\sinh(Qw/2)\exp(-Q[z_0 + w/2]) \tag{5.24}$$

for a grating with dimensions as in Figure 5-12 and using the tabulated saturation magnetisation $\mu_0 M_y = 1.82$ T, it returns $\tilde{B}_1 = 0.141$ T, which agrees with the value estimated from the experimental results. The second feature can be found whether $B_a \| x$ or $B_a \| y$ and is located in the vicinity of $B_a = 3$T. The broad structure corresponds to the electrical detection of dipolar magnetic waves studied in the previous chapter.

The focus now turns to the subject of this chapter which is the peak labelled as ESAR (Electron Spin Anti-Resonance) in Figure 5-13. Necessary conditions to the detection of ESAR are the presence of both the microwaves and the periodic magnetic potential. When the magnetic modulation is switched off but the 2DEG is still irradiated with microwaves the peak vanishes, as it can be observed in

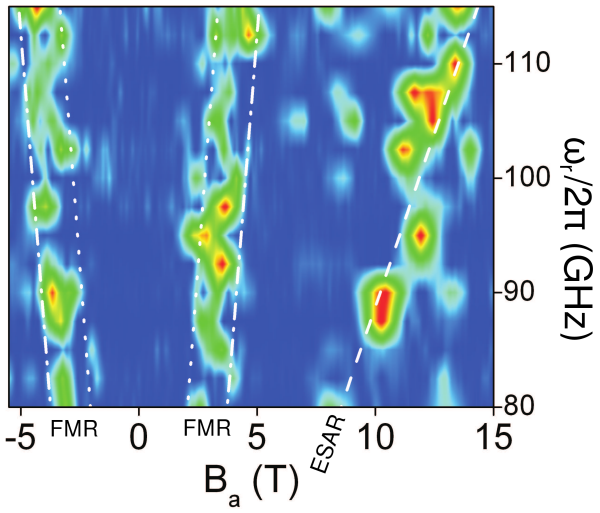

Figure 5-15: *Microwave induced resistance mapped as a function of microwave frequency and* $B_a||y$.

the curve with dashed line. While there is no doubt that the electron spins of an unmodulated 2DEG are in resonance like the modulated case, spin flipping transitions never change the net conductivity and therefore its electrical detection is unattainable. Even if spin flips change the conductivity of spin-up and spin-down channels, they change at the expense of each other, therefore conserving net conductivity. Bolometric effect is ruled out as well with the presented evidence as it would enable the detection of electron spin resonance in a 2DEG in the ballistic regime and there is no evidence of such with the absence of a magnetic potential ($B\|x$).

The dependence of ESAR with the microwave frequency is shown in Figure 5-14. A more complete representation of the dependence results is in the color map in Figure 5-15 where is plotted the microwave induced resistance $|\Delta\rho_{xx}^{\mu W}|$, which was obtained by subtracting the background resistance measured at zero microwave power. The peak positions for each frequency were fitted with a least squares method, weighted by the amplitude of the peaks, with a model of the form

$$\omega_r = \frac{g_{\|}\mu_B}{\hbar}(B_a + B_N) \tag{5.25}$$

where ω_r is the angular frequency of the microwaves, μ_B is the Bohr magneton

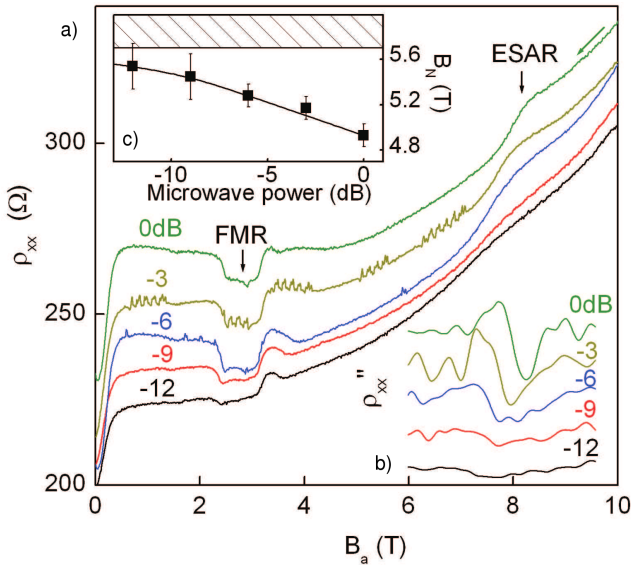

Figure 5-16: *a) Dependence of ρ_{xx} on microwave power; b) second derivative of the resistance curves near the ESAR peak; c) Overhauser shift as a function of microwave power.*

and $g_{\|}$ is the Lande g-factor in the quantum well. The best fit occurs for the parameters $|g_{\|}| = 0.43 \pm 0.04$ and $B_N = 4.53T \pm 0.3T$.

The term B_N is the Overhauser shift due to the dynamic polarisation of nuclear spins [42, 43], as it was introduced in Section 2.7.

Figure 5-16 shows the dependence of the Overhauser shift with the microwave power. In Figure 5-16.c), B_N decreases from 5.6T at -12dB to 4.9T at 0dB. By extrapolating the fit to -∞ dB, B_N saturates at $5.7T \pm 0.2T$. This value is close to the maximum value for the Overhauser shift in GaAs, previously estimated by Paget *et al* [9]. In the inset (b) of Figure 5-16, the second derivative of the resistivity ρ_{xx} was plotted to enhance the peaks. As it was shown in Section 5.1, electrons propagating in snake-orbits feel a time dependent magnetic field $B_{1,z}(t)$ due to the periodical transversal movement when drifting along the inhomogeneous magnetic field gradient. This means that besides the MESR, electron spins can resonate when driven by $B_{1,z}(t)$ as well (SESR). It was observed as well that ESR using this route is always resonant in the range of field B_a applied in the experiment, meaning that whenever the field B_a is being swept, the nuclear spins are constantly being polarised through hyperfine interaction

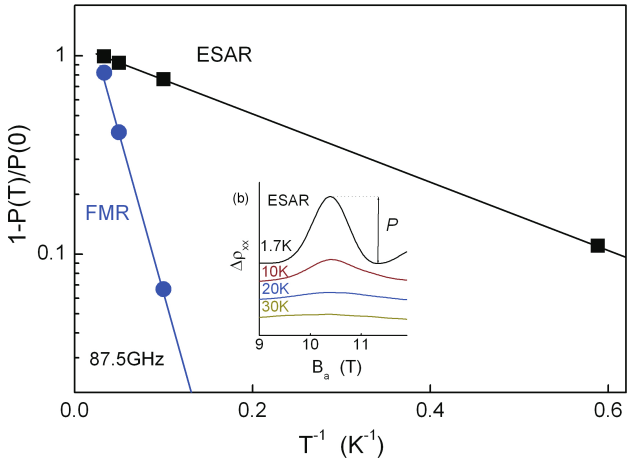

Figure 5-17: *a) Thermal activation of ESAR and FMR peak amplitudes; b) temperature depedence of the amplitude of the ESAR peak.*

with the electron spins in resonance, hence the satured B_N. In Section 5.2 was concluded that when such system is in the condition of microwave induced ESR, the two transitions interfere destructively and the SESR transition is blocked. This is consistent with the picture of decreasing B_N with increasing microwave power, because the source for saturated DNP is destroyed in the moment B_N is measured.

The Landé g-factor can be estimated from the analysis of the temperature dependence of the ESAR peak amplitude. The peak amplitude is assumed to be proportional to the fraction of redistributed spins

$$\frac{N_\uparrow - N_\downarrow}{N_\uparrow} = 1 - e^{\frac{-\Delta_Z}{k_B T}} \tag{5.26}$$

where Δ_Z is the Zeeman gap. Figure 5-17.b) shows the temperature dependence of the ESAR peak amplitude. The amplitudes for each temperature were extracted and following the thermal activation law

$$P(T) = P(0)\left(1 - e^{\frac{-\Delta_Z}{k_B T}}\right) \tag{5.27}$$

it was plotted $1 - P(T)/P(0)$ vs. $1/T$. Please note that the ordinate of the plot

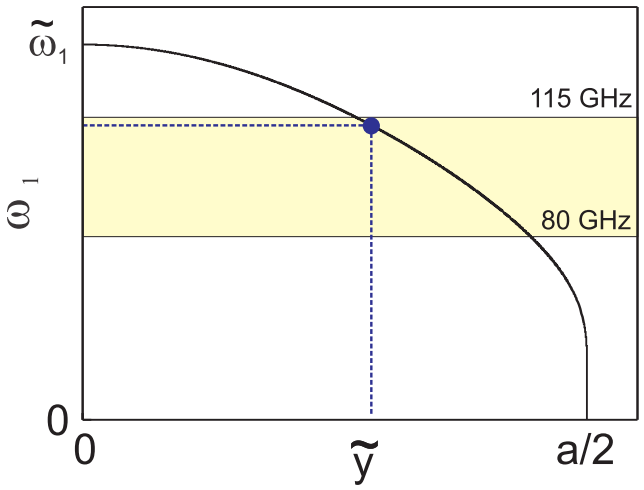

Figure 5-18: *Frequency spectrum of snake oscillators.*

is in log scale. The ratio P(1.7K)/P(0) = 0.89 was determined from a linear fit and from that value it was extracted the activation energy as $\Delta_Z = 0.342$meV. Equating the activation energy to the Zeeman gap, given by $\Delta_Z = g_{\|}\mu_B(B_a + B_N)$ and using the values of B_a and B_N determined for the ESAR at 87.5 GHz, the g-factor was determined as $g_{\|} = 0.40$, which corresponds to the Landé g-factor determined through the frequency dependence, within experimental error. The theoretical value for a 15nm wide GaAs quantum well is $g_{\|} = -0.42$ [44].

After discussing the position of the ESAR peak in the magnetoresistance spectrum, it is now going to be analysed the existence of the peak itself. The ESAR is the destructive interference between ESR transitions induced by different *ac* magnetic fields: the magnetic component of the microwaves and the field $B_{1,z}(t)$ felt by the snake oscillators. The energy of the SESR transition can be known if it is determined the frequency of the snake trajectories. Based in a semiclassical model of snake orbits (Section 5.1), the frequency of the oscillation of a snake trajectory is given by Equation 5.13 with $\gamma = Ql = 2.7$, $l = \sqrt{\hbar k_F/(eB)} = 172nm$, $b = Q\tilde{B}_1 = 2.2T/\mu m$ and $\tilde{\omega}_1 = \sqrt{\hbar k_F e b}/m^*$.

The frequency spectrum of $\omega_1(\tilde{y})$ is plotted in Figure 5-18. The frequency cutoff is at $\tilde{\omega}_1/2\pi = 150$GHz and corresponds to the snake states with $\tilde{y} \simeq 0$. For orbits whose amplitude reach half of the period of the superlattice, the frequency falls to zero. The Rabi frequency Ω_1 depends on the maximum value of $B_{1,z}$ each snake oscillator sees and is given by $\Omega_1 = |g_{\|}|\mu_B B_{1,z}(\tilde{y})/\hbar$ and is plotted in Figure 5-19.

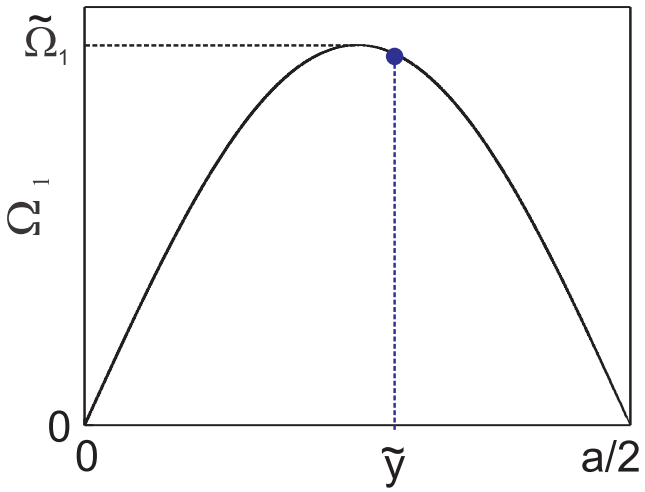

Figure 5-19: *Rabi frequency of the snake oscillators plotted as a function of the oscillator amplitude.*

The Rabi frequency peaks at $\tilde{\Omega}_1/(2\pi) = 0.81\text{GHz}$.

From Section 5.2's picture, the three states coupled by these two transitions are disposed in the Λ-configuration (Figure 5-20). The spin down states are labelled as $|\downarrow, N>$ and $|\downarrow, N+1>$ and the spin up state as $|\uparrow, N>$. The transition (ω_1, Ω_1), as it was discussed before, is always resonant because the frequency spectrum covered by the field B_a range used in the experiment is continuous. Therefore, there is always an oscillator mode excited by the Larmor frequency that meets the $\omega_r = \omega_0$ condition. As the field B_a is swept, transition (ω_r, Ω_r) is detuned from resonance by $\Delta = \omega_0 - \omega_r$. When it crosses resonance with $\Delta = 0$, the two spin down states hybridise to form a dark state defined by

$$|d\rangle = \frac{\Omega_1}{\sqrt{\Omega_1^2 + \Omega_r^2}}|\downarrow, N+1\rangle - \frac{\Omega_r}{\sqrt{\Omega_1^2 + \Omega_r^2}}|\downarrow, N\rangle \tag{5.28}$$

Since $|d\rangle$ has no term with $|\uparrow, N\rangle$, there is no way out until the microwave transition is detuned again. The dark state blocks transitions and the oscillators are scattered from their snake trajectories, affecting the conductivity. In the linear response regime, resistivity ρ_{xx} increases linearly to the fraction of snake orbits trapped in the dark state. This fraction is the probability of forming the dark state P_{dark} and is obtained by calculating the expectancy of the density matrix

of the system in the dark state $\langle d|\hat{\rho}|d\rangle$.

A derivation of the probability of forming the dark state in the three level system of Figure 5-20 consisting of $|1\rangle, |2\rangle, |3\rangle \equiv |\uparrow, N\rangle, |\uparrow, N+1\rangle, |\downarrow, N\rangle$. It was used the first notation for simplicity. The Hamiltonian of the unperturbed system is $H_0 = 0|1\rangle + 0|2\rangle + \hbar\omega_0|3\rangle$. The three levels interact via transition (ω_1, Ω_1) which is always resonant and (ω_r, Ω_r) which is detuned from resonance by $\Delta = \omega_0 - \omega_r$. The interaction Hamiltonian of the Λ scheme is given by

$$H_{int} = \begin{bmatrix} 0 & 0 & \Omega_r \\ 0 & -2\Delta & \Omega_1 \\ \Omega_r & \Omega_1 & -2\Delta \end{bmatrix} \tag{5.29}$$

The components of the density matrix $\hat{\rho}$ of the spin ensemble evolve according to:

$$\begin{aligned}
\dot{\rho}_{11} &= \frac{i}{2}\Omega_r(\rho_{31} - \rho_{13}) + \rho_{33}\frac{\gamma_L}{2} \\
\dot{\rho}_{22} &= \frac{i}{2}\Omega_r(\rho_{32} - \rho_{23}) + \rho_{33}\frac{\gamma_L}{2} \\
\dot{\rho}_{33} &= \frac{i}{2}[\Omega_r(\rho_{13} - \rho_{31}) + \Omega_1(\rho_{23} - \rho_{32})] + \rho_{33}\gamma_L \\
\dot{\rho}_{12} &= \frac{i}{2}[\Omega_r\rho_{32} - \Omega_1\rho_{13}] + \frac{1}{2}\rho_{12}(2i\Delta - \gamma_T) \\
\dot{\rho}_{13} &= \frac{i}{2}[\Omega_r(\rho_{33} - \rho_{11}) - \Omega_1\rho_{12}] + \frac{1}{2}\rho_{13}(2i\Delta - \gamma_L) \\
\dot{\rho}_{23} &= \frac{i}{2}[\Omega_1(\rho_{33} - \rho_{22}) - \Omega_r\rho_{21}] + \frac{1}{2}\rho_{23}(0 - \gamma_L)
\end{aligned} \tag{5.30}$$

where γ_L, γ_T are the longitudinal and transverse spin scattering rates. Time independent solutions of the system are found by successive approximations first retaining only terms in Ω_1 since $\Omega_1 \gg \Omega_r$. It was assumed as initial conditions $\rho_{11} \approx 1$, $\rho_{22} \approx 0$, $\rho_{33} \approx 0$. These are inserted in Eqs. 5.30 to obtain:

$$\begin{aligned}\rho_{32} &= \frac{i\Omega_r e^{-i\Delta t}}{} \rho_{21} \\ \rho_{12} &= \frac{i\Omega_1}{\gamma_T - 2i\Delta}\rho_{13} \\ \rho_{31} &= \frac{i\Omega_r e^{i\Delta t}}{\gamma_L + 2i\Delta} + \frac{i\Omega_1}{\gamma_L + 2i\Delta}\rho_{21}\end{aligned} \tag{5.31}$$

These equations are similar to Equation 12 in Ref [10]. First order solutions are:

$$\begin{aligned}\rho_{32} &= \frac{-i\Omega_r(\gamma_T - 2i\Delta)}{\Omega_1^2 + (\gamma_L - 2i\Delta)(\gamma_T - 2i\Delta)} e^{-i\Delta t} \\ \rho_{12} &= \frac{-\Omega_r\Omega_1}{\Omega_1^2 + (\gamma_L - 2i\Delta)(\gamma_T - 2i\Delta)} e^{-i\Delta t} \\ \rho_{31} &= \frac{-i\Omega_1\Omega_r^2}{\gamma_L[\Omega_1^2 + (\gamma_L - 2i\Delta)(\gamma_T - 2i\Delta)]}\end{aligned} \tag{5.32}$$

First order solutions are usually sufficient to calculate the susceptibility of the magneto-dipole transition. Using $\chi_r = M/H_r = 2n_s g_{||}\mu_B\rho_{12}e^{i\Delta t}/H_r$ and recalling the Rabi frequency $\Omega_r = g_{||}\mu_B\mu_0 H_r/\hbar$, it is verified that it is re-obtained the standard susceptibility [10].

$$\chi_r = \frac{(g_{||}\mu_B)^2}{\hbar}\mu_0 n_s \left\{ \frac{4\Delta(\Omega_1^2 - 4\Delta^2) - 4\gamma_T^2\Delta}{|\Omega_1^2 + (\gamma_L + 2i\Delta)(\gamma_T + 2i\Delta)|^2} + i\frac{8\gamma_L\Delta^2 + 2\gamma_T(\Omega_1^2 + \gamma_L\gamma_T)}{|\Omega_1^2 + (\gamma_L + 2i\Delta)(\gamma_T + 2i\Delta)|^2} \right\} \tag{5.33}$$

The probability of forming the dark state however requires finding the second order corrections in ρ_{11} and ρ_{22}. This is done by injecting ρ_{13} of Equation 5.32 into $\dot{\rho}_{11}$ of Equation 5.30 to obtain:

$$\rho_{33} = 2\frac{\Omega_p^2}{\gamma_L}\frac{\gamma_T(\Omega_1^2 + \gamma_L\gamma_T) + 4\Delta^2\gamma_L}{|\Omega_1^2 + (\gamma_L + 2i\Delta)(\gamma_T + 2i\Delta)|^2} \tag{5.34}$$

Element $\dot{\rho}_{13}$ of Equations 5.30 then gives the second order correction $\delta\rho_{11} = \rho_{33}$. The probability of the system falling in the dark state as it crosses resonance can now be calculated. The dark state is given by Equation 5.28. The state

of the system is $|\psi(t)\rangle = c_1(t)|1\rangle + c_2(t)|2\rangle + c_3(t)e^{-\omega_0 t}|3\rangle$, hence the dark state probability is:

$$\begin{aligned} P_{dark} &= |\langle D|\psi(t)\rangle|^2 \\ &= \langle D|\psi(t)\rangle\langle\psi(t)|D\rangle \\ &= \langle D|\hat{\rho}|D\rangle \end{aligned} \tag{5.35}$$

$$P_{dark} = \frac{1}{\Omega_1^2 + \Omega_r^2}(\Omega_1^2 - \Omega_1\Omega_r(\rho_{12} + \rho_{21}) + \Omega_r^2) \tag{5.36}$$

It is used the hermiticity of the density matrix, ρ_{12} of Equation 5.32 and Equation 5.34 and it was assumed that for conduction electrons $\gamma_T \cong \gamma_L$ to obtain:

$$P_{dark} = \frac{4\Omega_1^2\Omega_r^2}{\Omega_1^2 + \Omega_r^2}\frac{\Omega_1^2 + \gamma_L\gamma_T}{|\Omega_1^2 + (\gamma_L + 2i\Delta)(\gamma_T + 2i\Delta)|^2} \tag{5.37}$$

The total conductivity of the 2DEG in such circumstance is given by the sum of the contribution of the snake states not trapped in the dark state and the contribution of all other states, Σ

$$\sigma_{xx}^{\mu W} = \sigma_s(1 - P_{dark}) + \Sigma \tag{5.38}$$

Without microwaves, no snake states are blocked and therefore the conductivity would be $\sigma_0 = \sigma_s + \Sigma$. The microwave induced resistivity is then given by

$$\frac{\rho_{xx}^{\mu W}}{\rho_0} = \frac{1}{1 - \rho_0\sigma_s P_{dark}} \tag{5.39}$$

It can be seen from 5.39 that if P_{dark} is raised from zero, the denominator decreases and therefore $\rho_{xx}^{\mu W}/\rho_0$ increases. It can be concluded that $\Delta\rho_{xx}^{\mu W} \propto P_{dark}$, which explains the observation of the ESAR peak. The increment in resistivity of the 2DEG is given by

$$\frac{\Delta\rho_{xx}^{\mu W}}{\rho_0} = \alpha P_{dark} \tag{5.40}$$

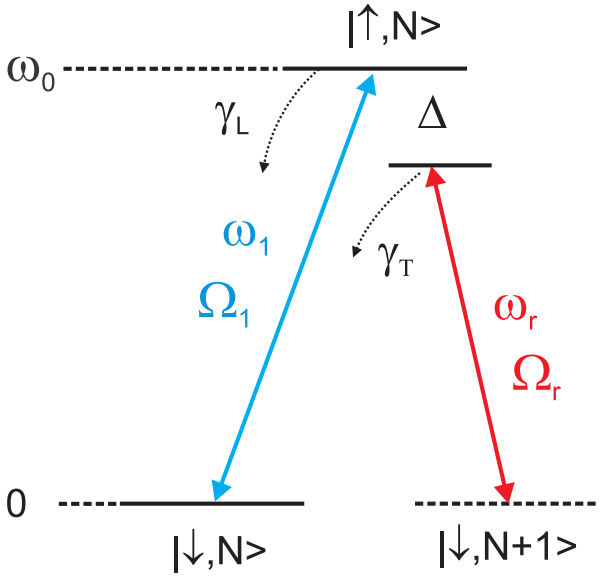

Figure 5-20: *Lambda system consisting of the SESR driven transition* (ω_1, Ω_1) *and the MESR transition* (ω_r, Ω_r) *across the Zeeman gap.*

where $\alpha \approx 10$ is the relative resistance change due to snake channeling calculated from the semiclassical drift-diffusion theory [38]. The ESAR peak is then modelled by Equation 5.40 based on the coherent population trapping theoretical framework. Figure 5-21 shows the ESAR peak at 110GHz fitted with Equation 5.40. Setting $\Omega_1/2\pi \approx 0.81$GHz, scaling the theoretical curve horizontally to fit the width of the ESAR peak returns $\gamma_L = \gamma_T = 1.76 \times 10^{10} s^{-1}$. The momentum scattering rate is $\mu m^*/e = 1.4 \times 10^{10} s^{-1}$, which is very close to the values of the relaxation rates, suggesting the spin relaxation time is limited by the lifetime of the snake orbits. The Rabi frequency of the microwave transition can be determined by scaling the theoretical curve vertically. It can be estimated as $\Omega_r/2\pi \approx 70$MHz. The system therefore operates in a regime where $\Omega_r \ll \Omega_1$ and by replacing $\Omega_r^2 + \Omega_1^2$ with Ω_1^2, the dependence of the ESAR peak amplitude with the microwave power becomes linear ($P_{\mu W} \propto \Omega_r^2$). This dependence can be observed in Figure 5-16. Other fitting parameters show that the lifetime of the dark state is comparable to the period of spin flips, $\Omega_1 = 0.29\gamma_L$, which is enough to observe coherent population trapping-related effects in the magnetoresistance. Increasing the lifetime of the dark state amplifies the ESAR peak as predicted by Equation 5.37.

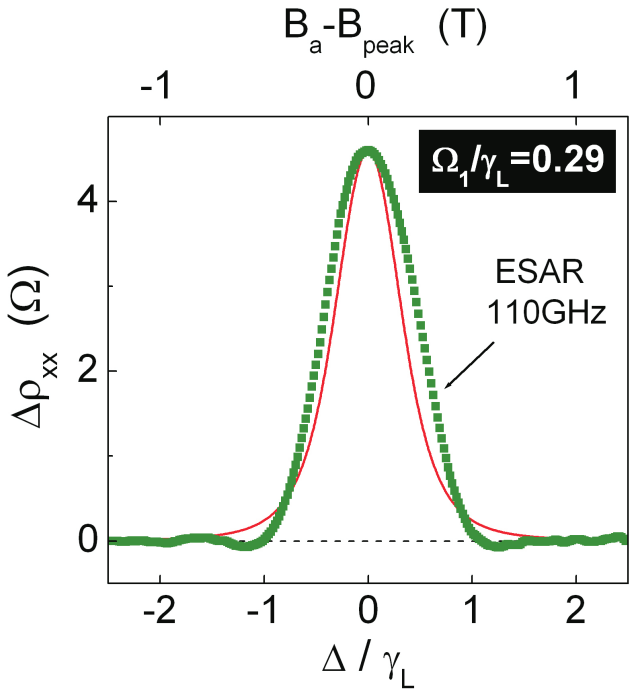

Figure 5-21: *Fit of the ESAR line at 110 GHz (squares) with Equation 5.40.*

It is demonstrated the coherent population trapping (CPT) of electron spins in snake orbits irradiated with microwaves. Two pathways to excite electron spin resonance with different Rabi frequencies interfere destructively. When both the MESR and the SESR transitions are resonant, their initial states hybridise and form a dark state. The dark state blocks spin flips and freezes snake channeling, affecting the 2DEG conduction. This is demonstrated as follows. Firstly, the longitudinal resistance develops an absorption peak when - and only when - both transitions are resonant. Secondly, the absorption peak exhibits an Overhauser shift that decreases with increasing microwave power - the opposite of conventional ESR. The mechanism underpinning this shift is a reduction in dynamic nuclear polarisation (DNP) caused by the blockade of spin flips. The change in the resistance induced by the dark state is computed and the result is used to fit the absorption peak. The spin relaxation rate and the Rabi frequencies are used as adjustment parameters and to find good agreement with expected values. Magnetic superlattices are thus shown to be an attractive system for performing coherent operations on the electron spin. The Overhauser shift observed is similar to the value predicted by Paget *et al* [9] for saturated GaAs nuclei, thus this

result is interpreted as evidence the nuclei are saturated. This is achieved by the hyperfine interaction between the electron spins in snake orbits, which are always in Rabi flopping with high Rabi frequency throughout the experience, and the nuclear spins in the GaAs nuclei.

Chapter 6

Conclusion

It was demonstrated a novel way of detecting ESR electrically in two dimensional electron gases using perpendicular, periodic, space varying magnetic fields with average zero amplitude.The method works reliably in a continuous range of frequencies, without the necessary conditions of previous efforts. An always occuring magnetic resonance of electrons describing snake-like open orbits in the 2DEG is blocked by a second magnetic resonance induced by the microwaves subject to detection. In terms of transport in the 2DEG, the magnetic resonance cancellation is reflected on the electron being scattered off the open orbit, therefore affecting the conduction in the 2DEG.

To somewhat simplify the mechanism, nuclear polarisation can be suppressed by saturating the NMR by irradiating the sample additionally with radio frequency electromagnetic waves, like the electron nuclear double resonance (ENDOR) case. The downside would be the shifting of the ESAR peaks approximately 5 T to higher applied magnetic field, which would require an experimental setup with a magnet of higher output for the used frequency range. InAs/InGaAs heterojunction based devices, for example, would have a much higher Landé g-factor which would bring the ESAR peaks to much lower fields. Unfortunately that field range is not "clean", *i.e.*, the ESAR peak could be drowned by other features like the V-shaped GMR due to snake orbits (Section 5.1) or DESW and DMW modes (Chapter 4).

This mechanism allows the development of submicron-scale electronic devices which can detect electromagnetic waves in the microwave range. It is the first of two steps towards the proof of concept of a nanotransceiver which can have a wide range of applications like wireless communications of very small electronic devices or as a replacement for physical interconnects in integrated electronic circuits.

This work paves the way for the fabrication of devices with optimised ESR peak amplitude by engineering the Rabi frequency of the two transitions in question. In the same class of devices, electrical induced microwave emission through the fluorescence of electron spins in snake orbits brought to resonance has been predicted but is yet to be measured experimentally [45, 46].

In Chapter 4, the high frequency dynamics of spins in magnetic 1D arrays were studied by using a 2DEG as a sensor. Two types of spin wave modes were observed: dipolar magnetisation waves which propagate across the 1D array through dipolar interaction between the stripes and dipolar edge spin waves, which are localised modes, confined in spin wave wells near the pole surfaces. It is shown that hybrid structures provide a highly sensitive and non-invasive probing of the magnetisation dynamics. This technique complements established techniques by providing access to extremely small magnets using submicron Hall junctions.

Appendix A

Demagnetisation factors of infinitely long stripes

Considering Figure 5-12 and setting $k = h/d$, the demagnetisation factors [33] of an infinitely long stripe with rectangular cross-section are $N_x = 0$ and

$$N_y = \frac{1}{\pi k} \ln\left(\frac{1}{\sqrt{1+k^2}}\right) + \frac{k}{\pi} \ln\left(\frac{\sqrt{1+k^2}}{k}\right) \tag{A.1}$$

$$N_z = \frac{k}{\pi} \ln\left(\frac{k}{\sqrt{1+k^2}}\right) + \frac{1}{\pi k} \ln\left(\sqrt{1+k^2}\right) + 1 - \frac{2}{\pi} \arctan k \tag{A.2}$$

Appendix B

Dipolar magnetic field generated by a 1D superlattice of rectangular prisms

The stray field generated by a periodic 1D array [38] can be calculated accurately at the plane $z = z_0$ by the formula

$$B_1(y, z_0) = \begin{cases} \mu_0 M \frac{hd}{a} \sum_{n=1}^{\infty} q_n F(q_n) e^{-q_n(z_0+h/2)} \sin(q_n x - \theta) \\ 0 \\ \mu_0 M \frac{hd}{a} \sum_{n=1}^{\infty} q_n F(q_n) e^{-q_n(z_0+h/2)} \cos(q_n x - \theta) \end{cases},$$

where $q_n = 2\pi n/a$, a is the period of the array, h is the height of the wires and d their width, θ is the angle the magnetisation vector does with the z axis and

$$F(q_n) = \frac{\sin(q_n d/2)}{q_n d/2} \frac{\sinh(q_n d/2}{q_n d/2} \tag{B.1}$$

is the geometric factor for wires with a rectangular cross-section.

Appendix C

Dipolar magnetic field generated by a 1D superlattice of rectangular prisms (improved)

The expression in Appendix B was modified in order to calculate the internal field inside the stripes.

The magnetic field emanating from the grating is obtained by solving the Maxwell's equations of magnetostatics $\nabla \cdot \vec{H} = -\nabla \cdot \vec{M}$ and $\nabla \times \vec{H} = 0$. Assuming that the stripes are magnetised homogeneously, the magnetisation within one period is:

$$\vec{M} = \begin{cases} 0 \\ M_y[\theta(z - h/2) - \theta(z + h/2)][\theta(y - d/2) - \theta(y + d/2)] \\ 0 \end{cases} \tag{C.1}$$

where θ is the Heaviside step function. The magnetisation function is stepwise and repeated across the grating, hence lending itself to Fourier analysis. The symmetry of the system and its invariance by translation along x imply that $\vec{H} = H_y(y, z)\hat{y} + H_z(y, z)\hat{z}$. The two Maxwell's equations are then solved in Fourier space by making the transformation:

$$\vec{H}(y,z) = \sum_{n=-\infty}^{+\infty} \vec{H}(q_n,z)e^{-iq_n y} \tag{C.2}$$

$$\vec{H}(q_n,z) = \frac{1}{a}\int_{-a/2}^{+a/2} dy \vec{H}(y,z)e^{+iq_n y} \tag{C.3}$$

where $q_n = 2\pi n/a$. The Fourier coefficients $\vec{H}(q_n,z)$ are first obtained and the stray magnetic field are computed in real space using Equation C.2. The in-plane stray magnetic field is:

$$H_y(y,z) = -M_y \frac{hd}{a}\sum_{n=1}^{+\infty} q_n F_y(q_y,z)\cos q_n y \tag{C.4}$$

with form factor F_y:

$$F_y(q_n,z) = \begin{cases} \frac{\sin q_n d/2}{q_n d/2}\frac{\sinh(q_n h/2)}{q_n h/2}e^{-q_n|z|} & |z| > h/2 \\ \frac{\sin(q_n d/2)}{q_n d/2}\frac{1-e^{-q_n h/2}\cosh(q_n z)}{q_n h/2} & |z| < h/2 \end{cases} \tag{C.5}$$

The perpendicular vector component is:

$$H_z(y,z) = -M_y \frac{hd}{a}\sum_{n=1}^{+\infty} q_n F_z(q_n,z)\sin q_n y \tag{C.6}$$

with form factor F_z:

$$F_z(q_n,z) = \begin{cases} \frac{\sin q_n d/2}{q_n d/2}\frac{\sinh(q_n h/2)}{q_n h/2}sgn(z)e^{-q_n|z|} & |z| > h/2 \\ \frac{\sin(q_n d/2)}{q_n d/2}\frac{\sinh(q_n z)}{q_n h/2}e^{-q_n h/2} & |z| < h/2 \end{cases} \tag{C.7}$$

where,

$$sgn(z) = \begin{cases} +1 & z > 0 \\ -1 & z < 0 \end{cases} \tag{C.8}$$

.

Appendix D

List of publications

The work described in this thesis has led to the following publications:

- Nogaret A, Nasirpouri F, Portal JC, Beere H, Ritchie D, Hindmarch AT, Marrows CH, *Double spin resonance in a spatially periodic magnetic field with zero average*, EPL 94, 28001, 2011
- Saraiva P, Nogaret A, Portal JC, Beere H, Ritchie D, *Dipolar spin waves of lateral magnetic superlattices*, Phys Rev B 82, 224417 2010
- Nogaret A, Saraiva P, Dai B, Portal JC, *Control of spin currents with double spin resonance*, Physica E 42, 926-928, 2010
- Saraiva P, Nogaret A, Krupko Y, Portal JC, Beere H, Ritchie D, *Photoresistance oscillations of magnetic quantum wires*, Physica E 40, 1436-1438, 2008

Bibliography

[1] C. Bayer, J. Jorzick, S. Demokritov, A. Slavin, K. Guslienko, D. Berkov, N. Gorn, M. Kostylev, and B. Hillebrands, "Spin-wave excitations in finite rectangular elements," in *Spin Dynamics in Confined Magnetic Structures III*, Vol. 103 (Springer, 2006) p. 57

[2] C. Bayer, S. O. Demokritov, B. Hillebrands, and A. N. Slavin, Appl. Phys. Lett. **82**, 607 (Jan. 2003)

[3] A. Nogaret, J. Phys.: Condensed Matter **22**, 253201 (Jun. 2010)

[4] A. Nogaret, Phys. Rev. Lett. **94**, 147207 (2005)

[5] M. Dobers, K. Klitzing, and G. Weimann, Phys. Rev. B **38**, 5453 (1988)

[6] M. Dobers, J. Vieren, Y. Guldner, P. Bove, F. Omnes, and M. Razeghi, Phys. Rev. B **40**, 8075 (Oct. 1989)

[7] P. Ye, D. Weiss, R. Gerhardts, and M. Seeger, Phys. Rev. Lett. **74**, 3013 (1995)

[8] A. Nogaret, S. Bending, and M. Henini, Phys. Rev. Lett. **84**, 2231 (2000)

[9] D. Paget, G. Lampel, and B. Sapoval, Phys. Rev. B **15**, 5780 (1977)

[10] M. Fleischhauer, A. Imamoglu, and J. Marangos, Rev. Mod. Phys. **77**, 633 (2005)

[11] C. Kittel, Phys. Rev. **73**, 155 (1948)

[12] C. W. J. Beenakker and H. van Houten, Arxiv **cond-mat/0412664** (2004)

[13] J. H. Davies, *The Physics of Low-dimensional Semiconductors: An Introduction* (Cambridge University Press, 1997)

[14] R. C. O'Handley, *Modern Magnetic Materials: Principles and Applications* (Wiley-Blackwell, 2000)

[15] D. D. Stancil and A. Prabhakar, *Spin Waves: Theory and Applications* (Springer, 2009)

[16] C. Kittel, *Introduction to Solid State Physics* (John Wiley & Sons, 2004)

[17] A. G. Gurevich and G. A. Melkov, *Magnetization: Oscillations and Waves* (CRC Press, 1996)

[18] M. I. Dyakonov, *Spin Physics in Semiconductors (Springer Series in Solid-State Sciences)* (Springer, 2008)

[19] A. Abragam and M. Goldman, Rep. Prog. Phys. **41**, 395 (1978)

[20] J. Jorzick, S. Demokritov, B. Hillebrands, M. Bailleul, C. Fermon, K. Guslienko, a. Slavin, D. Berkov, and N. Gorn, Phys. Rev. Lett. **88**, 047204 (Jan. 2002)

[21] J. Park, P. Eames, D. Engebretson, J. Berezovsky, and P. Crowell, Phys. Rev. Lett. **89**, 277201 (Dec. 2002)

[22] M. Kostylev, A. Serga, T. Schneider, T. Neumann, B. Leven, B. Hillebrands, and R. Stamps, Phys. Rev. B **76**, 184419 (Nov. 2007)

[23] J. Jorzick, S. Demokritov, C. Mathieu, B. Hillebrands, B. Bartenlian, C. Chappert, F. Rousseaux, and A. Slavin, Phys. Rev. B **60**, 15194 (Dec. 1999)

[24] R. I. Joseph and E. Schlomann, J. Appl. Phys. **36**, 1579 (1965)

[25] B. A. Kalinikos and A. N. Slavin, J. Phys. C: Solid State Physics **19**, 7013 (1986)

[26] G. Scott, Phys. Rev. **104**, 1497 (1956)

[27] F. C. Rossol, J. Appl. Phys. **37**, 1227 (Jun. 1966)

[28] T. Wagner and J. Stanford, Phys. Rev. B **5**, 1876 (Mar. 1972)

[29] R. Nicklow, N. Wakabayashi, and M. Wilkinson, Phys. Rev. Lett. **26**, 140 (1971)

[30] B. Cooper, R. Elliott, S. Nettel, and H. Suhl, Phys. Rev. **127**, 57 (1962)

[31] S. Legvold, J. Alstad, and J. Rhyne, Phys. Rev. Lett. **10**, 509 (1963)

[32] D. Lawton, A. Nogaret, S. Bending, D. Maude, J. Portal, and M. Henini, Phys. Rev. B **64**, 033312 (2001)

[33] D. J. Craik, *Magnetism: Principles and Applications* (Wiley, 1997)

[34] M. Kostylev, A. Stashkevich, and N. Sergeeva, Phys. Rev. B **69**, 064408 (2004)

[35] R. Oakeshott and A. MacKinnon, J. Phys.: Condensed Matter **5**, 9355 (1993)

[36] I. Ibrahim and F. Peeters, Phys. Rev. B **52**, 17321 (1995)

[37] J. Reijniers and F. Peeters, J. Phys.: Condensed Matter **12**, 9771 (2000)

[38] A. Nogaret, N. Overend, B. L. Gallagher, P. C. Main, and M. Henini, Physica E **2**, 421 (1998)

[39] J. Reijniers and F. Peeters, Phys. Rev. B **63**, 165317 (2001)

[40] A. Nogaret, P. Saraiva, B. Dai, and J. Portal, Physica E **42**, 926 (2010)

[41] R. Gerhardts, Phys. Rev. B **53**, 11064 (1996)

[42] S. Kronmüller, W. Dietsche, K. v. Klitzing, G. Denninger, W. Wegscheider, and M. Bichler, Phys. Rev. Lett. **82**, 4070 (1999)

[43] W. Desrat, D. Maude, M. Potemski, J. Portal, Z. Wasilewski, and G. Hill, Phys. Rev. Lett. **88**, 256807 (2002)

[44] A. Kiselev, E. Ivchenko, and U. Rössler, Phys. Rev. B **58**, 16353 (1998)

[45] A. Nogaret and F. M. Peeters, Phys. Rev. B **76**, 075311 (2007)

[46] A. Nogaret, N. J. Lambert, and F. M. Peeters, Phys. Rev. B **76**, 075312 (2007)